



UNIVERSITY OF LEEDS

# Band Structure of InAs/GaSb coupled quantum wells studied by magnetotransport



Craig Stewart Knox

University of Leeds

School of Electronic and Electrical Engineering

Submitted in accordance with the requirements for the degree of

*Doctor of Philosophy*

September, 2019

## Intellectual Property Statement

The candidate confirms that the work submitted is his/her/their own, except where work which has formed part of jointly authored publications has been included. The contribution of the candidate and the other authors to this work has been explicitly indicated below. The candidate confirms that appropriate credit has been given within the thesis where reference has been made to the work of others.

Work from the following jointly authored papers is in this thesis:

Spin-orbit interaction in InAs/GaSb heterostructures quantified by weak antilocalization by F. Herling, C. Morrison, **C. S. Knox**, S. Zhang, O. Newell, M. Myronov, E. H. Linfield, and C. H. Marrows in Physical Review B Vol. 95, 155307, 2017

This Paper details some of the fabrication methods used in the thesis, and is covered in chapter 3.

- **Work attributable to the candidate:** Device fabrication and sample preparation. Initial observation of effect.
- **Work attributable to collaborators:** F. Herling: Measurements, data analysis and writing of the manuscript. C. Morrison: Management of the project and data analysis. S. Zhang: Wafer growth and supply. O. Newell and M. Myronov, Measurement and support for millikelvin measurements. E. H. Linfield: Support and management for C. S. Knox, F. Herling and C. Morrison. C. H. Marrows: Support and management for C. S. Knox, F. Herling and C. Morrison.

Partial hybridisation of electron-hole states in an InAs/GaSb double quantum well heterostructure by **C. S. Knox**, C. Morrison, F. Herling, D. A. Ritchie, O. Newell, M. Myronov, E. H. Linfield, and C. H. Marrows in Semiconductor Science and Technology, Vol.32, 104002 (2017).

The work published covers the measurements on wafer C1295, covered in chapter 5.

- **Work attributable to the candidate:** Device fabrication, measurements, research of and writing of manuscript.
- **Work attributable to collaborators:** C. Morrison: Management of the project, millikelvin measurements and data analysis. D. A. Ritchie: Supply of material. O. Newell and M. Myronov, Measurement and support for millikelvin measurements. E. H. Linfield: Support and management for C. S. Knox and C. Morrison. C. H. Marrows: Support and management for C. S. Knox and C. Morrison.

Deconvolution of Rashba and Dresselhaus spin-orbit coupling by crystal axis dependent measurements of coupled InAs/GaSb quantum wells by C. S. Knox, L. H. Li, M. C. Rosamond, E. H. Linfield, and C. H. Marrows in Physical Review B Vol. 98, 155323, 2018.

The work published forms the vast majority of chapter 7.

- **Work attributable to the candidate:** Management of the project, device fabrication, measurements, data analysis, research of and writing of manuscript.
- **Work attributable to collaborators:** L.H. Li: Wafer growth and supply, M.C. Rosamond: Cleanroom support and advice for C. S. Knox. E. H. Linfield: Support and management for C. S. Knox and M. C. Rosamond. C. H. Marrows: Support and management for C. S. Knox.

This copy has been supplied on the understanding that it is copyright material and that no quotation from the thesis may be published without proper acknowledgement.

The right of Craig Stewart Knox to be identified as Author of this work has been asserted by him in accordance with the Copyright, Designs and Patents Act 1988.

© 2019 The University of Leeds and Craig Stewart Knox.

## Acknowledgements

I would like to start by thanking my supervisors, Professor Christopher Marrows and Professor Edmund Linfield. Their patience with my particular writing style clearly knows no limits, and they were always a goldmine of information about what I should be thinking about over the course of this PhD. Secondly, a huge thanks to Dr Christopher Morrison and Franz Herling, for coaching me through the tender early days of my PhD, and showing me that anything, done right, can make good science. The clean-room work would not be possible without Dr Mark Rosamond who not only somehow knows what I am doing without me saying a word, but also knows what I should be doing instead.

Also a special thanks to the rest of the Pollard Institute, particularly Dr Christopher Wood and Professor Giles Davies. Without their experience and intimate knowledge of 2DEG systems, this thesis would be a lot shorter. A huge thank you must also go to the Condensed Matter Group in the School of Physics and Astronomy, for graciously accommodating my never-ending thirst for cryostat time. Special thanks must also go to Dr Satoshi Sasaki for always being willing to discuss the minutiae of topological transport and Dr Gavin Burnell for his bottomless Python experience, and his One Code Labview software. Without this gigantic infrastructure in place as I started here, this project wouldn't have been nearly as successful as it has been. I am eternally grateful for the help of John Turton, Brian Gibbs, Luke Bone, David Chapman and Adam Foster for always being there when Blaataand needed filling, and having the patience to tolerate my persistent hovering.

Both the THz group in EEE and the Condensed Matter group in Physics truly have been a joy to work with, and have made the late nights and weekends bearable. Thanks to Dr David Bacon for the invaluable advice (on day one) to keep all my paper notes in one Word document. I only came to appreciate the value of CTRL+F within these last few months. Special thanks to Dr Georgios Stefanou, Benjamin Steele, Joshua Gretton, Matthew Vaughan, Amy Westerman, and Dr Fatima Al Ma'Mari for keeping me company in Lab 3 and sharing in my cryostat woes. I am grateful to all my office-mates over the years, Daniel Grout, Nicholas Peters, Katie Moran and Khulaif Alshammari. Only these guys would take in a refugee

from the open plan offices of EEE, and then put up with my complaints. I would also like thank my adoptive group-mates; Joseph Wilson, Dr Anne Ghesquiere and Dr Raoul Guiazon. Thank you for taking me into your Quantum-Information shaped hearts, and for making this thesis writing process bearable.

Finally, I would like to thank my friends and family for their constant support over the years. They have kept my spirits up throughout these 3.5 years. You've made this all worthwhile.

## Abstract

This thesis describes the characterisation of InAs/GaSb coupled quantum wells in the electron-dominated regime. The “inverted” band gap, created by electron-hole coupling within this material is predicted to give rise to a quantum spin Hall phase, where carrier dynamics are dominated by ballistic, spin-polarised, edge states. If it was possible to inject spin into these edge-states, this material could become the foundation for future spintronic devices. However, the effect of this electron-hole coupling on the electron-dominated transport is relatively unexplored. Therefore, this thesis studies the electron dominated regime in a variety of quantum wells, and highlights the differences between this coupled system and the single 2DEG transport, seen in previous studies of single InAs wells.

The effect the coupling has on the transport in the absence of a gate bias is probed by comparing the transport in a simple InAs/GaSb well to a similar well with an inter-layer AlSb barrier. Once it was determined that two carrier, electron-hole, transport exists in the InAs/AlSb/GaSb well, but not in the simple InAs/GaSb well, the effect of gate biases on the magnetotransport through the simple coupled well was also probed. In that case, the effects of higher order electron-hole coupling on the band-structure within this interesting coupled quantum well system was observed.

Finally, the spin-orbit coupling within this strongly coupled quantum well system is investigated. The Dresselhaus and Rashba spin-orbit coupling terms are explicitly calculated and their dependences on a small gate bias are noted. In particular, the Rashba spin orbit coupling is not only much larger than that observed in single InAs quantum wells, but it shows a remarkable dependence on the quantum well growth conditions. This strong spin-orbit coupling could have a profound impact on the quantum spin Hall effect predicted to arise in this material system, perturbing the polarisation axis of the quantum spin Hall state.

# CONTENTS

<b>1</b>	<b>Introduction</b>	<b>1</b>
<b>2</b>	<b>Theory and Background</b>	<b>5</b>
2.1	Band Structure of InAs/GaSb Coupled Wells . . . . .	6
2.1.1	Band Anticrossing . . . . .	8
2.1.2	Electron-Hole hybridisation in InAs/GaSb heterostructures . . .	10
2.1.3	Band Structure Tuning in InAs/GaSb quantum wells . . . . .	13
2.1.4	Modifying the hybridisation gap in InAs/GaSb coupled wells . .	16
2.2	Magnetotransport of a 2DEG . . . . .	19
2.2.1	Cyclotron motion and Landau levels . . . . .	19
2.2.2	The Shubnikov-de Haas effect . . . . .	20
2.2.3	The Integer Quantum Hall Effect . . . . .	23
2.2.4	Magnetotransport within InAs/GaSb coupled wells . . . . .	26
2.3	The Quantum Spin Hall Effect . . . . .	29
2.3.1	Theory of the QSHE . . . . .	29
2.3.2	Experimental Signatures of the QSHE . . . . .	32
<b>3</b>	<b>Wafer Growth and Device Fabrication</b>	<b>37</b>
3.1	Molecular Beam Epitaxy of InAs/GaSb wafers . . . . .	38
3.2	AFM Studies of as grown GaSb . . . . .	40
3.2.1	Principles of AFM . . . . .	40
3.2.2	AFM as a Measure of Growth Conditions . . . . .	42
3.3	Device Fabrication . . . . .	44
3.3.1	Photolithography techniques . . . . .	44
3.3.2	Ohmic Contact Metallisation by Thermal Evaporation . . . . .	47

3.3.3	Wet Chemical Etching . . . . .	51
3.3.4	Top Gate Fabrication . . . . .	53
3.3.5	Back Gating Processes . . . . .	55
<b>4</b>	<b>Cryogenic Measurements</b>	<b>58</b>
4.1	Continuous Flow <sup>4</sup> He Cryostat . . . . .	59
4.2	Magnetotransport Measurement Techniques . . . . .	62
4.3	<sup>3</sup> He Refrigerator . . . . .	64
<b>5</b>	<b>Effects of Limited Coupling on the Transport in InAs/(AlSb)/GaSb</b>	
	<b>Quantum Wells</b>	<b>68</b>
5.1	Sample Details . . . . .	69
5.2	Transport in the Case of Intimate Contact . . . . .	71
5.3	Transport in the Case of Disrupted Coupling . . . . .	77
5.4	Conclusions and Further Work . . . . .	87
<b>6</b>	<b>Scattering in Coupled Quantum Wells Far from Charge Neutrality</b>	<b>90</b>
6.1	Sample Details . . . . .	92
6.2	Mobility as a Function of Carrier Density . . . . .	94
6.3	Temperature Scaling of the Mobility . . . . .	99
6.4	Scattering in the Low Carrier Density Regime . . . . .	103
6.5	Scattering in the Peak Regime . . . . .	106
6.6	Scattering in the High Carrier Density Regime . . . . .	117
6.7	Wafer Dependence of Scattering . . . . .	118
6.8	Discussion . . . . .	121
6.9	Conclusions and Further Work . . . . .	130
<b>7</b>	<b>Spin-Orbit Coupling in InAs/GaSb Heterostructures Away from Charge</b>	
	<b>Neutrality</b>	<b>133</b>
7.1	Sample Details . . . . .	134
7.2	Observation of Spin-Orbit coupling in InAs/GaSb heterostructures . . . . .	136
7.3	Crystallographic Axis-Dependent Measurements of the Spin Orbit Coupling in G0156 . . . . .	139
7.4	Effects of Growth Conditions on Spin-Orbit Coupling within InAs/GaSb Heterostructures . . . . .	144

7.5	Conclusions and Further Work . . . . .	146
<b>8</b>	<b>Conclusions and Outlook</b>	<b>148</b>
8.1	Conclusions . . . . .	149
8.2	Outlook and Further Work . . . . .	151
<b>A</b>	<b>Device Fabrication Recipe</b>	<b>153</b>
	<b>References</b>	<b>157</b>

# LIST OF FIGURES

2.1	Band alignments at $k = 0$ within the 6.1 Å family of III-V semiconductors. The shaded regions represent the band gaps (in eV) within the bulk semiconductors, lattice matched to InAs. From [3]. . . . .	6
2.2	Example band alignments at $k = 0$ within three heterostructures. The left diagram shows a deep InAs quantum well, with the distribution of the 2DEG highlighted by the blue dashed line ( $ \Psi_e ^2$ ). The centre diagram shows a GaSb quantum well, with the distribution of the 2DHG highlighted by the red dashed line ( $ \Psi_h ^2$ ). Finally, the diagram on the right shows the band alignment within an InAs/GaSb coupled quantum well, highlighting the coexistence of a 2DEG (mostly localised within the InAs layer) and 2DHG (localised within the GaSb layer) . . . . .	7
2.3	Illustrative in-plane dispersion relations for the highest energy hole band (red) and the lowest energy electron band (black) in the coupled (solid) and uncoupled (dashed) case. Here, $\Delta$ is assumed to be a constant with respect to $k$ . . . . .	9
2.4	$k_{  }$ dependence of the dimensionless parameters $f_{1,2}$ (which describes the coupling strength between the electron and heavy hole subbands) along the $\langle 010 \rangle$ and $\langle 110 \rangle$ crystallographic axes. $f_1$ represents an event coupling electrons and heavy holes with a similar spin parities, whereas $f_2$ represents an event coupling electrons and heavy holes with opposite spin parities. From [4] . . . . .	11

2.5	Dispersion relation, along the $\langle 100 \rangle$ crystallographic axis, for an InAs/GaSb quantum well with well thicknesses of 30/15 nm, respectively. The first 3 electron and heavy hole subbands are shown, along with the first light hole subband. The labels indicate which bands are anticrossing. Adapted from [30] . . . . .	12
2.6	Fig. 2.6a shows an indicative phase diagram of an InAs/GaSb coupled quantum well under applied top ( $V_f$ ) and back ( $V_b$ ) gate biases. The top gate acts on the InAs layer, whereas the back gate acts on the GaSb layer. The system can either be inverted, with the associated electron-heavy hole anticrossing (shaded in red) or non-inverted (shaded in blue). The striped regions represent gapped regimes. Two top gate sweeps at a fixed back gate voltage are labelled A and B. Adapted from [5]. Fig. 2.6b shows schematically the electron-like (black) and hole-like (red) band structure in the non-inverted (top) and inverted (bottom) cases. Example Fermi energies for each region of Fig. 2.6a are highlighted by the blue dashed lines. . . . .	14
2.7	Fig. 2.7a shows the in-plane dispersion relations for an InAs/GaSb quantum well in the absence of an applied field (left) and with 3 T applied magnetic field (right). The black (red) points represent states that were originally electron (hole) states prior to coupling. An example energy which is mid-gap in the absence of a magnetic field, but contains states available for transport in the presence of a magnetic field is highlighted by blue dashed lines. Adapted from [41]. Fig. 2.7b shows a schematic diagram of similar dispersion relations when the well is in the non-inverted regime. The solid lines denote states in the absence of a magnetic field, whereas the dashed lines denote the same states under a small in-plane magnetic field. Note that in this case, no mid-gap states are created by application of an in-plane magnetic field. . . . .	17
2.8	In-plane dispersion relations for the principal electron (blue), heavy hole (red) and light hole bands (black) for different thicknesses of AlSb spacers ( $L_{\text{AlSb}}$ ). From [44]. . . . .	18

2.9	SdH oscillations (black) and quantum Hall data (red) measured on a GaAs/Al <sub>x</sub> Ga <sub>1-x</sub> As quantum well at 3 K. Note the position of the quantum Hall plateaux (which take values corresponding to integer fractions of the von Klitzing constant), and that the minima of the oscillations tend to 0 Ω resistance as we increase the magnetic field. . . . .	21
2.10	Schematic of cyclotron motion within a finite sample, when the Fermi energy is between the second and third Landau levels. Two edge states are observed running around the sample perimeter, whereas the bulk states are localised in closed cyclotron orbits and therefore cannot carry any current. Left-moving carriers are shown in blue, and right moving carriers are shown in red. . . . .	24
2.11	Schematic representations of the Laughlin pumping argument. Fig. 2.11a shows the model system considered, adapted from [58]. Fig. 2.11b shows the potential landscape of the system shown in Fig. 2.10, with the Landau levels shown in red, the Fermi energy shown in blue, the harmonic potential shown in green, and a cycle of the effective Laughlin pump shown in orange. . . . .	25
2.12	Fig. 2.12a shows schematically the band structure of an InAs/GaSb quantum well, highlighting the electron-like dispersion (red), the hole-like dispersion (blue), the hybridisation gap (yellow) and the QSHE edge states (pink and green). From [17]. Fig. 2.12b shows the edge states of a material in the QSHE state, with spin down shown in red and spin up shown in blue. From [72]. . . . .	31
2.13	Schematic dispersion of QSHE states in the perfectly out of plane polarised case (left) and in a generic helical edge mode case (right) [19]. In both cases, a forbidden elastic backscattering event is shown in black. . . . .	32
2.14	Longitudinal conductance as a function of applied top gate bias in a symmetric Hall bar, and an asymmetric “π” bar, showing the doubling of conductance (halving of resistance) with the removal of two contacts. The inset shows the conductance of the “π” bar structure as a function of $\frac{1}{T}$ , showing that the conductance is quantised below a sample temperature of 4 K. From [13]. . . . .	33

3.1	Schematic of an AFM in contact mode. The piezoelectric actuator responsible for moving the tip closer or further away from the surface is labelled Z, and the piezoelectric motors responsible for moving the tip horizontally in relation to the sample are labelled X,Y. Taken from [82].	41
3.2	AFM images of as grown layers of GaSb on n+ GaAs. Figs. 3.2a and 3.2b shows $10\ \mu\text{m} \times 10\ \mu\text{m}$ scans used to calculate the average roughness of the material. Fig. 3.2a shows a poorly optimised growth, with a rms roughness of $2.5 \pm 0.1\ \text{nm}$ , whereas Fig. 3.2b is well optimised, with a rms roughness of $0.9 \pm 0.1\ \text{nm}$ . Fig. 3.2c shows a $2\ \mu\text{m} \times 2\ \mu\text{m}$ scan, highlighting the fine structure of the mounds seen in Fig 3.2b. . . . .	43
3.3	Optical micrograph of a successful device on wafer G0186, showing the ohmic contacts (gold), the semiconductor channel (blue), the etched surface (brown) and the top gate electrode (light blue). The $\text{Al}_2\text{O}_3$ dielectric is transparent, and covers the whole device. . . . .	45
3.4	Schematic of photolithography process for a positive tone photoresist. .	45
3.5	Optical micrograph of a wafer SF0801 showing the damage (the brown, roughened surface) caused by 60 s of development in MF-322 (a more concentrated version of MF-319). . . . .	46
3.6	Optical micrograph of AuGeNi contacts on wafer SF0799 3.6a as deposited and 3.6b after 60 s thermal annealing. Note the blackened discoloration of the contact pads, which we attribute to the formation of Ge rich islands [87]. . . . .	48
3.7	Optical micrograph of etched quantum well surface on wafer SF0802 showing a nominally $10\ \mu\text{m}$ Hall bar arm; 3.7a shows where the ohmic contacts where annealed prior etching and 3.7b shows where no annealing has taken place. In both cases, the top of the mesa is shown in blue, the contact material is shown in yellow and the etched surface is shown in brown. Note the roughness of the mesa top in Fig. 3.7a, caused by the annealing process. . . . .	49
3.8	Hall resistance up to 8 T at 1.5 K in wafer G0049, where the device has been contacted by AuGeNi (black) and Cr/ Au (red). . . . .	50

3.9	SEM micrographs taken at 30 ° angle of incidence depicting etched sidewalls, etched by using the cocktail etch described here. Fig. 3.9a, taken by Dr Nicolas Peters, shows the residue left on the etched sidewalls, highlighted with an arrow. Fig. 3.9b, taken by Benjamin Steele, shows the etch undercut in an etched sidewall, highlighted with an arrow. . . .	52
3.10	Schematic diagram of one and a half ALD cycles, illustrating the formation of an oxide layer with a metallic precursor (in our case, tetramethylaluminium) and water. . . . .	54
3.11	Schematic diagram of the S1813-PMMA bilayer resist process used to define the top gate stack. . . . .	55
3.12	Hall resistance up to 8 T on two devices on wafer G0156. The red trace depicts a device with an annealed silver back gate and the black trace has not been annealed during packaging. The inset highlights the odd features in the high field quantum Hall regime, caused by the high resistance contact formed by the silver. . . . .	56
4.1	Schematic diagram of the continuous flow <sup>4</sup> He cryostat used in this thesis. From [98] . . . . .	60
4.2	Graph of the boiling point of various cryogenes as a function of pressure. From [99] . . . . .	61
4.3	Schematic diagram of a typical pulse-tube cryocooler. The entire structure is filled with coolant gas, in our case <sup>4</sup> He. From [99]. . . . .	65
5.1	Stack structures and band alignments for the two wafers studied in this chapter. The distributions of the electrons (blue dashed lines, $ \Psi_e ^2$ ) and heavy holes (red dashed lines, $ \Psi_h ^2$ ) at $k_{  } = 0$ are also highlighted. Fig. 5.1a shows the stack structure and band alignment for the strongly coupled wafer G0156. Fig. 5.1b shows shows the stack structure and band alignment for the weakly coupled wafer C1295. Note the significant portion of electron states within the GaSb layer in G0156 [23] that is diminished in C1295, as a result of introducing the inter-layer AlSb barrier.	70
5.2	Magnetoresistance up to 8 T as a function of temperature up to 10 K for a strongly hybridised wafer, G0156. Inset; the Zeeman split peak at 6.6 T and its temperature dependence. . . . .	71

5.3 Fig. 5.3a: Spin-degenerate SdH oscillations at 1.5 K in G0156 between 1.5 and 4 T, with the peaks highlighted in orange, the troughs highlighted in blue, and the average of these two shown in green. The quadratic fit, used to subtract a baseline is shown in red. Fig. 5.3b: The data in Fig. 5.3a with the extracted background subtracted. . . . . 73

5.4 Plots for self-consistent extraction of Dingle ratio  $\alpha$  and effective mass  $m^*$  in G0156. The linear fit used to extract these quantities is shown in red. These graphs had best fit for the effective mass of  $m^* = (0.040 \pm 0.005) m_0$ , where  $m_0$  is the free electron mass, and Dingle ratio ( $\alpha$ ) =  $28 \pm 3$ . . . . . 75

5.5 Hall resistance up to 8 T as a function of temperature up to 10 K for a strongly hybridised wafer (G0156). The expected positions of the QHE plateaux are shown in orange. The Zeeman split  $\nu = 5$  plateau is highlighted by an arrow. Inset; the highlighted Zeeman split plateau at 6.6 T and its temperature dependence. . . . . 77

5.6 Magnetoresistance up to 8 T as a function of temperature up to 10 K for a device on C1295, where the two quantum well layers were separated by a 2.5 nm thick AlSb barrier. . . . . 78

5.7 Plots for self-consistent extraction of Dingle ratio  $\alpha$  and effective mass  $m^*$  in C1295. The linear fit used to extract these quantities is shown in red. These graphs had best fit values for an effective mass of  $m^* = (0.070 \pm 0.005) m_0$ , where  $m_0$  is the free electron mass, and a Dingle ratio of  $\alpha = 15 \pm 1$  . . . . . 79

5.8 In plane dispersion relations for the principal electron (blue, labelled E), heavy hole (red, labelled HH) and light hole (black, labelled LH) bands for two different thicknesses of AlSb spacers ( $L_{\text{AlSb}}$ ). The left figure should be the dispersion of the strongly coupled wafer G0156. The Fermi energy, highlighted by the green dashed line, should result in transport that is analogous to a single 2DEG. The right figure should correspond to the dispersion of the weakly coupled wafer C1295. The Fermi energy (highlighted by the green dashed line) should give rise to SdH oscillations with an effective mass equal to the average between the electron and heavy-hole masses. Adapted from [44]. . . . . 80

5.9	Hall resistance up to 8 T for a weakly hybridised wafer, C1295, taken at 1.5 K. The expected positions of the IQHE plateaux, calculated from the ordinary Hall effect ( $B < 0.2$ T), are shown in orange. The insert highlights the non-linearity of the ordinary Hall effect at low magnetic fields ( $ B  \leq 1.5$ T). . . . .	82
5.10	Hall resistance up to 12 T for the weakly hybridised wafer, C1295, between 330 mK and 1.71 K. Inset; the anomalous $\nu \approx 3$ plateau at 9.3 T, and its temperature dependence. Data collected by Dr. Maksym Myronov, analysed by Dr Christopher Morrison. . . . .	83
5.11	Magnetoresistance up to 12 T for a weakly hybridised wafer between 330 mK and 1.71 K. The SdH minima responsible for the conventional $\nu = 4$ and $\nu = 3$ IQHE plateaux are highlighted by arrows. Data collected by Dr. Maksym Myronov, analysed by Dr Christopher Morrison. . . . .	84
5.12	Fig. 5.12a, Sheet resistance in C1295 at the 9.3 T minimum plotted as a function of temperature. Fig. 5.12b, the data in Fig. 5.12a plotted as $\frac{R_{\min}}{T}$ vs $T$ . The fit to equation 5.8 is shown in red. Data analysed by Dr Christopher Morrison. . . . .	86
5.13	Schematic diagrams for the electron (blue) and hole(red) Landau levels illustrating the Fermi energy ( $E_f$ ), the size of the hybridisation gap ( $\Delta$ ) and the level broadening ( $\Gamma$ ). Fig. 5.13a illustrates the case when the layers are in intimate contact, and so the hybridisation gap is much larger than the level broadening. Fig. 5.13b illustrates the effect of an AlSb spacer, reducing the hybridisation gap below the size of the Landau level broadening [18]. . . . .	87
6.1	Fig. 6.1a shows the stack structures studied within this chapter. Note that in both cases the InAs layer is closer to the top surface and so will be predominately affected by the application of a top gate bias. A schematic band alignment for this structure is shown in Fig. 6.1b, where the distributions of the electrons (blue dashed line, $ \Psi_e ^2$ ) and heavy holes (red dashed line, $ \Psi_h ^2$ ) at $k_{  } = 0$ are also highlighted, following [25]	92

6.2	Contour maps of the Hall carrier density (in Fig. 6.2a) and the Hall mobility (Fig. 6.2b) as a function of both top and back gate biases in G0186. The black lines indicate contours of constant Hall carrier density and mobility, respectively. . . . .	94
6.3	SdH oscillations as a function of Hall carrier density, modulated solely by a top gate bias, with the back gate grounded. Note the ring-like structures seen at high carrier densities ( $n \geq 20$ ) $\times 10^{11}$ $\text{cm}^{-2}$ ), indicative of SdH oscillations arising from a second carrier gas [120]. . . . .	96
6.4	Fig. 6.4a shows sheet resistance as a function of applied back gate bias at different applied top gate biases. Fig. 6.4b shows the IQHE behaviour at a constant top gate bias of $-3$ V at back gate biases of $-4.5$ V (black), $-5.5$ V (red), $-6$ V (blue), $-6.5$ V (pink), $-7$ V (green) and $-7.5$ V (dark blue). The inset shows the SdH oscillations at similar gate biases. In this case, the back gate was formed by annealing silver paint into the back surface of the device . . . . .	97
6.5	Hall mobility as a function of carrier density in G0186. This graph here represents the data in Fig 6.2b plotted as a function of the data in Fig. 6.2a. The different coloured symbols represent different back gate biases between $\pm 2.5$ V. . . . .	98
6.6	Hall mobility as a function of carrier density for different temperatures, up to 81 K. In this case, the carrier density was varied by applying a top gate bias between $\pm 2.5$ V, in the absence of a back gate bias. . . . .	100
6.7	Log-log plots of Hall mobility against sample temperature, at a constant carrier density. Fig. 6.7a represents a carrier density of $(10.0 \pm 0.1) \times 10^{11}$ $\text{cm}^{-2}$ (well before the peak in Hall mobility), Fig. 6.7b represents a carrier density of $(15.9 \pm 0.2) \times 10^{11}$ $\text{cm}^{-2}$ (at the peak in Hall mobility) and Fig. 6.7c represents a carrier density of $(22.4 \pm 0.2) \times 10^{11}$ $\text{cm}^{-2}$ (at a carrier density where the relative top and back gate biases is important to the Hall mobility). The solid red lines represent the fit over the low temperature ( $T < 20$ K) regime, whereas the dashed blue lines represent the fit over the high temperature ( $T > 50$ K) regime. For comparison, Fig. 6.7d shows the sheet resistance as a function of temperature on the same sample, with $T = 53$ K marked by the red, dashed line. . . . .	101

6.8	The low carrier density region of Fig. 6.5 plotted as a log-log plot of Hall mobility as a function of Hall carrier density. The fit to extract the power law scaling of the mobility is shown in red. As in Fig. 6.5, the back gate is biased between $\pm 2.5$ V for a range of top gate biases. . . .	104
6.9	Comparison between the low-field ( $B \leq 0.2$ T) Hall carrier density and the carrier density derived from the Fourier transform of the SdH oscillations as a function of back gate bias. The Hall carrier density is shown in black, whereas the SdH carrier density is shown in red. Fig. 6.9a shows the case where the carrier density was modulated solely by applying a back gate bias, with the top gate grounded, whereas Fig. 6.9b shows a similar study where the carrier density was tuned into the low carrier density regime by a $-1$ V top gate bias. . . . .	105
6.10	Transport scattering time and quantum lifetime as a function of Hall carrier density, in the low density regime. The effective mass and Dingle ratio needed to extract this data was derived from fitting the SdH amplitude as a function of temperature up to 20 K at each top gate bias, with the back gate grounded. . . . .	106
6.11	Fig. 6.11 shows the carrier density from the Fourier spectrum of the SdH oscillations shown in 6.3 (black and red). The carrier density extracted from the low field ( $B \leq 0.2$ T) Hall coefficient is also shown in green. The Hall mobility (shown in blue) is plotted for comparison. . . . .	107
6.12	SdH oscillations (black) and IQHE plateaux (red) in a device on G0186 at 1.5 K, showing transport consistent with that arising from a single 2DEG. The expected positions of the IQHE plateaux are shown in blue.	108
6.13	Top gate to channel capacitance plotted as a function of DC top gate bias at 1.5 K, with the back gate grounded. The subsequently measured Hall mobility is plotted in red, for comparison . . . . .	110

6.14 Fig. 6.14a shows the effective mass (in units of free electron mass) and the variation in Hall mobility across the peak and low carrier density regimes. Fig. 6.14b shows the ratio between the transport scattering time and the quantum lifetime (also known as the Dingle ratio) and the variation in Hall mobility across the peak and low carrier density regimes. Fig. 6.14c shows the transport scattering time and quantum lifetime as a function of Hall carrier density, in the peak regime. The effective mass and Dingle ratio needed to extract this data was derived from fitting the SdH amplitude as a function of temperature up to 20 K at each top gate bias. . . . . 111

6.15 Schematic diagrams of the 2D Fermi surface at a constant energy at 0 magnetic field (solid black lines) and including an in-plane magnetic field in the  $x$  direction (dashed red lines). Fig. 6.15a illustrates the case where a single subband is occupied, whereas Fig. 6.15b shows the case in which there are additional low- $k$  states at the Fermi energy. Following [129]. . . . . 113

6.16 Fig. 6.16a shows the in-plane magnetoresistance in a device of G0186 at 1.5 K, in the absence of a gate bias, for two different current orientations. The black curve shows the field orientated at right angles to the current direction, whereas the red curve shows the current orientated parallel to the magnetic field. This current-field alignment is shown schematically in Fig 6.16b, where the blue arrows represent the direction of the applied magnetic field, and the red arrows represent the direction along which the magnetoresistance was measured. . . . . 114

- 6.17 Fig. 6.17a shows the change in the in-plane magnetoresistance in a device of G0186 at 1.5 K for a range of top gate voltages (with a top gate step of 0.1 V), where the magnetic field was applied perpendicular to the current direction ( $B_x$ ,  $R_{yy}$ ). The curves are artificially offset for clarity. Fig. 6.17b is a contour plot of the normalised sheet resistance as a function of both top gate bias and applied in-plane magnetic field in the region where a  $B_{||} = 0$  maximum is present. The grey areas show where the resistance increases past the  $B_{||} = 0$  value, and therefore where the magnetoresistance returns to being parabolic, as in the single subband case. The black curve in Fig. 6.16a is a cross-section of Fig. 6.17b at the red dashed line. Fig. 6.17c shows the FWHM extracted from Fig. 6.17b as a function of top gate bias. The peak region is identified as being between  $\pm 0.6$  V top gate bias from subsequent measurements of the carrier density. . . . . 115
- 6.18 Hall mobility as a function of Hall carrier density in the high carrier density regime at 1.5 K. The different coloured points represent different back gate biases between  $\pm 2.5$  V. The transition from the unified trend in mobility with Hall carrier density to the regime where the relative top and back gate biases are important to transport is highlighted with a red arrow. . . . . 118
- 6.19 Hall mobility as a function of Hall carrier density in wafer G0156, grown on GaAs. The different colours represent different back gate biases between  $\pm 3$  V. . . . . 119

- 6.20 Log-log plots of the Hall mobility against sample temperature at a constant carrier density in wafer G0156, used to determine the dominant scattering mechanism. The solid red lines represent the fit over the low temperature ( $T < 20$  K) regime, whereas the dashed blue lines represent the fit over the high temperature ( $T > 50$  K) regime. Fig. 6.20a represents a carrier density of  $(11.1 \pm 0.1) \times 10^{11} \text{ cm}^{-2}$  (in the low carrier density regime); Fig. 6.20b represents a carrier density of  $(14.9 \pm 0.2) \times 10^{11} \text{ cm}^{-2}$  (at the peak in Hall mobility) and Fig. 6.20c represents a carrier density of  $(18.8 \pm 0.2) \times 10^{11} \text{ cm}^{-2}$  (in the high carrier density regime). For comparison, Fig. 6.20d shows the sheet resistance as a function of temperature on the same sample, with  $T = 47$  K marked by the red, dashed line. . . . . 120
- 6.21 Fig. 6.21a shows the effective mass and variation in Hall mobility in wafer G0156 as a function of top gate bias. Fig. 6.21b shows the Dingle ratio and variation in Hall mobility over the same gate bias range. Fig. 6.21c shows the transport scattering time and quantum lifetime, derived from Figs 6.21a and 6.21b. The effective mass and Dingle ratio needed to extract this data was derived from fitting the SdH amplitude as a function of temperature up to 20 K at each top gate bias. . . . . 122
- 6.22 Dispersion relations of the first excited electron (red) and heavy hole (black) bands in the absence of an applied negative back gate bias (solid lines) and in the presence of a negative voltage applied across the back gate, shifting the hole bands up by 30 meV (dashed lines). Band offsets were taken from [25]. The bottom of the uncoupled InAs band is set as zero energy. An example Fermi energy that would be in the low carrier density regime is shown by the black dotted line. . . . . 124

6.23 Dispersion relations of the first (red) and second (blue) excited electron subbands in the absence of an applied gate bias (solid lines, replicated from Fig. 6.22) and in the presence of a positive voltage applied across the top gate, shifting the electron bands down by 50 meV (dashed lines). An example Fermi energy is indicated by the dotted black line. This should be the state the of system at the onset of the peak regime. Band offsets were taken from [25]. The bottom of the uncoupled InAs band is set as zero energy. . . . . 127

6.24 Dispersion relations of the first (red) and second (blue) excited electron subbands. An example Fermi energy is indicated by the dotted black line. Fig. 6.24a shows the relevant subbands in the absence of an applied gate bias (solid lines, replicated from fig Fig. 6.22) and in the presence of a positive voltage applied across the top gate, shifting the electron bands down by 100 meV (dashed lines). Both traces in Fig. 6.24b show the relevant bands under a positive top gate bias shifting the electron bands down by 100 meV. As such, the dashed trace in this figure corresponds to the dashed trace in Fig. 6.24a. However, the thick dash-dot-dash trace shows the effects of applying an additional negative back gate bias, shifting the hole bands up 2 meV, as would occur within the high carrier density regime. Band offsets were taken from [25]. The bottom of the uncoupled InAs band is set as zero energy. . . . . 128

7.1 Fig. 7.1a shows the stack structures studied within this chapter. A schematic band alignment for this structure is shown in Fig. 7.1b, where the distributions of the electrons (blue dashed line,  $|\Psi_e|^2$ ) and heavy holes (red dashed line,  $|\Psi_h|^2$ ) at  $k_{||} = 0$  are also highlighted, following [25] 135

7.2 Hall resistance up to 8 T for wafers studied in this chapter. Fig. 7.2a shows the Hall resistance in G0153, whereas Fig. 7.2b shows the Hall resistance in G0156. In both cases, the measured data is displayed in black, with the expected 0 K plateaux positions from the low field (applied field  $< 0.2$  T) Hall measurements displayed in red. The  $\nu = 10, 11$  and 12 plateaux are highlighted by arrows in both Fig 7.2a and 7.2b, along with an interesting odd-integer plateau at low magnetic field ( $\nu = 27$ ) in Fig. 7.2a, indicating the presence of a second carrier gas. . . . . 137

7.3	Magnetoresistance up to 2.5 T (in the absence of a gate bias) as a function of temperature up to 10 K, used to extract the effective mass for wafers studied in this chapter. Fig. 7.3a shows the magnetoresistance in wafer G0153, whereas Fig. 7.3b shows the magnetoresistance in wafer G0156. . . . .	138
7.4	Fig. 7.4a SdH oscillations plotted as a function of inverse field used in the Fourier analysis at $-1$ V applied top gate bias in G0156. A beating mode, indicating the two separate frequencies is highlighted in the inset. Fig. 7.4b is a discrete Fourier transform of Fig. 7.4a. The two frequencies, corresponding to the two spin-split carrier densities are highlighted with arrows. . . . .	139
7.5	Total SOC parameters $\Omega$ along the $[100]$ , $[110]$ and $[1\bar{1}0]$ axes as a function of applied top gate bias in wafer G0156. . . . .	140
7.6	Schematic diagrams of the 2D Fermi-surface, showing the relative orientations of the effective SOC magnetic field in a quantum well grown along the $[001]$ axis. Fig 7.6a shows the orientation of the effective magnetic field arising from Rashba SOC, while Fig 7.6b shows same information for the Dresselhaus SOC. Fig 7.6c shows the total magnetic field due to SOC experienced in this class of quantum well, where the length of arrow is proportional to the strength of the spin-splitting experienced by the carriers. Here, we assume that the Rashba term makes a dominant contribution to the SOC. . . . .	142
7.7	Fig. 7.7a shows the total SOC parameter at zero top gate voltage in G0156, plotted as a function of angle to the $[110]$ axis, showing the expected $\cos(2\theta)$ dependence. The fit to equation 7.2 is shown in red. Fig. 7.7b shows the Rashba and Dresselhaus parameters found from fitting equation 7.2 to the relevant data in Fig.7.5. . . . .	143
7.8	Collection of total SOC parameters $\Omega$ along the $[100]$ , $[110]$ and $[1\bar{1}0]$ axes as a function of applied top gate bias in wafer G0153. . . . .	144
7.9	Fig. 7.9a, total SOC parameter at zero gate bias in G0153, plotted as a function of angle to the $[110]$ axis. The fit to equation 7.2 is shown in red. Fig. 7.9b, Rashba and Dresselhaus parameters found from fitting equation 7.2 to the relevant data in Fig.7.8. . . . .	145

## Abbreviations

2DEG	Two Dimensional Electron Gas	AC	Alternating Current
DC	Direct Current	FET	Field Effect Transistor
FWHM	Full Width Half Maximum	IPA	Isopropyl Alcohol
IQHE	Integer Quantum Hall Effect	PMMA	Poly(Methyl Meth-Acrylate)
SdH	Shubnikov de-Haas	UVO	Ultra Violet Ozone

---

# CHAPTER 1

---

Introduction

---

For the past 60 years, advances in semiconductor physics and semiconductor fabrication have delivered revolutionary new devices. Key to this success is the additional degree of freedom that semiconductors provide over their metallic and insulating counterparts, namely a small band-gap, that can be tuned by doping or applying an electric field in the form of a gate bias. This has led to the development of bipolar and metal-oxide-semiconductor transistors, used throughout modern electronics. Furthermore, as methods for fabricating semiconductor heterostructures have improved, so has the range of semiconductor structures available for study. A key motivating factor has been to modulate the band gap seen in semiconductors, either by strain [1], doping [2], or the choice in material [3], to suit the desired application.

Normally, the electron states within the conduction band of a semiconductor have a parabolic dispersion relation, characterised by a single effective mass  $m^*$ . However, what if this were not the case? Such a scenario can be engineered in InAs/GaSb heterostructures, where due to the energies within the system, the hole bands in the GaSb are more energetic than the lowest energy electron bands within the InAs. This leads to the electrons within this system having a hole-like dispersion at low momentum, completely opposite to the usual case. The semiconducting gap in this composite system is then controlled, not by the bulk parameters of the semiconductor, but by the strength of the coupling between the n-type InAs layer and the p-type GaSb layer [4].

This “inverted” band alignment is so radically different to the environment external to the device (e.g. in either the metallic contacts or the vacuum) that there must exist a transition region between this “inverted” regime and the non-inverted regime that closes the gap [5]. As this transition closes the “inverted” band gap, and fundamentally changes the topology of the system, the system is said to be a two-dimensional topological insulator (2DTI). This topological transition region is then predicted to be characterised by a set of counter-propagating, spin polarised edge states, leading to the quantum spin Hall effect (QSHE). Within these QSHE edge states, spin-states travel ballistically, without scattering [6], enabling coherent transport of spin over large ( $\mu\text{m}$  length) distances. Additionally, within these edge states, the polarisation of the spin-states is locked to their direction of travel. As such, 2DTIs open up opportunities for new device physics, from spin-based transistors [7] to new quantum computing architectures [8].

Recent research into this interesting, InAs/GaSb system has therefore focussed on

---

accessing this gapped state [9], probing the magnitude of the gap [10–12] and exploring the new topological physics present within this gapped regime [13–17]. However, the conventional transport outside the “inverted” gap region remains relatively unexplored. This is due to the assumption that the transport far from the gapped regime is analogous to a single InAs (in the electron dominated regime) or GaSb (in the hole dominated regime) quantum well [12]. This thesis will examine the electronic transport through this electron-dominated regime in detail and show clear distinctions between transport within these coupled quantum wells and that shown in single InAs quantum wells studied in the literature.

In chapter 2, a review of the concepts used throughout the thesis is presented, alongside a literature review, putting the individual experimental chapters into the wider experimental context of this material system. All the devices measured within this thesis were grown using molecular beam epitaxy, and then patterned into measurable devices in a cleanroom environment using optical lithography and wet etching techniques. These techniques are outlined in chapter 3. The experimental techniques used to observe transport throughout this material are then discussed in chapter 4.

Chapter 5 considers the effects of limiting the coupling between the InAs and GaSb layers by inserting an AlSb spacer between the two quantum well layers. While studies of this nature have been undertaken previously [18], the effects of limited coupling on the effective mass of the carriers present is also explored here. This provides insight into the nature of the transport within these coupled quantum wells when the inter-well coupling is inhibited. It is found that, by inhibiting the inter-well coupling, and closing the “inverted” band gap a second transport channel can be observed, arising from the hole states in the GaSb.

Chapter 6 looks at the relationship between mobility and carrier density within these structures in detail, in an effort to understand how the inter-well coupling affects transport. Of particular interest is how a gate bias applied to the GaSb layer affects transport through the heterostructure, especially when the majority carriers are electrons, localised within the InAs layer. We find that, at high electron-like carrier densities, a gate bias applied to the GaSb layer does not affect the Hall mobility in the same way as a gate bias applied to the InAs layer. From this, we infer that the inter-well coupling is important to the electron transport at all carrier densities, not just when the Fermi energy is near to the “inverted” band gap.

---

Finally, the spin-orbit coupling (SOC) within this class of heterostructure is considered in chapter 7. The spin dynamics of the normal state could have profound consequences on the topological regime [19, 20], and so is of inherent experimental interest. From our measurements, we find that the magnitude of the SOC within these coupled quantum wells is greatly enhanced when compared to single InAs quantum wells. We also find that the Dresselhaus SOC, arising from the asymmetries present within the zinc-blende crystallographic structure is remarkably robust against applied gate voltages and small changes in the growth conditions.

---

# CHAPTER 2

---

Theory and Background

This chapter introduces the band structure of InAs/GaSb coupled quantum wells, and the origin of electron-hole hybridisation in these structures. The physical principles that underpin the investigation of this band structure, through high field magnetotransport, will also be discussed. Finally, the chapter will conclude with a brief introduction into one motive for considering this unusual heterostructure, the study of the quantum spin Hall effect.

## 2.1 Band Structure of InAs/GaSb Coupled Wells

The compound semiconductors InAs, GaSb and AlSb are all III-V semiconductors, with lattice constants of approximately  $6.1 \text{ \AA}$  in a zinc-blende crystal structure [3]. Due to their similar lattice constants, heterostructures can be easily grown (by conventional MBE techniques) with a minimum of strain induced defects [21, 22]. Of particular interest is the band alignment within these materials, which is shown in Fig. 2.1.

We initially note that a thin InAs layer, sandwiched between two AlSb barriers,

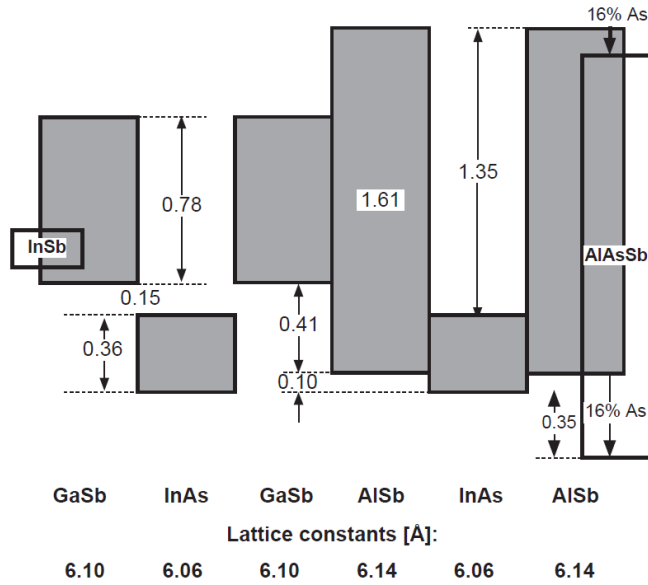


Figure 2.1: Band alignments at  $k = 0$  within the  $6.1 \text{ \AA}$  family of III-V semiconductors. The shaded regions represent the band gaps (in eV) within the bulk semiconductors, lattice matched to InAs. From [3].

## 2.1 Band Structure of InAs/GaSb Coupled Wells

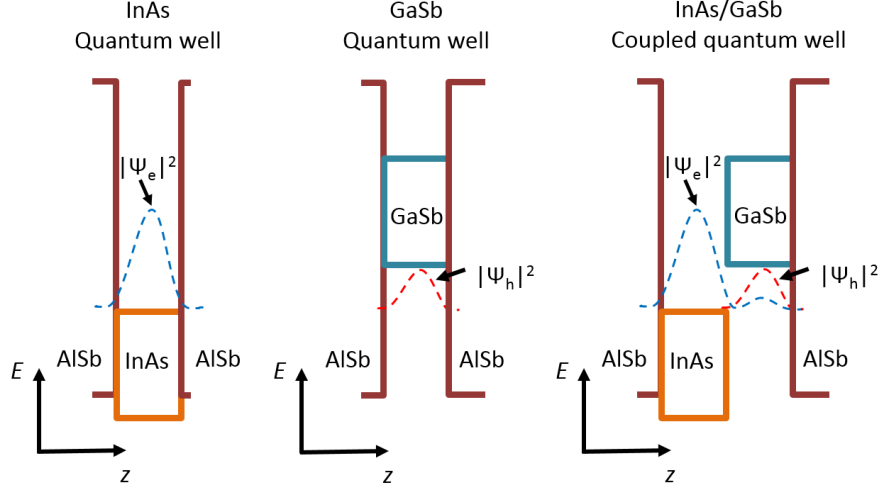


Figure 2.2: Example band alignments at  $k = 0$  within three heterostructures. The left diagram shows a deep InAs quantum well, with the distribution of the 2DEG highlighted by the blue dashed line ( $|\Psi_e|^2$ ). The centre diagram shows a GaSb quantum well, with the distribution of the 2DHG highlighted by the red dashed line ( $|\Psi_h|^2$ ). Finally, the diagram on the right shows the band alignment within an InAs/GaSb coupled quantum well, highlighting the coexistence of a 2DEG (mostly localised within the InAs layer) and 2DHG (localised within the GaSb layer)

would form a deep quantum well. An electron within the InAs conduction band would be forbidden from entering the AlSb layers, as no electronic states would be available for transport. As such, the electrons within the InAs layer would act as a 2-dimensional electron gas (2DEG) where the transport is confined to the plane of the InAs layer. Additionally, the hole states within GaSb can be similarly confined by AlSb barriers, creating a 2-dimensional hole gas (2DHG).

A more interesting consequence of this band alignment is the “staggered” band alignment between InAs and GaSb, where the bottom of the conduction band in InAs is lower in energy than the top of the valence band in GaSb. If these two layers were in contact, there would be charge transfer from the GaSb layer into the InAs layer. This charge transfer will couple the two quantum wells [23, 24]. This coupling allows the hybridisation of the electron and hole states, drastically altering the dispersion of the conduction and valence bands within the composite system. The band alignments

---

## 2.1 Band Structure of InAs/GaSb Coupled Wells

for single InAs/AlSb and GaSb/AlSb quantum wells are shown in Fig. 2.2, alongside the band alignment for an InAs/GaSb coupled quantum well. Note the significant extension of electron-like states within the GaSb well in the coupled case, responsible for the inter-well coupling [23, 25]. This inter-well coupling, and the resulting band structures, will be discussed throughout the remainder of this section.

### 2.1.1 Band Anticrossing

In a general case, coupling between two states will lead to a modification of the energies of the initial states. This becomes especially important if the two coupled states originally occurred at the same energy. In that case, the coupling will create an energy gap between the two states, in a phenomenon known as “avoided crossing”, or anticrossing. Electron-hole hybridisation in InAs/GaSb coupled systems is a textbook example of this anticrossing, where the coupling between the two quantum well systems will create a gap in the hybrid dispersion relation that did not exist in the uncoupled case. For simplicity, we will consider only the states within the highest energy hole band from the GaSb ( $\psi_h$ ) and the states within lowest energy electron band in the InAs ( $\psi_e$ ). If we neglect the coupling between the states, the system can be described by:

$$\begin{bmatrix} H_e & 0 \\ 0 & H_h \end{bmatrix} \begin{pmatrix} \psi_e \\ \psi_h \end{pmatrix} = E \begin{pmatrix} \psi_e \\ \psi_h \end{pmatrix} \quad (2.1)$$

where  $H$  is the Hamiltonian of the uncoupled quantum well, and the subscript e or h denotes either electrons or holes, respectively. Naturally, the eigenvalues of this system are the uncoupled dispersion relations of the InAs and GaSb 2D carrier gases. However, once we introduce coupling between the wells, the system becomes [4]:

$$\begin{bmatrix} H_e & \Delta \\ \Delta & H_h \end{bmatrix} \begin{pmatrix} \psi_e \\ \psi_h \end{pmatrix} = E \begin{pmatrix} \psi_e \\ \psi_h \end{pmatrix} \quad (2.2)$$

where  $\Delta$  is a parameter associated with the strength of the coupling between the two quantum wells. We notice that the eigenvalues of this new coupled system are:

$$E = \frac{1}{2}[(H_e + H_h) \pm \sqrt{(H_e - H_h)^2 + 4\Delta^2}] \quad (2.3)$$

where the new electron dispersion relation corresponds to the + arm of equation 2.3, and the hole dispersion relation corresponds to the – arm of the same. If we assume that the effective masses ( $m^*$ ) of the electron and hole states are constant with respect to  $k$ , and

## 2.1 Band Structure of InAs/GaSb Coupled Wells

that the bottom of the InAs conduction band is at 0 energy, the uncoupled Hamiltonians are;  $H_e = \frac{\hbar^2 k^2}{2m_e^*}$  and  $H_h = E_o - \frac{\hbar^2 k^2}{2m_h^*}$ , where  $E_o$  is the offset between the maximum of the uncoupled hole dispersion relation and the minimum of the uncoupled electron dispersion relation, and  $k$  is the in-plane wavevector. An illustration of this coupled system, using these unperturbed Hamiltonians and assuming that  $\Delta$  is a constant with respect to momentum is shown in Fig. 2.3.

We notice that a gap due to the anticrossing ( $E_g$ ) opens at a finite in-plane momentum,  $k_{\text{cross}}$ . It is worth highlighting that, in this simplified case, the size of the gap is independent of the  $k_{\parallel} = 0$  overlap ( $E_o$ ) and instead only depends the magnitude of the quantum well coupling,  $\Delta$ . Additionally, we see that as the wave vector  $k$  approaches 0, the electron (hole) band acquires the shape of the uncoupled hole (electron) band. This will result in electron-like states in the coupled system travelling through the sample with a hole-like dispersion relation at low  $k$  [24].

However, the model presented in Fig. 2.3 is an oversimplification. One detail overlooked is the lack of spin-degeneracy in InAs/GaSb heterostructures. If we consider an InAs layer within an InAs/GaSb coupled quantum well, we observe that on one side, the InAs will be adjacent to an AlSb barrier, whereas on the other side, it will be next to

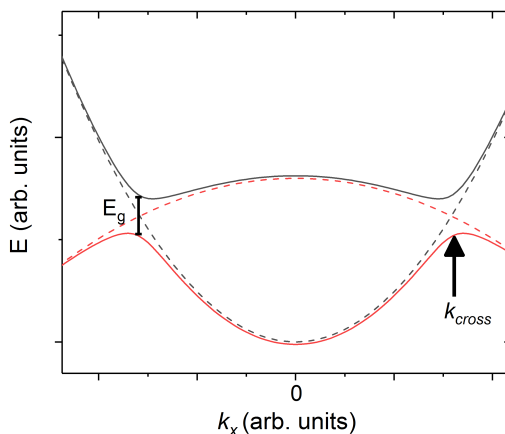


Figure 2.3: Illustrative in-plane dispersion relations for the highest energy hole band (red) and the lowest energy electron band (black) in the coupled (solid) and uncoupled (dashed) case. Here,  $\Delta$  is assumed to be a constant with respect to  $k$

the GaSb layer within the quantum well. This inherent structural inversion asymmetry will create a potential difference across the quantum well [26], which will give rise to an electric field. Relativistic carriers within the quantum well will experience that electric field as an effective magnetic field, causing states with spins aligned to that effective field to have a lower energy than states with similar wavevectors, but opposite spins. Additionally, the zinc blende crystal structures found throughout these III-V semiconductors lack bulk inversion symmetry, resulting in an additional potential gradient, and so a further effective magnetic field [27].

The Rashba spin-orbit coupling (SOC) arising from the structural inversion asymmetry, and the Dresselhaus SOC arising from the bulk inversion asymmetry have to be taken into account when calculating the dispersion relation of these coupled quantum wells. In fact the energy splitting arising from this SOC can be of the same magnitude as the anticrossing gap,  $E_g$  [25, 28]. The magnitudes of these SOC terms will be further discussed in chapter 7.

### 2.1.2 Electron-Hole hybridisation in InAs/GaSb heterostructures

Perhaps more importantly, Fig. 2.3 assumes that the quantum well coupling ( $\Delta$ ) is constant with respect to in-plane wavevector. However, due to the symmetries of the lowest energy electron band in InAs and the highest energy hole band in GaSb, this cannot be the case. A formal consideration of this problem requires a complex 8-band  $\mathbf{k}\cdot\mathbf{p}$  calculation, where spin degeneracies [25] and band non-parabolicities [4] can be explicitly included. The details of such a model are beyond the scope of this thesis, but the numerical results of such models are worthy topics of discussion.

The states in the conduction band in InAs are s-like, with a total angular momentum quantum number of  $m_i = \pm\frac{1}{2}$ . On the other hand, the states in the highest energy hole band in GaSb are heavy-holes, with a total angular momentum quantum number of  $m_i = \pm\frac{3}{2}$ . As any inter-well tunnelling event would have to conserve angular momentum, the electron states in InAs cannot directly couple to the heavy hole states within the GaSb [4, 24, 25].

As such, an intermediary state is required, in the form of light-holes (so called because their lower angular momentum leads to a lower effective mass than the heavy-hole states [21]) within the GaSb, with a total angular momentum quantum number of  $m_i = \pm\frac{1}{2}$ . In fact, the electron distribution extends significantly from the InAs layer

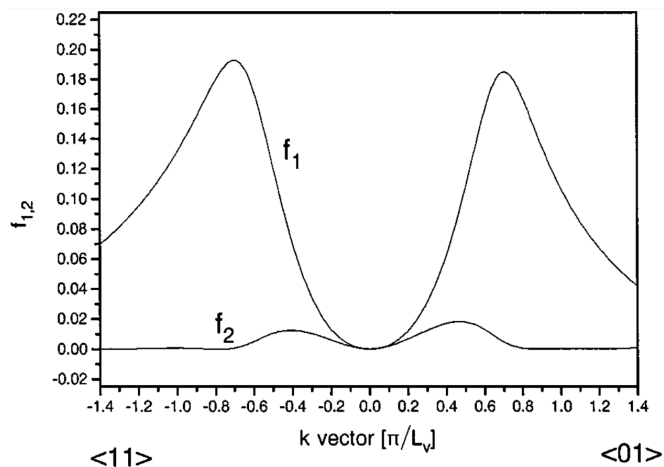


Figure 2.4:  $k_{\parallel}$  dependence of the dimensionless parameters  $f_{1,2}$  (which describes the coupling strength between the electron and heavy hole subbands) along the  $\langle 010 \rangle$  and  $\langle 110 \rangle$  crystallographic axes.  $f_1$  represents an event coupling electrons and heavy holes with a similar spin parities, whereas  $f_2$  represents an event coupling electrons and heavy holes with opposite spin parities. From [4]

into an adjacent GaSb layer, just as the light hole distribution extends from the GaSb into the InAs [25, 28]. It is worth noting that at  $k_{\parallel} = 0$  there is no extension of the heavy hole states into the InAs layer [25]. At a finite in-plane momentum  $k_{\parallel} \neq 0$ , the total angular momentum of the heavy hole states is no longer a good quantum number. This allows light hole states to mix with the heavy hole states away from the band centre, indirectly coupling the electron and heavy hole dispersion relations through the mixed-in light holes [4, 29]. The  $k_{\parallel}$  dependence of this indirect coupling is shown in Fig. 2.4, where  $f_1$  represents an event coupling electrons and heavy holes with a similar spin parities, (e.g.  $+\frac{1}{2} \Rightarrow +\frac{3}{2}$ ), whereas  $f_2$  represents an event coupling electrons and heavy holes with opposite spin parities (e.g.  $+\frac{1}{2} \Rightarrow -\frac{3}{2}$ ) [4].

Fig. 2.4 shows an important property of the electron-heavy hole coupling, namely that the coupling is slightly stronger along the  $\langle 110 \rangle$  crystallographic axis when compared to the  $\langle 010 \rangle$  crystallographic axis (both of which are in the plane of the quantum well) due to the nonparabolicity of the light hole band. This can lead to situations where the Fermi energy is within the gapped regime in one axis, but not in the other [4]. However, measurements of the resistance of an InAs/GaSb quantum

## 2.1 Band Structure of InAs/GaSb Coupled Wells

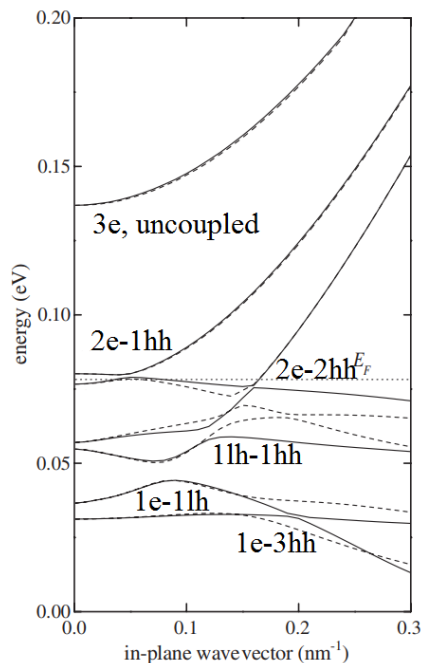


Figure 2.5: Dispersion relation, along the  $\langle 100 \rangle$  crystallographic axis, for an InAs/GaSb quantum well with well thicknesses of 30/15 nm, respectively. The first 3 electron and heavy hole subbands are shown, along with the first light hole subband. The labels indicate which bands are anticrossing. Adapted from [30]

well within the gapped regime shows that this anisotropy is not sufficient to close the hybridisation gap [12].

We note that we have only discussed the coupling between the first electron and heavy hole subbands. As we vary the thickness of the wells, higher order subbands will have energies that can enter the hybridisation gap. For example, higher order heavy hole subbands will mix with the light hole bands, and therefore anticross with uncoupled electron bands [25]. The same is true for higher order electron subbands which will hybridise with the mixed-in light holes, and so anticross with uncoupled heavy hole subbands [30, 31]. An example band structure, calculated along the  $\langle 100 \rangle$  crystallographic axis, containing multiple anticrossing gaps is shown in Fig. 2.5.

### 2.1.3 Band Structure Tuning in InAs/GaSb quantum wells

Experimentally, InAs/GaSb quantum wells show transport that is dominated by the electron-like (i.e.  $m_i = \pm\frac{1}{2}$ , charge  $-e$ ) states in the absence of an external electric field [12, 32, 33], as the Fermi energy is pinned within the InAs bands. Therefore, in order to explore the gapped regime, we require a means to tune the band-structure so that the Fermi energy enters the electron-heavy hole hybridisation gap. This is most commonly achieved by gating the coupled quantum well system. For a single quantum well, applying a gate bias to the top or bottom of the structure will create an electric field across the heterostructure. This electric field will shift the energy of the bands within the quantum well, altering the number of available states below the Fermi energy, allowing carriers to be depleted or excited.

A further degree of control can be obtained in coupled quantum wells by applying a top and back gate bias simultaneously. If we apply, for example, a top gate bias, as long as a relatively small (e.g.  $n > 7 \times 10^{10} \text{ cm}^{-2}$ ) number of carriers exist in the quantum well layer closest to the top gate electrode (either InAs or GaSb), the layer underneath will be completely screened from the electric field produced by the applied gate bias [34]. This allows one to shift the electron dispersion relation relative to the hole dispersion relation, and vice versa. As such, it should be possible to tune the system from a completely unhybridised state (where the electron dispersion does not cross any hole bands) to a hybridised state with electron-hole anticrossing. A schematic diagram of this phase transition is shown in Fig. 2.6 [5].

As the gapped region (regions II and V in Fig. 2.6) occurs when the Fermi energy lies within a gap between a regime where the majority carriers are electrons, and a regime where the majority carriers are holes, it is often referred to as a charge neutrality point [32, 35, 36]. Near to this charge neutral regime, where the electron and hole concentrations are of similar magnitude, the action of a gate bias on the InAs or GaSb layers is experimentally obvious. The Hall resistance does not scale linearly with an applied magnetic field under these conditions, a characteristic of two-carrier transport [37].

However, when transport is dominated by one carrier type (regions I and IV for holes and regions III and VI for electrons in Fig. 2.6) the effects of a gate bias on the minority carriers are less obvious. It has been observed that by applying an external electric field to the GaSb layer, while the system is in the electron dominated regime, the

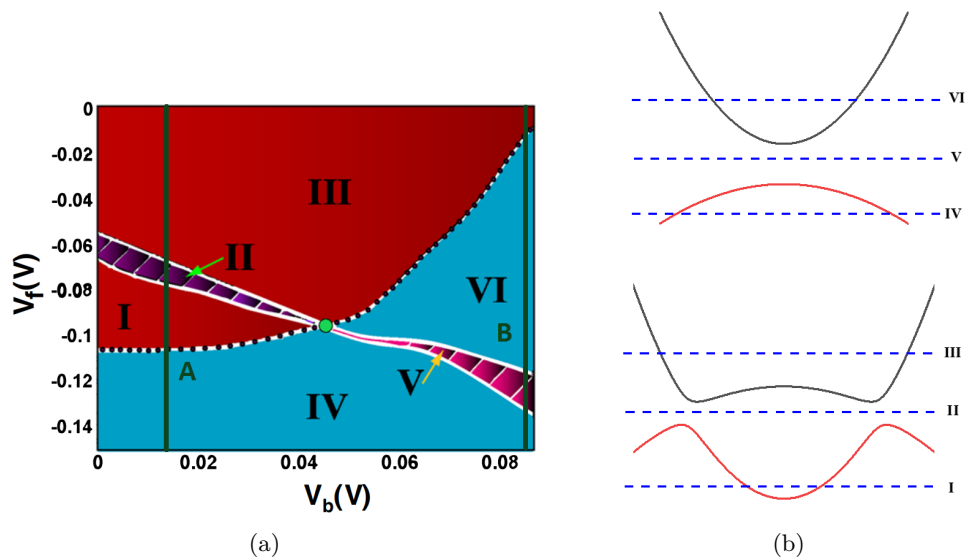


Figure 2.6: Fig. 2.6a shows an indicative phase diagram of an InAs/GaSb coupled quantum well under applied top ( $V_f$ ) and back ( $V_b$ ) gate biases. The top gate acts on the InAs layer, whereas the back gate acts on the GaSb layer. The system can either be inverted, with the associated electron-heavy hole anticrossing (shaded in red) or non-inverted (shaded in blue). The striped regions represent gapped regimes. Two top gate sweeps at a fixed back gate voltage are labelled A and B. Adapted from [5]. Fig. 2.6b shows schematically the electron-like (black) and hole-like (red) band structure in the non-inverted (top) and inverted (bottom) cases. Example Fermi energies for each region of Fig. 2.6a are highlighted by the blue dashed lines.

electron-like carrier density is modulated [9, 12, 38]. This might lead to the conclusion that, because the concentration of holes in the GaSb layer is negligible, an electric field applied to that layer will not be sufficiently screened from the InAs layer, and will instead act as an additional gate modulating the electron-dominated InAs layer [12]. However, if InAs/GaSb quantum wells grown using a high purity gallium source are compared to nominally identical samples grown using an impure source of gallium, the electron mobility is almost two orders of magnitude lower ( $30 \times 10^4 \text{ cm}^2\text{V}^{-1}\text{s}^{-1}$  at a carrier density of  $8 \times 10^{11} \text{ cm}^{-2}$  (pure) compared to  $0.8 \times 10^4 \text{ cm}^2\text{V}^{-1}\text{s}^{-1}$  at a carrier density of  $8.1 \times 10^{11} \text{ cm}^{-2}$  (impure)) [39]. This drop in mobility implies that electrons,

## 2.1 Band Structure of InAs/GaSb Coupled Wells

---

which should be localised within the InAs layer, can scatter off of impurities within the GaSb layer. This would seem to corroborate the theoretical prediction that the electron distribution extends significantly into the GaSb layer [25, 28]. Furthermore, Nguyen et. al. have observed unexplained features in the electron mobility when the carrier concentration is modulated solely through applying an electric field to the GaSb layer [9]. Specifically, they observe two maxima in the Hall mobility, where only one (arising from intersubband scattering, occurring as a new subband is populated [40]) is expected. As such, a more detailed investigation on the effect an electric field has on the electron dominated transport is of experimental interest. Such a study is undertaken in chapter 6.

There should be very few states available for transport mid-gap and therefore, a large increase in resistance is seen when the Fermi energy is within the gapped regime [33]. However, Fig. 2.6 shows why merely looking for a maximum in resistance as proof of a hybridisation gap is problematic. If we were to take two top gate sweeps at a fixed back gate voltage (labelled A and B on Fig. 2.6) we would initially (at  $V_f = 0$ ) see electron dominated transport (in regions III and VI), where the Fermi energy is pinned within the conduction band. As we apply a more negative top gate bias, the Fermi energy will enter a gapped regime (regions II and V) before finally hole dominated transport is seen (in regions I and IV), arising from the valence bands [5].

This presents an experimental challenge: how do we distinguish gate sweep A, where the Fermi energy enters the interesting, “inverted” hybridisation gap, from gate sweep B, where the (non-inverted) gapped regime is equivalent to that found in a normal semiconductor? One way is to apply a magnetic field in the plane of the sample [16, 35], and modify the momentum of the carriers within the quantum well. As before, we can approximate the Hamiltonian in the absence of an applied magnetic field as  $E = \frac{p_0^2}{2m^*}$ , where  $p_0$  is the momentum of the carrier in the absence of a magnetic field and  $m^*$  is the effective mass of the carrier. However, once we apply a magnetic field, the momentum becomes  $p = (p_0 + qA)$  and so the Hamiltonian becomes:

$$E = \frac{1}{2m^*}(p_0^2 + 2qAp_0 + q^2A^2) \quad (2.4)$$

where  $A$  is the magnetic vector potential and  $q$  is the charge on the particle. As the sign of  $q$  will be opposite for the electron-like states in InAs and the hole-like states in GaSb, the two dispersion relations will be shifted relative to one-another in momentum-space. As the electron band minimum moves away from the hole band maximum, a hybridised

dispersion will become distorted, creating states that are available for transport at energies that started as mid-gap. A schematic diagram of this distortion is shown in Fig. 2.7a. The creation of mid-gap states, available for transport, with application of an in-plane magnetic field will result in the resistance decreasing for the hybridised case. The non-inverted, unhybridised case will experience no such effect, as the size of the gap will not be affected by the application of small, in-plane magnetic fields, as shown schematically in Fig. 2.7b [11, 35, 41].

Once the origin of the high-resistance state has been established, the size of the hybridisation gap can be determined by temperature dependent measurements of the resistance. Initially, it was noted that the conductivity of an InAs/GaSb coupled quantum well, tuned into a gapped regime, changes significantly at 25 K, implying the hybridisation gap is of the order of 2 meV [33]. Later studies show that, above 2 K, the system can be described by an Arrhenius function with a similar 2 – 4 meV activation energy [10, 12].

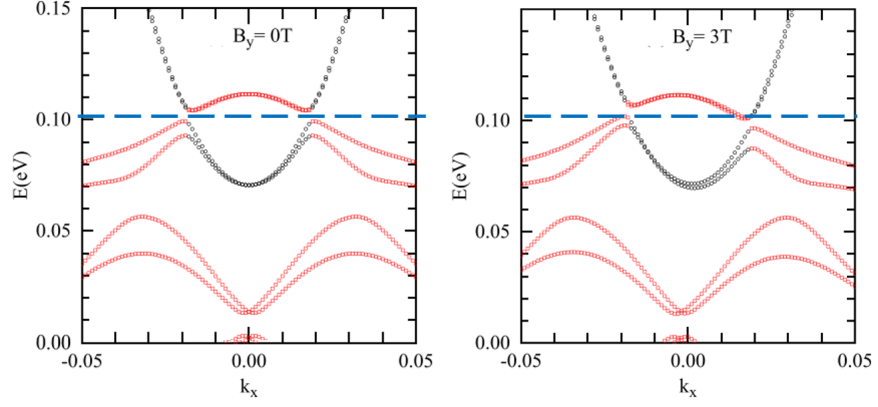
It is worth noting that the resistance of these inverted InAs/GaSb coupled quantum wells seems to saturate below 2 K, rather than diverging as one might expect for an insulating state [12]. This was found to be due to the broadening of the non-hybridised levels due to scattering. If a particle undergoes a scattering event, its tunnelling probability will be diminished [42]. In this coupled quantum well system, this diminished tunnelling probability will mean that a certain number of carriers will remain decoupled, as they will not be able to hybridise with the hole states. This will result in a finite number of mid-gap states and an associated mid-gap conductivity. In an ideal system, with a minimum of level-broadening, these mid-gap states will be localised, and the residual conductivity will tend to  $\frac{e^2}{h}$  [12, 43].

### 2.1.4 Modifying the hybridisation gap in InAs/GaSb coupled wells

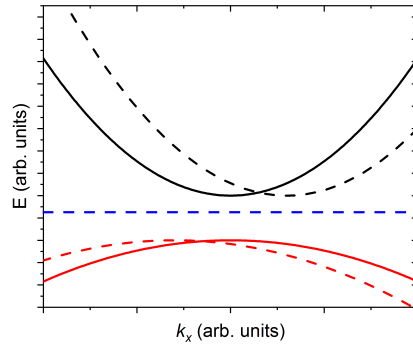
In this section, we consider the methods that can be used to tune the degree of hybridisation within InAs/GaSb coupled wells, and so alter the size of the hybridisation gap in energy. First, as the overlap between the electron and hole bands starts to vanish, the hybridisation gap will close [5, 30]. Secondly, it has been found that the higher the total number of carriers in the system, the weaker the hybridisation gap [10].

A more interesting scenario is one in which the inter-layer tunnelling is inhibited by insertion of a barrier between the InAs and GaSb layers, usually AlSb, which has a

## 2.1 Band Structure of InAs/GaSb Coupled Wells



(a)



(b)

Figure 2.7: Fig. 2.7a shows the in-plane dispersion relations for an InAs/GaSb quantum well in the absence of an applied field (left) and with 3 T applied magnetic field (right). The black (red) points represent states that were originally electron (hole) states prior to coupling. An example energy which is mid-gap in the absence of a magnetic field, but contains states available for transport in the presence of a magnetic field is highlighted by blue dashed lines. Adapted from [41]. Fig. 2.7b shows a schematic diagram of similar dispersion relations when the well is in the non-inverted regime. The solid lines denote states in the absence of a magnetic field, whereas the dashed lines denote the same states under a small in-plane magnetic field. Note that in this case, no mid-gap states are created by application of an in-plane magnetic field.

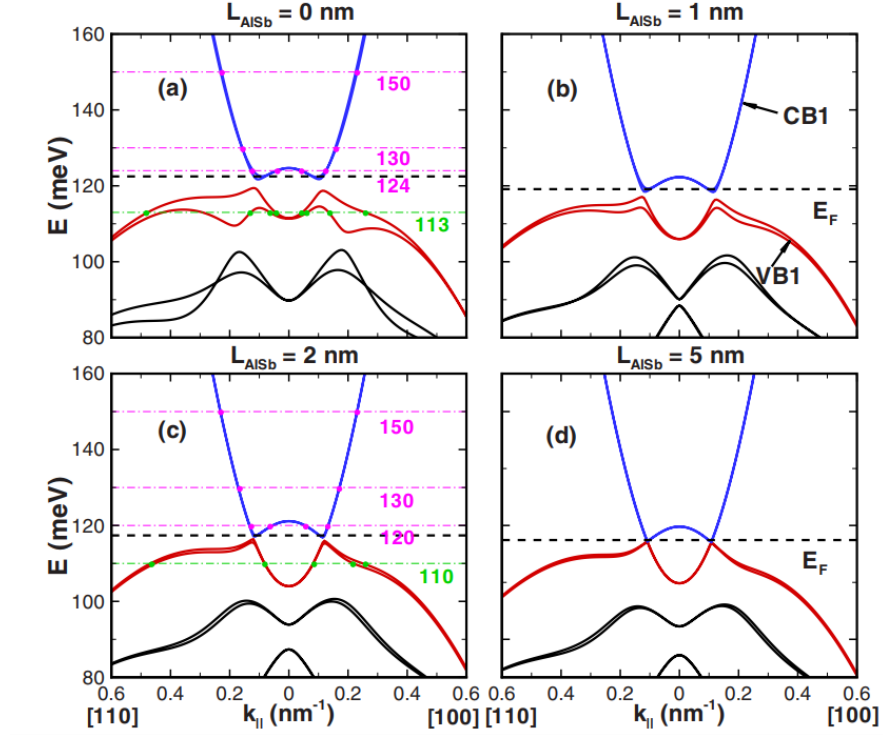


Figure 2.8: In-plane dispersion relations for the principal electron (blue), heavy hole (red) and light hole bands (black) for different thicknesses of AlSb spacers ( $L_{\text{AlSb}}$ ). From [44].

large band gap, as in Fig. 2.1. Naturally, this inhibition of tunnelling reduces the size of the hybridisation gap in energy, but this does not completely decouple the layers. In fact, it has been calculated that, while a 6 nm AlSb interlayer barrier will completely remove the hybridisation gap, at  $k_{\parallel} = 0$  the bottom of the conduction band will look like a heavy-hole band and the top of the valence bands will have the same curvature as the principal electron band. Additionally, a mid-well AlSb barrier will reduce the structural asymmetry within the quantum well, reducing the magnitude of the Rashba spin orbit coupling [44]. A schematic diagram of the effects an inter-layer AlSb spacer has on the band structure of an InAs/(AlSb)/GaSb quantum well is shown in Fig. 2.8.

A promising route for increasing the size of the hybridisation gap is through strain engineering. By matching the Fermi wavevectors in each layer, the electron-light hole hybridisation can be greatly enhanced. As more light holes are hybridised, the

electron-heavy hole hybridisation is similarly enhanced [23]. This wavevector matching is achieved by replacing the GaSb in the quantum well with  $\text{Ga}_x\text{In}_{(1-x)}\text{Sb}$ . With this, hybridisation gaps as large as 22 meV have been detected through temperature dependent measurements of the resistance when the system has been tuned into a mid-gap regime [14].

## 2.2 Magnetotransport of a 2DEG

Magnetotransport effects are an extremely powerful electrical method of probing 2D band structure in semiconductors. In the following section we will explore the magnetotransport phenomena seen in a 2DEG at low temperatures and the information we can extract from such measurements. For clarity, we will assume the device is oriented in the  $x, y$  plane, with a magnetic field oriented in the  $z$  direction.

### 2.2.1 Cyclotron motion and Landau levels

As in section 2.1.3, the momentum of a free electron in the presence of a magnetic field is given by  $p = (p_0 + eA)$ , where  $A$  is the magnetic vector potential such that  $B = \nabla \times A$ . We then choose;

$$A = Bx\hat{y} \tag{2.5}$$

so that  $B = B_z$ , i.e the magnetic field is applied solely out of the device plane. If we now re-evaluate the magnetic hamiltonian using this Landau gauge, we find:

$$\frac{\hbar^2}{2m^*} \frac{d^2\psi_x}{dx^2} + \frac{1}{2}m^*\omega_c^2(x - x_0)^2\psi_x = E\psi \tag{2.6}$$

where  $m^*$  is the effective mass,  $\psi_x$  is the wavefunction in the  $x$  direction, and  $\omega_c = \frac{eB}{m^*}$  is the cyclotron frequency. Equation 2.6 is a quantum harmonic oscillator in  $x$ , offset by  $x_0 = \frac{\hbar k_y}{m^*\omega_c}$ , with energies of:

$$E = \hbar\omega_c\left(\nu + \frac{1}{2}\right) \tag{2.7}$$

where  $\nu$  is an integer, known as the filling factor. As such, the energies of the system will be separated into discrete levels, with separation  $\hbar\omega_c$ , termed Landau levels. This describes the orbital motion of electrons around this magnetic field applied out of the device plane, wherein the angular momentum in the plane of the device is quantised into discrete cyclotron orbitals with a frequency  $\omega_c$ .

If thermal transitions can take place between these Landau levels, or if carriers can scatter (with a scattering time  $\tau$ ) before a cyclotron orbit is complete, then this quantisation is lost. Therefore, it is only at low temperatures (such that  $k_B T \ll \hbar\omega_c$ ) and high magnetic fields (such that  $\omega_c\tau \gg 1$ ) that these Landau levels will start to have an effect on the electronic transport [45].

### 2.2.2 The Shubnikov-de Haas effect

One manifestation of Landau level formation is the Shubnikov-de Haas (SdH) effect, characterised by oscillations in longitudinal resistance with increasing magnetic field. As we separate the energy of a 2D system into well quantised Landau levels, the density of states within the system will be similarly effected. However, the Fermi energy will not be affected by the application of an external magnetic field and so, as we apply a stronger magnetic field (and therefore increase the cyclotron frequency), the Landau levels sweep through the Fermi energy.

Within a Landau level, there will be a large density of states, with few, if any states between the Landau levels. This will result in periodic oscillations in resistance with increasing magnetic field. Equivalently, the magnetic field could be fixed, and the Fermi energy could be swept through the Landau levels with an applied gate bias [32]. An example of the oscillations in resistance with increasing magnetic field (with the accompanying Hall data shown in red), measured on a single GaAs/Al<sub>x</sub>Ga<sub>1-x</sub>As quantum well are shown in Fig. 2.9.

For a real sample, we have to include the effects of scattering and finite temperature on the density of states,  $g$ . The inclusion of these factors into the model complicates the derivation of the resistivity as a function of magnetic field and temperature  $\rho_{xx}(B, T)$  (derived in [46]) for spin degenerate Landau levels and isotropic scattering:

$$\rho_{xx}(B, T) = \frac{1}{\sigma_0} \left( 1 + 2 \frac{\Delta g(B, T)}{g_0} \right) \quad (2.8)$$

$$\frac{\Delta g(B, T)}{g_0} = 2 \sum_{s=1}^{\infty} \exp\left(\frac{-\pi s}{\omega_c \tau}\right) \frac{\Psi}{\sinh(\Psi)} \cos\left(\frac{2\pi E_F s}{\hbar\omega_c} - \pi s\right) \quad (2.9)$$

where  $E_F$  is the Fermi energy,  $g_0$  is the density of states in the absence of a magnetic field,  $\sigma_0$  is the conductivity in the absence of an applied magnetic field and

$$\Psi = \frac{2\pi^2 k_B T}{\hbar\omega_c}. \quad (2.10)$$

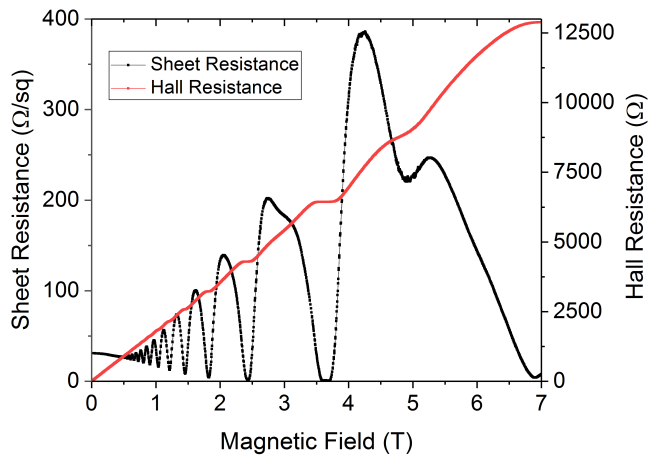


Figure 2.9: SdH oscillations (black) and quantum Hall data (red) measured on a GaAs/Al<sub>x</sub>Ga<sub>1-x</sub>As quantum well at 3 K. Note the position of the quantum Hall plateaux (which take values corresponding to integer fractions of the von Klitzing constant), and that the minima of the oscillations tend to 0 Ω resistance as we increase the magnetic field.

As such, we can see that the SdH oscillations are a good probe of the density of states at the Fermi energy. From equation 2.8, we can see that all the information the SdH oscillations can provide is enclosed within the density of states (equation 2.9), and as such is worth examining in some detail. We can see that equation 2.9 is a Fourier series composed of the product of three terms, which we will go on to describe in some detail.

The exponential term concerns the broadening of the Landau levels due to scattering [47]. As carriers scatter and their momentum changes, this will lead to a broadening of available energy states, as more momentum states become relevant to transport. This is usually parameterised by the FWHM of a broadened Landau level  $\Gamma = \frac{\hbar}{2\tau}$  [48]. As we increase the degree of scattering (and so decrease  $\tau$ ), it becomes more likely that a carrier will scatter before completing a cyclotron orbit, damping the observed oscillations.

The  $\frac{\Psi}{\sinh(\Psi)}$  term represents the thermal broadening of the Landau levels, via the Fermi-Dirac distribution function in the low temperature limit (i.e  $k_B T \ll \hbar\omega_c$ ) [46]. This low temperature limit is a safe approximation, as we require thermally activated

transitions between Landau levels to be negligible in order to observe oscillations in resistance.

The cosine term concerns the movement of the Fermi energy through the well defined Landau levels. For a 2DEG, the Fermi energy is directly proportional to the carrier density  $n$ , given by [49]:

$$E_F = \frac{\pi \hbar^2 n}{m^*} \quad (2.11)$$

as such, the period of the observed SdH oscillations in inverse magnetic field will be proportional to the carrier density responsible for these resistance oscillations, from equation 2.9. This  $\frac{1}{B}$  periodicity allows the SdH oscillations to act as a probe of the Fermi surface, as different states will have different energies, and so different carrier densities. For example, say we have a single GaAs/Al<sub>x</sub>Ga<sub>1-x</sub>As quantum well with two occupied electron-like subbands. These subbands will contain different carrier densities and have different effective masses, and so will produce SdH oscillations at different frequencies [40]. In fact, this is true of any degeneracy of the Fermi surface. Particularly interesting is the observation of beat frequencies in SdH oscillations within systems which experience spin-orbit coupling. As stated in section 2.1.1, asymmetries within a structure will create effective magnetic fields. These effective magnetic fields will split the dispersion relation, resulting in two states, a low energy state where the carrier spins are aligned to the internal field, and a high energy state where the carrier spins are aligned against this internal field [50, 51]. Each of these spin-states will produce a slightly different carrier density, and so we can calculate the magnitude of the SOC within a material from the beat frequency of the observed SdH oscillations [50, 52].

Interestingly, we can see from Fig. 2.9 that when the Fermi energy is between Landau levels, the observed resistance is 0  $\Omega$ . This is due to the resistivity tensor, given by:

$$\rho = \frac{1}{\sigma_{xx}^2 + \sigma_{xy}^2} \begin{bmatrix} \sigma_{xx} & \sigma_{xy} \\ -\sigma_{xy} & \sigma_{xx} \end{bmatrix} \quad (2.12)$$

where  $\sigma_{xx}$  is the conductivity parallel to the current, and  $\sigma_{xy}$  is the conductivity at right angles to the current. For example, the component of the resistivity in the  $x$  direction is  $\rho_{xx} = \frac{\sigma_{xx}}{\sigma_{xx}^2 + \sigma_{xy}^2}$ , and so if there is a significant  $\sigma_{xy}$  component (i.e the Hall voltage is non-zero), when the Fermi energy is between two Landau levels, where there are no states at the Fermi energy, i.e  $\sigma_{xx} = 0$ , the resistivity is also zero. If the observed

resistance does not approach  $0 \Omega$ , this may be an indication that there is an additional conduction channel present. After all, if there is still a sizeable density of states at the Fermi energy (either because of an additional set of Landau levels, or if the other conduction channel is not quantised into Landau levels at all) there will still be a significant conductivity along the current direction (i.e  $\sigma_{xx} \neq 0$  and therefore  $\rho_{xx} \neq 0$ ) [37].

Equations 2.8 and 2.9 were derived for Si inversion layers, where a 2DEG could be obtained by applying a gate bias to a heavily p-doped layer of Si. In such a system, the scattering can be modelled as isotropic, so every scattering event will contribute to the zero-field conductivity,  $\sigma_0$ , and also to the broadening of the Landau levels due to scattering,  $\Gamma$ . However, in GaAs/Al<sub>x</sub>Ga<sub>1-x</sub>As quantum wells (such as in Fig. 2.9), extracting  $\tau$  from the SdH oscillations consistently underestimates  $\sigma_0$  [53]. This disparity is due to the remote nature of the impurities within quantum well heterostructures. By separating the impurities from the 2D transport channel in space, the impurities will be screened from the channel [54]. If we consider impurities as potential barriers, this screening will reduce the height of these barriers, making small angle scattering events more likely [55]. However, scattering events that contribute to  $\sigma_0$  are weighted towards large angles by  $(1 - \cos(\theta))$  where  $\theta$  is the scattering angle. Therefore, it is helpful to define two scattering times; the transport scattering time,  $\tau_t$ , weighted towards large angle events, and the quantum lifetime,  $\tau_q$ , which is the timescale over which the carrier's momentum is well defined, and thus includes all scattering events. The ratio of these two parameters is known as the Dingle ratio;  $\alpha = \frac{\tau_t}{\tau_q}$ . Crucially, every scattering event will contribute to the broadening of the Landau levels, and so in equation 2.9,  $\tau = \tau_q$ . However, the  $\sigma_0$  depends only on the transport scattering time,  $\tau_t$ , and so equation 2.8 considers both scattering time-scales.

### 2.2.3 The Integer Quantum Hall Effect

From Fig. 2.9, we can see that the Hall resistance (red trace) forms plateaux as the Fermi energy moves between Landau levels (i.e the measured sheet resistance approaches  $0 \Omega$ ). Additionally, we note that the observed value of the Hall resistance at these plateaux is an integer fraction of one over the conductance quantum,  $\frac{h}{e^2}$  (known as the von Klitzing constant). In fact, these plateaux are quantised to such a degree that they can be used as a standard for electrical resistance [56]. This quantisation

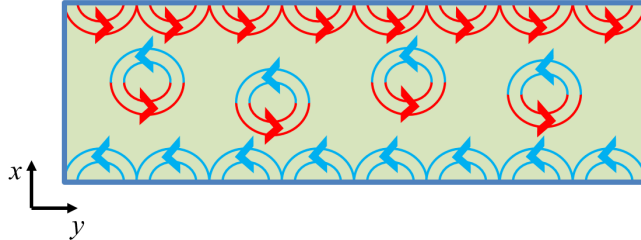


Figure 2.10: Schematic of cyclotron motion within a finite sample, when the Fermi energy is between the second and third Landau levels. Two edge states are observed running around the sample perimeter, whereas the bulk states are localised in closed cyclotron orbits and therefore cannot carry any current. Left-moving carriers are shown in blue, and right moving carriers are shown in red.

is also extremely robust against sample impurities, depending purely on the carrier density within the system and the charge of the carriers. This makes it a powerful tool to deconvolute the concentration of the electron and hole gases within an InAs/GaSb quantum well, as the SdH effect does not discriminate between carriers of different charges.

This integer quantum Hall effect (IQHE) is best explained by re-examining the cyclotron motion of electrons in a finite sample. Equation 2.6 assumes that there is no potential acting on the carriers, and while this may be a good approximation in the bulk of the sample, at the edges there will be a large confining potential as the carriers cannot escape the material. As the carriers cannot escape the material, neither can their cyclotron orbits, therefore orbits close to the sample edge will be cut off, producing so called “skipping orbitals” as in Fig 2.10.

Fig. 2.10 illustrates why the integer quantum Hall effect is so robust against disorder. As the cyclotron orbits will rotate in a certain direction (determined by the direction of the field and the charge of the carriers), each edge state will also have a set direction associated with it. The main consequence of this is to eliminate any possibility of back-scattering within these edge channels, e.g in Fig. 2.10, a left moving carrier travelling along the bottom edge has no right-moving states to scatter into [56].

However, the existence of these edge channels doesn’t necessitate a quantised Hall resistance. Therefore, to explore the quantised nature of the Hall voltage, we adopt

the approach used by Laughlin [57, 58]. In order to show that, in the high magnetic field limit, the Hall resistance should be quantised we should again examine equation 2.6, or more specifically the centre of the harmonic potential,  $x_0$  and our magnetic vector potential,  $B = \nabla \times A$ . If we consider the surface depicted in Fig. 2.10 not as a flat surface with a magnetic field applied out of the plane of the page, but as a ring with a radial magnetic field, a number of properties will emerge. This system is shown schematically in Fig 2.11a.

Firstly, we require a periodic boundary condition. The wavefunction of a particle at any position  $y$  must be identical to the same particle at  $y + L$  where  $L$  is the circumference of the ring. Therefore, to maintain phase coherence, the momentum of the particle in the  $y$  direction must be quantised as  $k_y = \frac{2\pi N}{L}$ , where  $N$  is an integer.

Next, we alter the gauge so that:

$$A' = A + \frac{\Phi}{L} \hat{y} \quad (2.13)$$

where  $A$  is the Landau gauge from equation 2.5 and  $\Phi$  is a constant. Note that, as before,  $\nabla \times A' = B_z$ , so by introducing  $\Phi$  we have not changed the system. Physically,  $\Phi$  can be thought of as a flux passing through the centre of the ring from Faraday's law. The only alteration made to the Hamiltonian (equation 2.6) from this change is

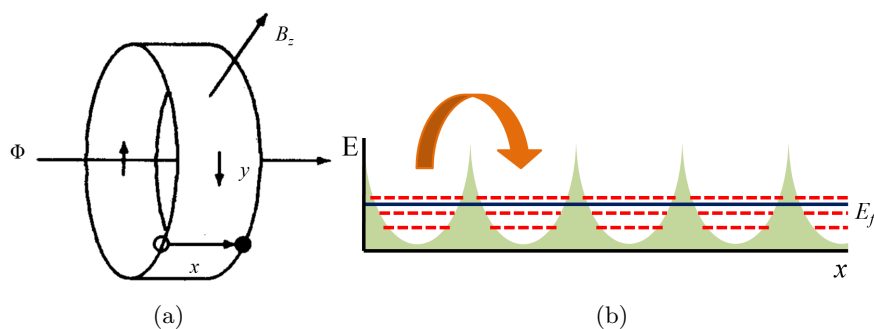


Figure 2.11: Schematic representations of the Laughlin pumping argument. Fig. 2.11a shows the model system considered, adapted from [58]. Fig. 2.11b shows the potential landscape of the system shown in Fig. 2.10, with the Landau levels shown in red, the Fermi energy shown in blue, the harmonic potential shown in green, and a cycle of the effective Laughlin pump shown in orange.

that our value of  $x_0$  shifts as:

$$\frac{hN}{m^*\omega_c L} \Rightarrow \frac{h}{m^*\omega_c L} \left( N - \frac{\Phi}{\phi_0} \right) \quad (2.14)$$

where  $\phi_0 = \frac{h}{e}$ , the magnetic flux quantum. Changing  $\Phi$  (by application of an electric field in the form of a current in the  $y$  direction) will result in a shift in the  $x$  centres of the cyclotron orbits. If  $\Phi$  is changed such that  $\phi_0$  extra flux is passed through the ring (i.e the current completes a circuit around the loop) this will map the position of the  $N^{\text{th}}$  “well” onto where the  $N - 1$  used to be. This can be repeated  $N$  times to create a system of harmonic potential “wells” spanning the width of the sample [59].

One way of thinking of this problem is to consider the harmonic potential in  $x$  as a cross-section of an Archimedes screw pump. When the Fermi energy is between two Landau levels, each potential “well” must contain an integer number of carriers. Applying a current in the  $y$  direction, so that  $\Phi$  increases by one flux quantum, will constitute one cycle of the pump, removing an integer number of carriers from one edge and depositing them on the opposite side. So long as an integer number of Landau levels are filled (i.e the Fermi energy is in-between two Landau levels) there will be an integer number of charges transferred from one edge to another and so Hall conductance must also be quantised. A cycle of this pump is shown schematically in Fig. 2.11b.

We note that, up to this point, we have been ignoring the spin of the charge carriers in our treatment of the IQHE. However, we note from Fig. 2.9 that most of the observed plateaux occur at even integer fractions of the von Klitzing constant. Additionally, at  $\approx 5.3$  T, a plateau with a filling factor,  $n = 3$  appears to develop, coincident with a split SdH maximum. This is indicative of Zeeman splitting around the applied magnetic field. Ordinarily, it is safe to assume that the Landau levels are spin degenerate (so only even integer plateaux are seen), but in the limit of extremely low temperatures and high magnetic fields, the Landau levels become spin-split. These spin-split plateaux are much more sensitive to changes in the sample temperature, as the energy scale of the Zeeman splitting is far less than the inter-Landau level separation [60].

### 2.2.4 Magnetotransport within InAs/GaSb coupled wells

Once we start adding additional channels, such as transport through an impurity layer, the quantised nature of the IQHE will break down. If there are any states available at the Fermi level, the number of electrons carried by each harmonic “well” (as in Fig.

2.11b) no longer has to be an integer, and so the quantised values of Hall resistance is lost [37]. This is of particular importance when studying the magnetotransport of InAs/GaSb quantum wells, where both the InAs well and GaSb well can support transport in n and p-type channels, respectively.

One of the more common indicators of two carrier transport is the “bending” of the ordinary Hall trace with increasing magnetic field [37, 61]. Under the ordinary Hall effect (OHE), charge carriers experience a Lorenz force (proportional to the applied magnetic field), causing a build-up of charge on one side of the device. This charge build-up leads to a transverse voltage, proportional to the carrier density within the material, otherwise known as a Hall voltage. This Hall voltage is commonly reported as a Hall resistance.

However, in the presence of two carriers, this is somewhat more complicated. This is because the Hall resistance will not only be proportional to the carrier density, but also proportional to the relative mobilities of the individual carrier species. This is only the case when conventional scattering dominates the movement of charge within the material. When cyclotron motion plays a dominant role, this dependence on the relative carrier mobilities drops out. This leads to two regimes of the ordinary Hall effect, where the gradient of the Hall resistance with respect to magnetic field (otherwise known as the Hall coefficient,  $R_H$ ) is described (in the case of parallel electron-hole transport) by [37]:

$$R_H = \begin{cases} \frac{p-nb^2}{e(p+nb)^2}, & \text{if; } \omega_c\tau_q \ll 1 \\ \frac{1}{e(p-n)}, & \text{if; } \omega_c\tau_q \gg 1 \end{cases} \quad (2.15)$$

where  $p$  and  $n$  are the hole and electron carrier densities, respectively, and  $b$  is the ratio between the electron and hole mobilities.

From equation 2.15, we can see why the Hall response is non-linear in the presence of multiple charge carriers. As the magnetic field is increased, and we move into the high field ( $\omega_c\tau_q \gg 1$ ) regime, the Hall coefficient loses its dependence on the ratio between the electron and hole mobilities,  $b$ , and so the gradient of the Hall resistance with respect to magnetic field will change [62].

As stated above, if there are an appreciable number of states at the Fermi energy, the SdH oscillations will no longer approach  $0 \Omega$  resistance, and the quantum Hall plateaux will deviate from their well quantised values. However, it is possible to select an applied magnetic field such that the Fermi energy is between Landau levels in both

the InAs and GaSb wells simultaneously. When this is the case, the SdH oscillations will approach  $0 \Omega$ , and the quantum Hall plateaux will form with a quantised resistance of an integer fraction of the von Klitzing constant, where the total filling factor is the difference between the filling factor in the InAs well and the filling factor in the GaSb well [18].

However, once one decouples the individual wells, this picture starts to become more complex. The reduction of coupling between the electron and hole dispersions leads to the two wells acting independently, resulting in two distinct carrier concentrations contributing to transport [61]. This is in contrast to the strongly hybridised case, where the transport appears dominated by a single carrier gas [33].

This is supported by optical measurements of the effective mass, via cyclotron resonance, of coupled quantum wells with varying degrees of hybridisation. In the strongly hybridised case, a single resonance peak is seen, corresponding to a single effective mass, and thus a single carrier type [63]. However, as the separation between the electron and hole gases is increased, either by increasing the respective well thickness [64, 65] or by inserting a spacer layer between the two active layers [66], the linewidth of the cyclotron spectrum increases, until the wells are completely decoupled [61]. This increase in linewidth (correlated with increased scattering [67]) was attributed to the electrons within the InAs layer scattering off of unhybridised holes within the GaSb layer [61, 66]. Once the inter-layer separation increases to such an extent that the two carrier can no longer interact, the cyclotron spectrum becomes analogous to a single, uncoupled, InAs quantum well.

It is worth noting that, while the magnetotransport behaviour of both the strongly coupled [33, 38] and the completely decoupled [18] quantum wells have been studied extensively, little attention has been paid to the transport in the partially coupled case. Such a case would be of experimental interest, as there should be an appreciable number of hole-like states available for transport, unlike the strongly hybridised case. Additionally, unlike the completely decoupled case, the electron-hole interactions should show interesting integer quantum Hall behaviour, where the measured filling factor arises from the difference between the electron and hole filling factor. Of particular interest would be whether SdH oscillations due to holes would be visible in such a system. In the strongly hybridised system, the electron and hole states are separated by the hybridisation gap, and in the uncoupled system the SdH oscillations are dominated by

the much higher mobilities found in the InAs 2DEG. Such a partially coupled scenario is explored in chapter 5.

## 2.3 The Quantum Spin Hall Effect

Fig. 2.10 highlights an interesting effect of the IQHE, that of the directionality of the skipping orbitals. As stated, the fact that the cyclotron orbits rotate in a given direction prohibits backscattering, making these edge states dissipationless. However, the high magnetic field needed to tune the system into a state where cyclotron motion becomes dominant limits the potential applications of such a state. If a state dominated by ballistic transport similar to the IQHE can be found in the absence of magnetic fields, it would certainly be of extreme experimental interest. InAs/GaSb coupled quantum wells are a candidate material to show such a state, known as the quantum spin Hall effect (QSHE), which we shall cover for the remainder of this chapter.

### 2.3.1 Theory of the QSHE

Figs 2.3 and 2.7a shows that, for this class of coupled quantum wells, near  $k_{\parallel} = 0$  the dispersion relation of the conduction (valence) band looks like a conventional hole (electron) dispersion, in contrast to the conventional, non inverted case, shown in Fig. 2.7b. If we just consider the curvature, and thus their effective mass, it appears near  $k_{\parallel} = 0$  that the conduction band has a negative effective mass. However, the bands of the AlSb barriers are analogous to those of a conventional semiconductor, containing a conduction band with a positive effective mass and a valence band with a negative effective mass. Additionally, there is no transition available to the state that both restores the conventional curvature of the bands and does not close the gap [5]. Specifically, we can realise this “protection” by reconsidering equation 2.3. We have stated in section 2.1.2 that the effective coupling between the lowest electron-like subband and the highest energy hole-like subband ( $\Delta$  in equation 2.3) goes to 0 as  $k_{\parallel}$  approaches 0 [4]. As such, as  $k_{\parallel}$  approaches 0 the conduction band must also adopt the behaviour of the highest heavy hole subband, including its curvature. This is often known as an “inverted” band gap.

However, this poses a problem. The region inside the quantum well with a negative effective mass in the conduction band has to be connected to the AlSb layers

surrounding the coupled quantum well. As this cannot be achieved with the hybridisation discussed earlier, we require that the system goes through some new, critical state, where the gap first closes, then re-opens with a conventional band alignment [6]. As this state is, in essence, a transition between a region of negative effective mass to a region of positive effective mass, it can be thought of as a domain wall containing a region of 0 effective mass.

Within the presence of strong SOC, the spins of current carriers will be related to their momentum. As in section 2.1.1, an electric field is seen by relativistic carriers as an effective magnetic field. We can also include the intrinsic SOC from the nuclear electric field as well as the electric fields due to asymmetries within the structure. Just as a conventional magnetic field gives rise to a Lorentz force, and thus the ordinary Hall effect, these effective magnetic fields can selectively deflect carriers by coupling to their spin, resulting in the spin Hall effect. Under the spin Hall effect, application of a charge current will lead to a selective deflection of spin-states to one side. However, as this picture does not include an external magnetic field, the system must obey time reversal symmetry, and thus Kramer's theorem applies. By this theorem, every time reversal symmetric state  $k_{\rightarrow\uparrow}$  will have a twin state with  $k_{\leftarrow\downarrow}$ . A material that experiences the spin Hall effect will, therefore, have transport of spin-up carriers moving towards one edge, balanced by transport of an equal number of spin down carriers moving towards the opposite edge [68]. Such a spin-current will result in a net transport of spin to one side of the device without a net transport of charge.

This time inversion symmetry, and the Kramer's degeneracy that arises from it, is a crucial part of the QSHE. As long as time reversal symmetry remains unbroken, left moving particles will experience one effective magnetic field from the SOC, whereas right moving particles will experience an effective magnetic field which is exactly opposite. As such, just like the conventional spin Hall effect, opposite currents will be induced for opposite spins [69]. Additionally, again by Kramer's theorem, as  $\psi(+K)$  must be equal to  $\psi(-K)$  (where  $K$  is the total momentum, accounting for spin), any gap-closing state must cross the energy gap at either the centre or the edge of the Brillouin zone, as otherwise there would be an asymmetry between  $\pm K$  [70].

By now we have a coherent picture of this gap-closing mechanism. It must be described by a state with a linear dispersion (and thus have no effective mass), that crosses the gap at a high-symmetry point of the Brillouin zone. In addition, due to the

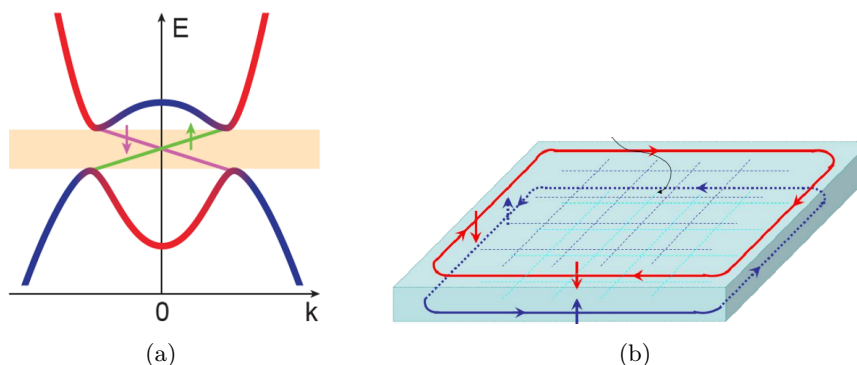


Figure 2.12: Fig. 2.12a shows schematically the band structure of an InAs/GaSb quantum well, highlighting the electron-like dispersion (red), the hole-like dispersion (blue), the hybridisation gap (yellow) and the QSHE edge states (pink and green). From [17]. Fig. 2.12b shows the edge states of a material in the QSHE state, with spin down shown in red and spin up shown in blue. From [72]

SOC within our QSHE material, combined with the Kramer's degeneracy enforced by time reversal symmetry, there must be a pair of gap closing states, where the spin of a carrier traversing one of these states is locked to its direction of travel. Such a state will give rise to two 1D spin polarised channels running around the sample exterior. One of these states will carry one spin state clockwise, and the other, carrying the opposite spin state, will move anticlockwise [5, 69–71]. A schematic diagram of these states in  $k$ -space, and the real-space edge states created by them is shown in Fig. 2.12.

In the ideal case, where we only consider the SOC from the nuclear electric field (i.e when the electric field lies only within the sample plane), the spins within a QSHE material point exclusively out of the plane of the device [70]. However, when we consider the Rashba and Dresselhaus SOC, which arise due to the asymmetries mentioned earlier [27], the electric field that gives rise to the SOC is no longer confined to the sample plane. Therefore, the spin-states within the QSHE will be tilted, away from their out of plane polarisation [19, 20]. It is worth noting that these additional sources of SOC still do not break time reversal symmetry, and the edge modes arising from the QSHE state will be preserved [5], but their spin quantisation axis will become  $k$  dependent [19, 20]. A schematic diagram of these so-called generic helical edge modes is shown in Fig. 2.13.

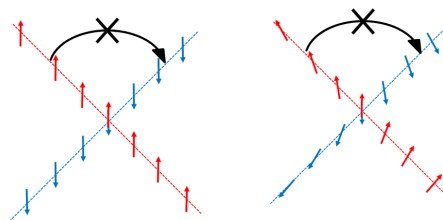


Figure 2.13: Schematic dispersion of QSHE states in the perfectly out of plane polarised case (left) and in a generic helical edge mode case (right) [19]. In both cases, a forbidden elastic backscattering event is shown in black.

While the Dresselhaus SOC will alter the quantisation axis into  $k$  dependent generic helical edge modes for any QSHE system [20], only higher order Rashba terms will be able to achieve this, as the conventional,  $k$ -linear, Rashba SOC will only be able to form these generic helical edge modes when particle hole symmetry is broken [19]. This makes the deconvolution of these SOC terms of experimental interest, particularly in InAs/GaSb coupled quantum wells, where both asymmetries (structural inversion asymmetry from the unusual stack structure and bulk inversion asymmetry from the zinc-blende crystal structure) are present [5, 19]. While some preliminary work has been undertaken [38], the dependence of the Dresselhaus SOC on various parameters such as gate voltage and small differences in growth conditions have not been explored. Additionally, the effect of an applied gate bias on the internal electric field arising from the stack asymmetry has not been discussed. We explore these concepts and determine the relative magnitudes of the Rashba and Dresselhaus SOC in chapter 7.

### 2.3.2 Experimental Signatures of the QSHE

Ideally, the QSHE would be investigated by measuring a quantised spin Hall voltage [70, 72]. Unfortunately, directly measuring a spin accumulation is difficult, especially in semiconductors, where a ferromagnet-semiconductor interface may act as a spin-scattering site, destroying spin information present [73]. Additionally, the quantised nature of the QSHE could be disrupted by strong spin-orbit coupling [6, 19]. As such, the QSHE is usually recognised by its ballistic, helical transport.

As each sample edge contains a pair of counter-propagating edge states, one might naively think that there is a natural back-scattering path. However, Fig. 2.13 shows

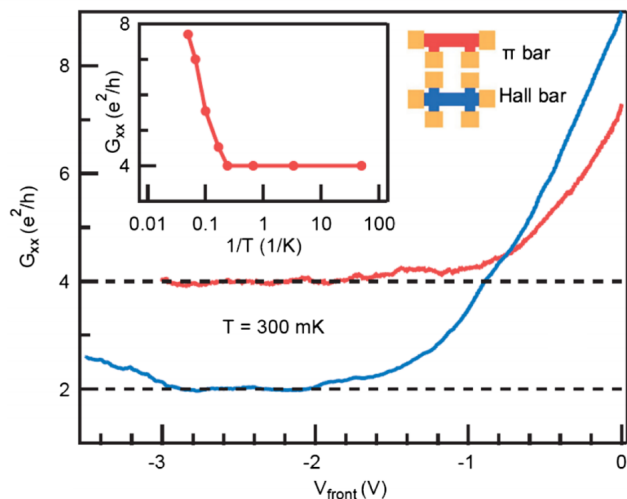


Figure 2.14: Longitudinal conductance as a function of applied top gate bias in a symmetric Hall bar, and an asymmetric “ $\pi$ ” bar, showing the doubling of conductance (halving of resistance) with the removal of two contacts. The inset shows the conductance of the “ $\pi$ ” bar structure as a function of  $\frac{1}{T}$ , showing that the conductance is quantised below a sample temperature of 4 K. From [13]

why conventional elastic back-scattering is forbidden. To move from a state with positive  $k$  to a state with the same energy but negative  $k$ , a  $180^\circ$  spin flip is required. Note that this remains true even in the presence of generic helical edge modes [19]. As such, the longitudinal resistance in a QSHE material should be quantised at  $R = \frac{h}{2e^2}$ , representing two, current carrying edge modes, carrying opposite spins on opposite sides of the device [71].

An interesting property of the QSHE is the helical nature of the edge modes. Unlike in the IQHE, where each sample edge contains carriers moving in one direction, under the QSHE each sample edge contains a pair of counter propagating edge states [72]. Therefore, if we apply a current along the length of a device, in any direction, that current will be carried along each sample edge. Additionally, when this current leaves the QSHE material, e.g. at a metal-semiconductor interface, the coherence of the QSHE state will be destroyed, leading to the creation of a new set of edge modes as the current re-enters the QSHE material.

This property can be measured by comparing the longitudinal resistance in a sym-

metric Hall bar to an asymmetric “ $\pi$ ” bar. In the first case, the quantised resistance of  $R = \frac{h}{2e^2}$  can be measured, whereas the latter case will show a resistance of  $R = \frac{h}{4e^2}$ . As we remove two metal-semiconductor interfaces from the “ $\pi$ ” bar, we create a device that supports one edge with a single pair of edge modes (which we can’t measure) and one edge with three sets of edge modes (one between the current source and the first measurement contact, one between the measurement contacts and one between the second measurement contact and the current drain). If we think about this as a network of resistors connected in parallel, it is easy to see that the current in the device will be split, with the undisrupted edge carrying the majority of the current. This leads to the halving of the measured resistance, as shown in Fig. 2.14 [13].

This can be detected in HgTe/CdTe quantum wells, where the “inverted” band gap is achieved through the strong intrinsic SOC within the HgTe quantum well material [69]. However, we have established that the conductivity within the hybridisation gapped regime in InAs/GaSb coupled wells is not zero [12, 43], and so there remains a significant number of bulk states that contribute to the conductivity when the system is in the QSHE state. This can provide a possible back-scattering path in the QSHE state, and so should be suppressed if the properties of this state is to be studied in detail.

Two methods have currently been developed to enhance the mid-gap resistance, but the principle behind both is the same. Both methods aim to introduce impurities into the quantum well structure and so localise the mid-gap states, limiting the number of bulk conduction channels. This is achieved either by inserting a layer of Si  $\delta$ -dopants at the InAs/GaSb interface [13, 74] or by using an impure source of Gallium during the quantum well growth, equivalent to doping the GaSb layer with  $\approx 1\%$  Al impurities [39]. As long as the hybridisation between the two wells is not disrupted by these impurities, the QSHE state should be robust against this disorder, due to the lack of elastic backscattering within this regime.

This lack of elastic backscattering is, like most of the QSHE, protected by time-reversal symmetry. However, once we break this symmetry, by applying an external magnetic field, this protection also breaks down. In the presence of Dresselhaus SOC, the applied magnetic field couples the spin-up and spin-down carriers, resulting in elastic backscattering events being permitted, destroying the quantised resistance. We still require a transition out of the inverted regime, but now the edges are characterised

by spinless 1D wires, which can easily be cut-off by disorder [75]. As the conduction through the QSHE state is characterised by mid-gap states that are protected by the symmetry of the material system, QSHE materials are often referred to as two-dimensional topological insulators (2DTI).

This disruption of the quantised longitudinal resistance with an applied magnetic field should be true for any magnetic field orientation. However, as the Dresselhaus SOC should be strongest along the out of plane  $z$  direction, applying a magnetic field along this direction should result in the largest deviation from the quantised resistance. Additionally, if a magnetic field is applied in the device plane, it should not matter what angle this field makes with respect to the edge states, as the magnetic field should now couple to the intrinsic SOC, and couple the spin-up and spin-down states in that manner [75]. While this is certainly true for HgTe/CdTe quantum wells [76], and strained InAs/Ga<sub>x</sub>In<sub>(1-x)</sub>Sb quantum wells [14], an applied in-plane magnetic field does not destroy the quantised resistance of InAs/GaSb quantum wells [13]. It is unclear why this is the case. In fact, the quantisation of the resistance seems to persist up to 12 T applied in-plane magnetic fields, with little in-plane anisotropy [13]. This is unexpected, as Fig. 2.7a shows that we would expect a relatively small in-plane magnetic field to result in the creation of mid-gap states [41], which should dominate transport over the QSHE edge states.

It has been proposed that the QSHE system in InAs/GaSb coupled quantum wells forms an excitonic state, where the electrons and holes become bound to each other by the long range Coulomb interaction [77]. In such a state, a gap opens in the Fermi surface, analogous to the gap formed in BCS superconductivity [78]. Rather than being proportional to the indirect electron-heavy hole coupling through the admixture of light holes that tunnel into the InAs layer from the GaSb layer, the size of the excitonic insulator gap will be inversely proportional to the pair-density. As the density of electron-hole pairs is increased, there will be a greater screening from the Coulomb interaction, weakening the coupling between electron and heavy-hole states [10]. The energy gap in such a state should not close as an in-plane field is applied, as the Coulomb interaction should not be modified by an in-plane magnetic field. As such, application of an in-plane magnetic field will merely shift the position of the gap-closing point in  $k$ , and should not necessarily open a gap in the edge state dispersion [13].

Finally, we should mention the evidence for spin-polarised transport within the

QSHE state. In HgTe/CdTe quantum wells, this was demonstrated by the spontaneous generation of a spin current at the device edge, where the majority of spins are polarized out of the device plane [79]. In InAs/GaSb coupled quantum wells, spin-polarized edge transport was shown through study of Josephson junctions in which the InAs/GaSb was used as a non-superconducting spacer. In this case, devices showed superconducting quantum-interference-like behaviour with a doubled periodicity compared to ordinary Cooper-pair mediated superconducting quantum interference devices, indicating that not only is transport dominated by edge states, but that there is also some separation of spin states along each channel edge [17].

---

# CHAPTER 3

---

Wafer Growth and Device Fabrication

All of the InAs/GaSb coupled quantum well devices discussed in this thesis were first grown by molecular beam epitaxy (MBE) and then patterned into devices in a clean-room environment. This chapter will briefly cover the growth and physical characterisation of as-grown wafers before discussing the fabrication of InAs/GaSb coupled quantum well devices for transport measurements. Where appropriate, we will focus on the process optimisation necessary to achieve high performance devices.

### 3.1 Molecular Beam Epitaxy of InAs/GaSb wafers

InAs/GaSb wafers were grown by MBE using three separate systems. Wafers marked with “SF” were grown in 2014 by Dr Shiyong Zhang at the University of Sheffield and wafers marked “G” were grown by Dr Lianhe Li at the University of Leeds between 2016 and 2017. We also received a piece of a wafer (C1295) from the University of Cambridge’s Cavendish Laboratory, grown by Professor Edmund Linfield in 1997.

Structures grown by MBE are single crystal, and extremely high quality, leading to high electrical mobilities within the structure. In MBE, the elements required to be deposited are heated until they vaporise. These component elements then diffuse towards the target substrate, where they settle and react with other elements that impinge on the substrate simultaneously (for example, the InAs in our structures will be deposited by simultaneously exposing the substrate to In and As sources).

As the MBE chamber is pumped to an ultra high vacuum and no carrier gases are used, the evaporated material moves as a ballistic beam, not interacting with background gas or other source beams until it reaches the substrate. This leads to an isotropic deposition on the sample, and can give very tightly controlled surface properties and single-crystal layers. These properties are essential for the fabrication of 2D electronic materials [80].

As the mean free path within the elemental beams is much larger than the MBE chamber itself, the substrate surface is where all reactions occur. Once an incident atom has been adsorbed onto the surface, it will diffuse around the crystal sites on the substrate until it is either incorporated into the crystal lattice or it is re-evaporated off the surface. As such we need to find the right balance between the substrate-atom binding energy and the mobility of the atom on the surface. This is influenced by an extremely large parameter space, including the background pressure, substrate temperature, the source material and the incident flux of material, which need individual

### 3.1 Molecular Beam Epitaxy of InAs/GaSb wafers

---

optimisation.

If the evaporated atoms are bound more tightly to each other than the substrate surface, large islands of material will nucleate and grow, eventually covering the full material surface. Due to the roughness this can cause, and the fact that layers grown by this mode can be amorphous rather than crystalline [81], this growth mode is not desirable. Therefore the optimal growth mode will arise when the mobility of atoms is high, and the source atoms are much more tightly bound to the substrate than to other source atoms. This will result in layers of material building up on the substrate surface. As the source molecules are bound more tightly to the surface of the substrate than each other, in the ideal case, a complete monolayer will form before the next one is nucleated. This is known as layer-by-layer growth.

Additionally, we desire tight control over the stoichiometry within our material. However, for the III-V group of semiconductors (of which InAs, GaSb and AlSb are all members) this is complex. The group V element (As or Sb) typically has a lower vapour pressure than its counterpart group III element (In, Ga or Al), and so can be evaporated at a lower temperature. However, to maintain layer-by-layer growth, the substrate temperature needs to be high enough that the group III element is sufficiently mobile, which may be hot enough to evaporate the group V element. Therefore, the group V element will quickly re-evaporate from the surface unless met with a group III atom to bond to, whereas the group III adatoms will be tightly bound to the substrate. Hence, if the flux of the group V element is kept significantly higher than the flux of the group III element, the growth rate can be controlled solely with the flux of the group III element. Any excess group V element is then re-evaporated from the substrate, maintaining the required stoichiometry. This III-V ratio, and the substrate temperature maintained are crucial parameters involved in MBE process optimisation [80].

Finally, it is worth considering the bonds formed between layers of different materials during epitaxial growth. For example, the interface between an InAs layer and an antimonide, say, GaSb, has a roughly equal probability to form InSb or GaAs. As the lattice constant of AlAs and GaAs are both smaller than the lattice constants of InAs, GaSb and AlSb [21], a mixed or arsenide based interface will apply a strain to the lattice, creating defects and scattering sites. Therefore to create a constant interface we need InSb-like interfaces. This is achieved, for the case of growth of InAs on the AlSb

quantum well barriers, by terminating the growth of AlSb with an antimony soak, and starting the growth of InAs with an indium soak. This should lead to the formation of a monolayer of InSb at the interface, which should improve the transport properties of the quantum well [22].

### 3.2 AFM Studies of as grown GaSb

In order to optimise the interfaces within the quantum well, we need to optimise the growth parameters of the layers and, in particular, the buffer used to relax the strain from the substrate. This becomes especially significant if lattice mismatched layers (such as GaSb) are grown on GaAs substrates. The large lattice mismatch between GaAs (lattice constant 0.56 nm [21]) and the quantum well (where the lattice constants are approximately 0.61 nm [21]) necessitates the growth of a smooth buffer layer to relax the strain from the substrate and remove defects associated with the large lattice mismatch. A key parameter that can be affected by the growth parameters is the surface roughness of the grown crystal. As such, we performed atomic force microscopy (AFM) measurements of as-grown GaSb layers, grown on GaAs substrates.

#### 3.2.1 Principles of AFM

AFM is a scanning probe microscopy technique, used to investigate the topography of surfaces to sub-nanometer precision (in an ideal case). In an ideal AFM system, an atomically sharp tip is mounted on a thin cantilever. The cantilever is attached to a piezoelectric actuator, used to move the tip towards or away from the sample surface. A laser is reflected off the cantilever, into a split photo-diode. As the cantilever has a known spring constant, the deflection of the cantilever as measured by the photo-diode can be related to the force applied by the piezoelectric actuator.

This deflection is used in a feedback loop to keep the tip at a constant deflection, or to keep a constant force applied to the tip. This is achieved by adjusting the height of the cantilever above the sample surface, which can then be recorded digitally. Additional piezoelectric motors can also be used to move the sample in relation to the tip, and thereby building an image of the surface topography through multiple raster scans of the surface. A schematic of this AFM process is shown in Fig. 3.1.

This method of AFM, known as contact AFM, has several disadvantages. As the

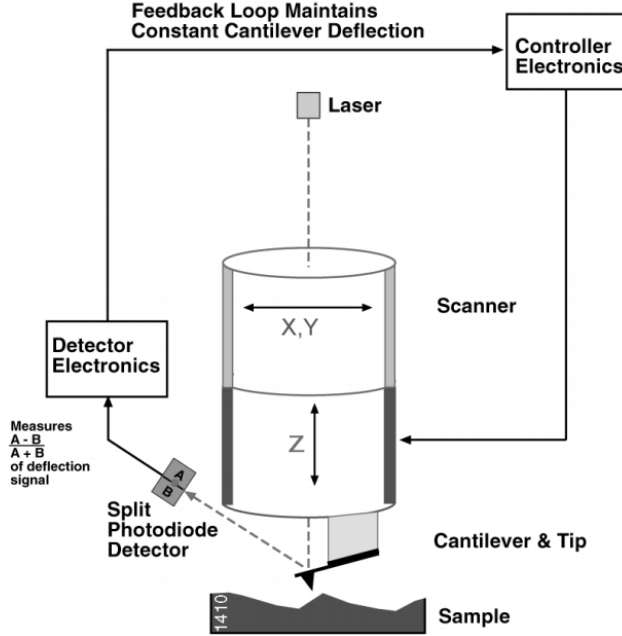


Figure 3.1: Schematic of an AFM in contact mode. The piezoelectric actuator responsible for moving the tip closer or further away from the surface is labelled Z, and the piezoelectric motors responsible for moving the tip horizontally in relation to the sample are labelled X,Y. Taken from [82].

AFM tip is forcefully dragged across the sample surface, the shear forces applied by the tip can cause damage to the sample surface. To mitigate this damage, we use so called “tapping mode” AFM in this thesis.

In “tapping mode” the tip is forced to oscillate by an additional piezoelectric. This oscillation is driven close to the cantilever’s natural resonance frequency  $\omega_0$ . A “tuning” operation is done beforehand, to record the free-space amplitude. As the tip comes into contact with the sample surface, a contact force is experienced, and the amplitude of the tip’s oscillations are damped. The motion of the tip can be described by the following second order differential equation;

$$m\ddot{z} = -kz - \frac{m\omega_0}{Q}\dot{z} + F_{ts} + F_0 \cos(\omega t) \quad (3.1)$$

where  $Q$  and  $k$  are the quality factor and spring constant of the tip/cantilever assembly, respectively.  $F_0$  and  $\omega$  are the amplitude and angular frequency of the driving force,

while  $F_{ts}$  concerns interactions between the tip and the sample surface. This equation describes the motion of a driven, damped harmonic oscillator [83]. The steady-state solution to this differential equation is a sinusoid with an amplitude  $A$ , as shown below;

$$z(z_c, t) = z_0(z_c) + A(z_c) \cos(\omega t - \phi(z_c)) \quad (3.2)$$

where  $z_c$  is the tip-sample separation in the absence of any tip-surface interactions, and  $\phi$  is the phase lag. As the amplitude of the oscillation varies only with the tip-sample separation in our case (i.e attractive tip-sample forces are negligible), we can use a feedback loop to maintain a constant amplitude and thus a constant tip-sample separation. In this way, we can build up a scan of the sample topography while applying much less force to the sample surface than contact mode AFM, at the small sacrifice of scan time [82, 83].

In this work, AFM images were taken with a Veeco Nanoman AFM, using silicon tips, with nominal radius of 8 nm, spring constant of the cantilever of  $42 \text{ Nm}^{-1}$  and resonant frequency of approximately 300 kHz. The upward facing side of the tip was coated in highly reflective aluminium, in order to enhance the photodetector response. AFM images are built up by scanning the tip along the  $x$  direction, and taking a height reading at a set number of points along each scan. The stage then moves in the  $y$  direction, and a set number of scans in the  $x$  direction are then taken. As such, our spacial resolution is directly tied to the size of the scan. Taking a smaller scan with the same number of points will reveal more detail about the surface of the material, but to accurately determine the roughness of the scanned surface we should aim for a larger scan.

#### 3.2.2 AFM as a Measure of Growth Conditions

For successful fabrication of quantum well devices, we require that the surface be as smooth as possible. A smooth top surface facilitates adhesion of contact material, improving device yield [84]. Additionally, smooth interlayer surfaces promote high mobility [22], and so it is of experimental interest to optimise our growth conditions to achieve atomically smooth interfaces.

For this purpose, AFM studies were performed on thick ( $\approx 0.5 \mu\text{m}$ ) layers of GaSb grown under various conditions on GaAs by Dr Lianhe Li. We attempted to optimise the substrate temperature, the III-V ratio and the thickness of an AlSb seed layer used to nucleate the GaSb layer on the GaAs substrate.

### 3.2 AFM Studies of as grown GaSb

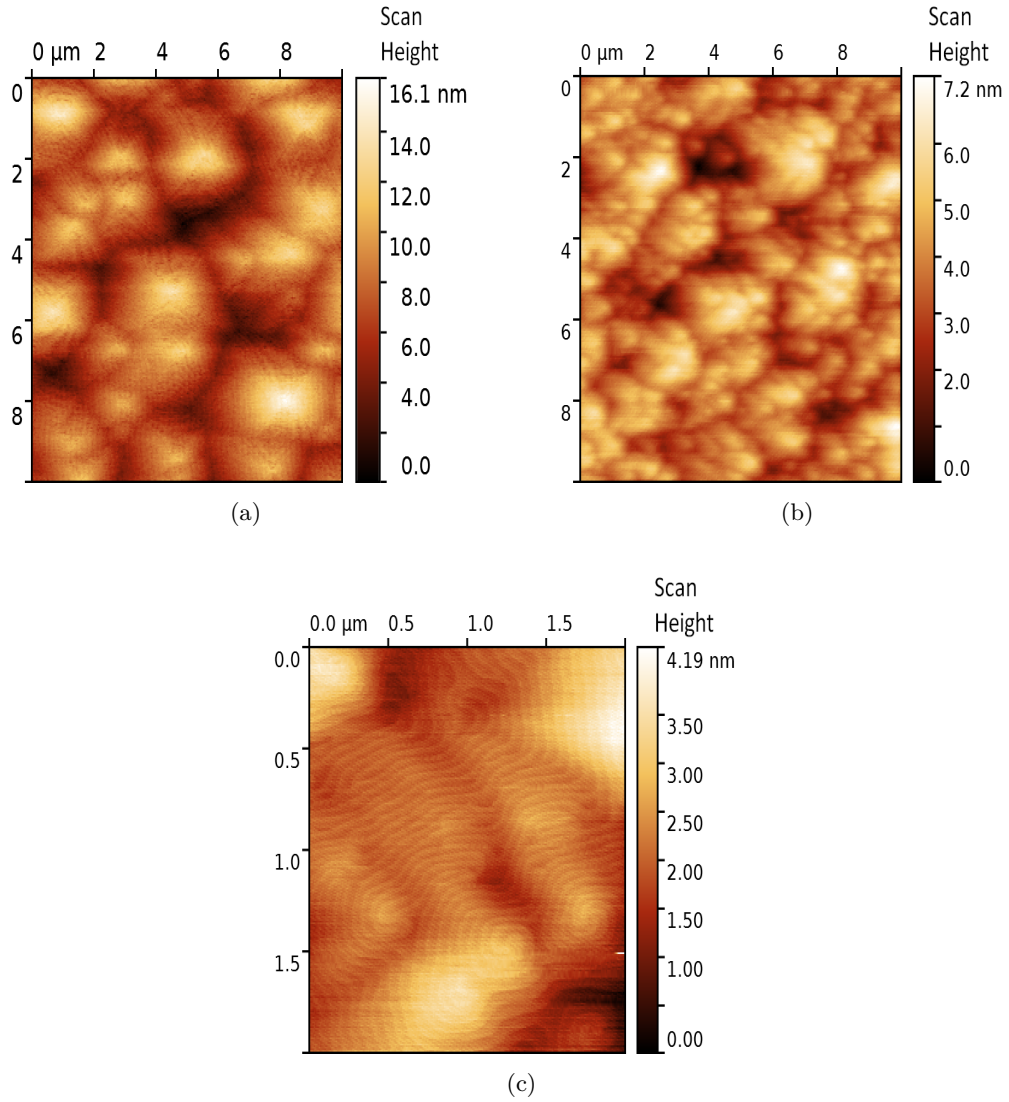


Figure 3.2: AFM images of as grown layers of GaSb on n+ GaAs. Figs. 3.2a and 3.2b shows 10 μm × 10 μm scans used to calculate the average roughness of the material. Fig. 3.2a shows a poorly optimised growth, with a rms roughness of  $2.5 \pm 0.1$  nm, whereas Fig. 3.2b is well optimised, with a rms roughness of  $0.9 \pm 0.1$  nm. Fig. 3.2c shows a 2 μm × 2 μm scan, highlighting the fine structure of the mounds seen in Fig 3.2b.

In the ideal case, we would obtain a wafer that is atomically flat, but this may be beyond the scope of this project. Instead, we measure the rms roughness over a 10  $\mu\text{m}$  scan (with a lateral resolution of 40 nm), and note the number of mounds present on the sample, and their height above the mean. A well optimised sample will contain mounds that are only a few atomic layers above the mean height. An AFM scan of an as grown GaSb layer is shown in Fig. 3.2a, with a comparison to a similar layer, grown under well optimised conditions, is shown in Fig 3.2b. This layer was grown at approximately 510  $^{\circ}\text{C}$ , with a 10 nm thick AlSb buffer layer and a III-V ratio of approximately 4. The rms roughness of this sample is  $0.9 \pm 0.1$  nm, of a similar magnitude to the lattice constant of GaSb [21, 85]. Fig. 3.2c shows a 2  $\mu\text{m}$  square scan (with a resolution of 8 nm) where we can see clear terraces, with a step height of  $0.3 \pm 0.1$  nm, close to the interlayer distance in GaSb [85]. Due to the presence of these monolayer high terraces, we are confident that these wafers are grown in the layer-by-layer growth mode.

## 3.3 Device Fabrication

Once we obtain high quality coupled quantum well wafers from MBE, we need to fabricate suitable devices for cryostat measurement. This section will detail the methods used to fabricate our transport devices (a successful example is shown in Fig. 3.3), and some of the pitfalls to be avoided during the fabrication processes. A detailed “recipe” of the current device process is outlined in appendix A.

### 3.3.1 Photolithography techniques

The devices measured in this thesis were patterned using various photolithography techniques. By shining UV light onto a photo-sensitive polymer, known as a photoresist, the chemical properties of that resist can be changed, altering its solubility in a developer solution. For the photolithography outlined in this work, we use a positive tone photoresist, where the exposed photoresist becomes more soluble in the developer solution. This leaves windows in the polymer through which metal can be deposited, or exposing areas of the substrate to an etch solution. A schematic diagram of this process is shown in Fig. 3.4.

A common positive-tone photoresist used in lithography is the Shipley 1800 series (of which we used S1813 and S1805), developed for the MICROPOSIT MF-319 family of

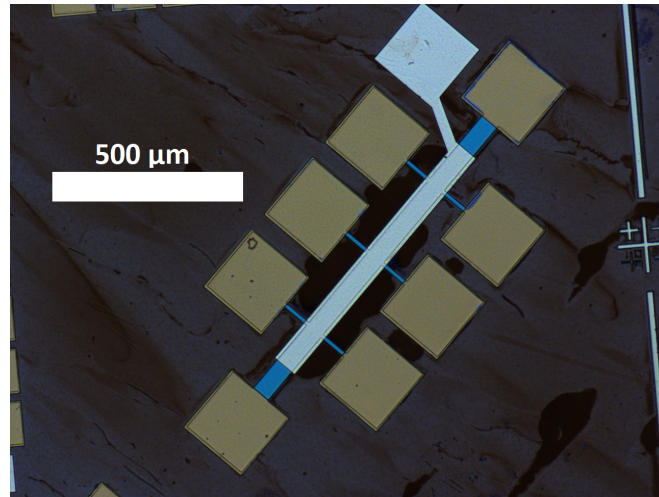


Figure 3.3: Optical micrograph of a successful device on wafer G0186, showing the ohmic contacts (gold), the semiconductor channel (blue), the etched surface (brown) and the top gate electrode (light blue). The  $\text{Al}_2\text{O}_3$  dielectric is transparent, and covers the whole device.

developers. The active component in the MF-319 developer is tetramethyl ammonium hydroxide, which attacks the antimony containing compounds within the quantum well. This has been used to define mesas or contact areas within this class of quantum well [16]. However, we found that as a development time greater than 3 minutes in MF-319 would only produce a roughened surface and no significant etching. As such, we did not pursue this technique. This roughened surface is illustrated in Fig. 3.5, where the surface not covered by the blue MA-N 2403 resist (also developed by tetramethyl ammonium hydroxide) is discoloured and brown. To avoid this damage, exposure times

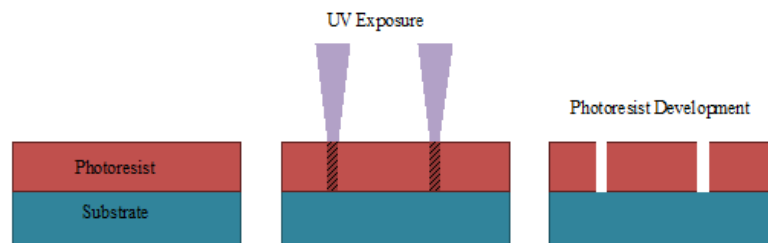


Figure 3.4: Schematic of photolithography process for a positive tone photoresist.

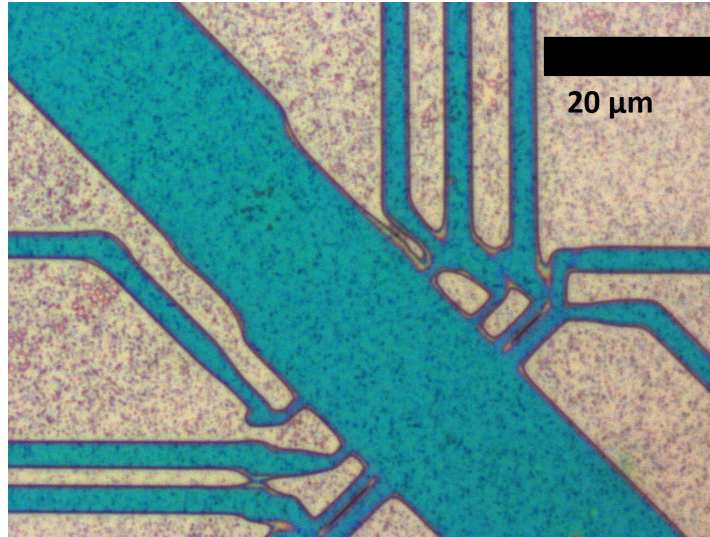


Figure 3.5: Optical micrograph of a wafer SF0801 showing the damage (the brown, roughened surface) caused by 60 s of development in MF-322 (a more concentrated version of MF-319).

were selected in order to minimise the development time, and so minimise exposure of the GaSb capping layer to the tetramethyl ammonium hydroxide.

When depositing metal onto a pattern defined by photolithography, it is helpful to have an “undercut”, where the window in the developed photoresist widens as it approaches the substrate surface. This prevents metal from being deposited on the side of the exposed photoresist, which could hinder lift-off when the photoresist is removed. This undercut can be achieved with a bilayer resist, where the top layer is less sensitive to the UV light. However, here we opted to use a chlorobenzene treatment to the S1813 photoresist. Soaking the photoresist in a chlorobenzene solvent prior to development makes the exposed surface of the photoresist resistant to the developer [86]. As the surface of the photoresist will then be developed at a slower rate to the remaining photoresist, we form the desired undercut profile for our contact step. This process is only relevant for contact metallisation, as undercuts are detrimental when we wish to define a mesa.

### 3.3.2 Ohmic Contact Metallisation by Thermal Evaporation

When making electrical contact to a semiconducting material, it is important that ohmic contacts are used. If this is not the case, the Fermi level can be pinned at the metal-semiconductor interface, inhibiting tuning of the Fermi level by electrostatic gating. Ohmic contacts are defined by a small Schottky barrier, and so are non-rectifying (i.e. carriers can pass across the metal-semiconductor junction in both directions freely) and so the contacts follow Ohm's law, where the voltage drop is directly proportional to the current supplied. This is a substantial material challenge, as any contact material would have to not only form an ohmic contact to the InAs quantum well, but also to the GaSb quantum well. Annealed AuGeNi ohmic contacts are used in quantum wells of GaAs/AlGaAs, so these were attempted first.

If AuGeNi is supplied as a eutectic, as is the case here, then it must be deposited on to the sample surface by mass, rather than a target thickness, because the constituent elements present within the eutectic have different vapour pressures, and so will be deposited at different rates for a given deposition method. Due to this property of the eutectic, all of the source material must be deposited to ensure the correct composition. As thermal evaporation has a high sample throughput and can easily work with small quantities of source material, we chose to thermally evaporate all metals within this thesis.

Thermal evaporation functions by heating the source metal to its boiling point and directing the resulting vapour to the substrate, analogous to MBE. Similarly to MBE, a high vacuum is desired, as this will not only lower the temperature the source metal needs to be heated to in order to evaporate, but will also remove contaminant gas molecules from the deposition chamber. Collisions between metal vapour atoms and gas molecules will deflect the metal "beam" from the target, resulting in the loss of material. Despite this, the pressure in a thermal evaporation chamber does not need to be as tightly controlled as in an MBE chamber, as material quality is not as critical for metallised contacts. As such, pressures of the order of  $10^{-5}$  to  $10^{-7}$  mbar are acceptable for thermal evaporation, which can be easily attained using turbo-molecular pumping techniques. In the evaporators used here, the source metal was heated by passing a high current through a tungsten foil "boat", and using the resistive heating of that "boat" to evaporate the source metal. This "boat" is formed of a thin sheet of metal with a hemispherical indent in the middle, in which the material to be evaporated is

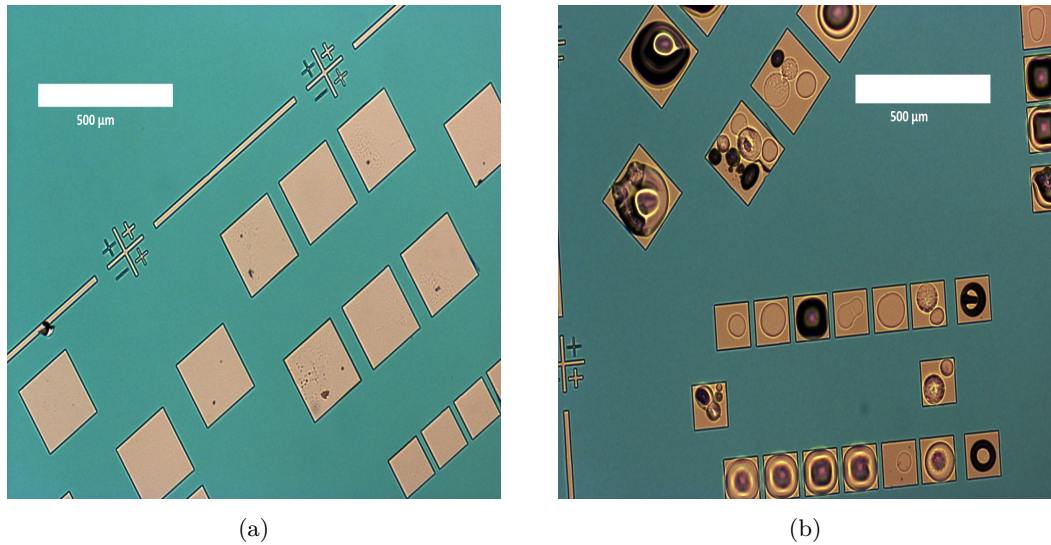


Figure 3.6: Optical micrograph of AuGeNi contacts on wafer SF0799 [3.6a](#) as deposited and [3.6b](#) after 60 s thermal annealing. Note the blackened discolouration of the contact pads, which we attribute to the formation of Ge rich islands [87].

placed. Approximately 0.3 g of AuGeNi eutectic resulted in approximately 100 nm of film being deposited, although this varied from day to day, with a key factor seeming to be the age of the tungsten foil boat. As the indent in the boat directs the material flux, if the boat begins to warp under continuous use, the material flux will drift from the target area, resulting in less material reaching the substrate.

In order for a good ohmic contact to form between GaAs structures and deposited AuGeNi, the AuGeNi must be annealed into the semiconductor surface. This allows the gold to diffuse into the semiconductor, displacing the gallium. The germanium then occupies the gallium vacancies, creating a heavily doped semiconductor to act as an intermediary between the metal and the semiconducting regions [87]. We suspected a similar process would work for the InAs/GaSb coupled quantum wells, and so the contacts were annealed at 300 °C for 60 s in a rapid thermal annealer. This thermal treatment causes germanium-rich islands to form on the contact pads, as illustrated in Fig. [3.6](#).

However, this annealing step causes some damage to the quantum well surface. We suspect that the  $\approx 10^{-2}$  mbar vacuum in the rapid thermal annealing apparatus is

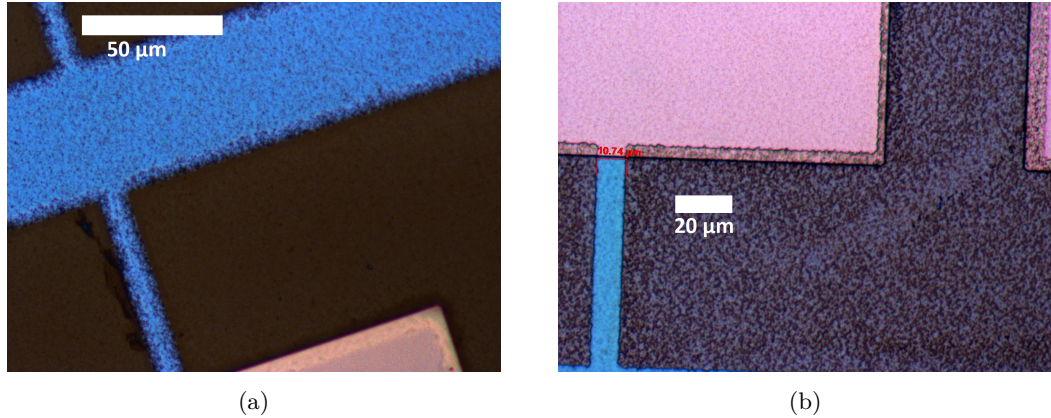


Figure 3.7: Optical micrograph of etched quantum well surface on wafer SF0802 showing a nominally 10  $\mu\text{m}$  Hall bar arm; 3.7a shows where the ohmic contacts were annealed prior etching and 3.7b shows where no annealing has taken place. In both cases, the top of the mesa is shown in blue, the contact material is shown in yellow and the etched surface is shown in brown. Note the roughness of the mesa top in Fig. 3.7a, caused by the annealing process.

not sufficient to prevent oxidation of the quantum well, which leads to an oxide layer forming on the substrate. This oxide layer inhibits further etching steps, as the oxide is attacked by the etching solution more rapidly than the surrounding material. This results in poor photoresist adhesion during the etching process, limiting the size of mesa features we can define.

The etch feature size can be improved by plasma ashing the sample in an oxygen plasma before depositing the photoresist for the etch step, to stabilise the surface oxide. Alternatively, the sample can be etched in 5 minute intervals, to minimise the time the photoresist has to delaminate from the sample surface. However, we found it was far simpler and more effective to remove this explicit annealing step entirely and use the elevated temperatures involved in top gate dielectric deposition to anneal the contacts. The improved etch quality from removing this annealing step, and instead depositing the contact material after chemically etching the quantum well SF0802 is shown in Fig. 3.7. As the reactive nickel remains on the surface of the unannealed AuGeNi ohmic contacts, the etch must be performed first, to prevent anodic effects from disrupting the wet etching process. An annealing step after the mesa etch was not attempted, as

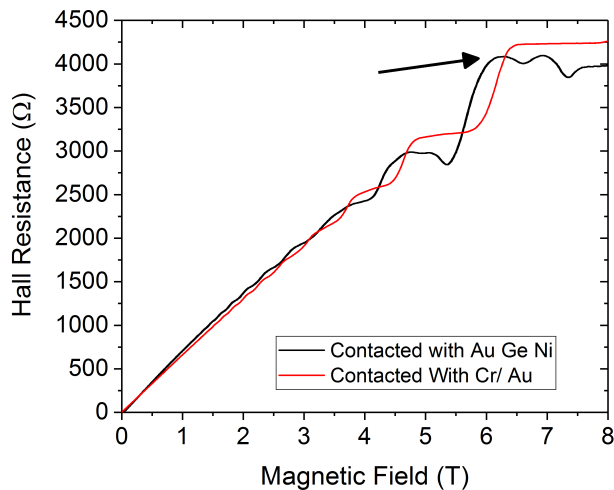


Figure 3.8: Hall resistance up to 8 T at 1.5 K in wafer G0049, where the device has been contacted by AuGeNi (black) and Cr/ Au (red).

we were afraid of oxidising the quantum well channel.

Even when we remove this annealing step, and reduce the interdiffusion of gold into the semiconductor, we still find that there is significant parallel conduction from the layers underneath the quantum well. This is probably caused by the AuGeNi making an undesired contact to these remote layers. This is best illustrated in wafer G0049, a single InAs quantum well, showing features associated with parallel hole conduction in the quantum Hall regime when contacted with AuGeNi, but those features are absent when the wafer is contacted by Cr/Au, as shown in Fig. 3.8. Note that the  $\nu = 6$  plateaux at 7 T (highlighted with an arrow in Fig. 3.8) is well quantised in the case of Cr/Au ohmic contacts, but not in the case of AuGeNi ohmic contacts.

InAs quantum wells have a very low Schottky barrier to other metals and superconductors, which allows them to form good ohmic contacts with many materials [36]. Additionally, several groups have been able to observe hole conduction when the coupled quantum well has been tuned through a hybridisation gap [9, 12, 32] when a Ti/Au ohmic contact has been deposited. As such, we adopt a thermally evaporated Cr/Au system for our ohmic contacts. We choose chromium as the seed layer rather than titanium as titanium forms an alloy with the tungsten in the “boats” used in our thermal

evaporation system [88], which can cause them to fail mid-growth.

The Cr/Au ohmic contacts have several other advantages over AuGeNi eutectic contacts, alongside the lack of undesired contact through a conducting underlayer. Due to the presence of unreactive gold on the surface, so long as the vast majority of the metal is passivated by a photoresist pattern, the etching can proceed unhindered by anodic effects, which is not the case with AuGeNi. Finally, as the components of the Cr/Au system are deposited individually, rather than as a eutectic, we can work to a desired material thickness, rather than depositing material by mass.

#### 3.3.3 Wet Chemical Etching

For semiconductor device fabrication, chemical etching is desired, as it is highly selective (i.e. certain materials will react with a chosen etchant at different rates). However, in this material system, this presents an issue: the majority of the quantum well is composed of the 50 nm thick AlSb barriers, but it is desirable for us to stop our etch in the AlSb lower barrier, to minimise potential undesired contact made to a conducting underlayer. This makes it hard for us to define a “stop layer”, in which the etching will slow to a halt. Therefore, careful optimisation of the process time is crucial.

We decided on a combined etchant, using a 50 % solution by mass of citric acid in water primarily to etch the InAs layer and phosphoric acid component to etch the GaSb. This has been shown to be applicable to InAs/GaSb superlattice photodetectors [89], used in infra-red detectors, and produces better side walls than purely argon-ion beam milling the superlattice.

An interesting property of this “cocktail” etch is that while both etchants dissolve the InAs and GaSb layers of the quantum well relatively quickly [90, 91], the etching of AlSb is comparatively slow. This aids with our timing, as the AlSb quantum well barriers and the insulating  $\text{Al}_{0.8}\text{Ga}_{0.2}\text{Sb}$  buffer layer will retard the etch. but this can lead to strange side-wall features, such as AlSb residues being deposited on the side of the mesa (displayed in Fig. 3.9a), or a strange “overhang” in the etch profile (shown in Fig 3.9b), where the AlSb barriers are undercut by the etching process. It is unknown how these features will play a part in future devices, but for the work presented here, this etching process is sufficient.

As mentioned, the limiting factor on the size of the features we can define with this etching process appears to be resist adhesion. As etching times often exceed 10 minutes,

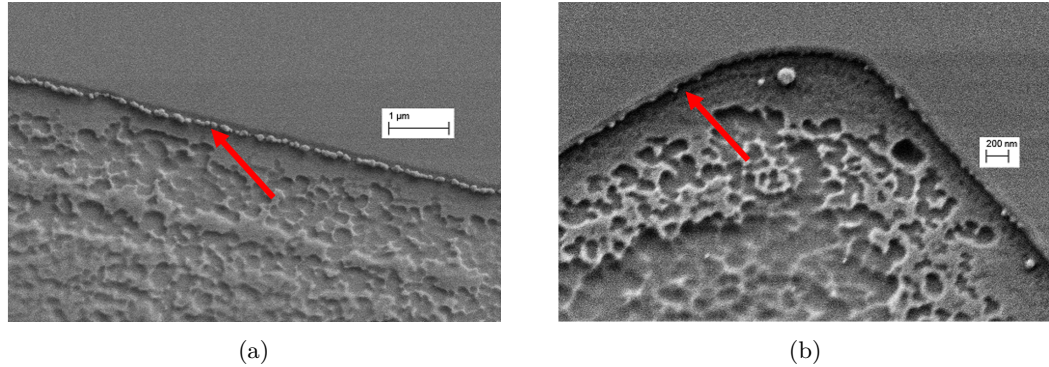


Figure 3.9: SEM micrographs taken at  $30^\circ$  angle of incidence depicting etched sidewalls, etched by using the cocktail etch described here. Fig. 3.9a, taken by Dr Nicolas Peters, shows the residue left on the etched sidewalls, highlighted with an arrow. Fig. 3.9b, taken by Benjamin Steele, shows the etch undercut in an etched sidewall, highlighted with an arrow.

the resist can become delaminated from the substrate, allowing the etch to attack material that would have otherwise been protected. In order to minimise the risk of this occurring, the photoresist is hard-baked prior to etching. By baking the photoresist a second time, the last remnants of the solvent, as well as any residual developer or water left from the development process are evaporated from the photoresist layer. This greatly improves the adhesion of the resist to the wafer surface, improving the available feature size down to  $0.75\ \mu\text{m}$ , when electron-beam lithography techniques are used. It is worth considering that the channel width may be considerably smaller than the measured feature size, due to surface oxidation or etch undercut, and that the  $0.75\ \mu\text{m}$  Hall bar arms were never electronically tested.

However, resist adhesion (and so the available feature size) varies from wafer to wafer. It is possible that a rougher top surface will lead to poorer resist adhesion, limiting our available feature size. We also note that the etch depth after a fixed time (measured with an alpha-step profilometer) varies from wafer to wafer ( $\approx 10\ \text{nm}/\text{min}$  etching rate for some wafers, but half that amount for others). It is unclear why this would be the case, as we would expect the solubility of the material to be consistent, regardless of material quality.

### 3.3.4 Top Gate Fabrication

In order to modulate the carrier concentration within our wafers, we require a process to define a gate on our devices. Successful fabrication of a top gate requires deposition of a dielectric, and metallisation of a gate electrode. We shall first consider the deposition of the gate dielectric.

As a dielectric is inherently insulating, deposition can pose a challenge. Previous studies have used SiN as a dielectric, deposited by plasma-enhanced chemical vapour deposition [32, 92]. However, the high temperatures involved in this process ( $\approx 300$  °C) can cause the AlSb within this class of structures to become conductive [93]. Recent studies have shown that if a single InAs quantum well is exposed to a high temperature then edge conduction through a high resistance channel, not consistent with transport through a single 2DEG, can be detected [94].

Instead, we use atomic layer deposition (ALD) to form our dielectric. ALD is a reactive technique, where two reagent gases are introduced to a chamber and a chemical reaction forms the desired material. Afterwards, unwanted by-products are pumped out of the chamber, ready for another cycle of precursors. In our ALD processes, the two reagents are tetramethylaluminium and water, to form  $\text{Al}_2\text{O}_3$ . As tetramethylaluminium is fairly volatile, and the metal-organic bonds are comparatively weak, the temperatures needed to form the  $\text{Al}_2\text{O}_3$  layer are much lower than those used for other dielectrics in plasma-enhanced chemical vapour deposition, and in fact can be as low as ambient temperature [95, 96].

In an ALD chamber, the reactions are designed to be self-limiting, so that once a precursor containing a metal atom bonds to the surface, no further precursor can bond to that site, eventually forming a monolayer of precursor on the substrate. The second precursor is then introduced, which will then react with the non-metallic half of the precursor, to form the desired material, and freeing reaction sites for the next cycle. The process then builds up the desired dielectric by releasing the two precursors in sequence. A schematic diagram of this process is shown in Fig. 3.10. An advantage of the self-limiting nature of the ALD process is that the dielectric forms a passivation layer over the etched mesa, prolonging the life of the device.

We chose  $\text{Al}_2\text{O}_3$  as our dielectric due to its well characterised ALD deposition, and the fact that it is fragile enough to punch through with a wire-bonder without requiring a via-etch. However, this creates several problems. Firstly, as we can physically punch

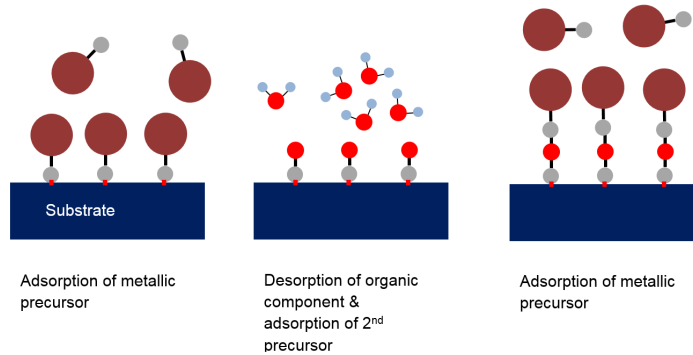


Figure 3.10: Schematic diagram of one and a half ALD cycles, illustrating the formation of an oxide layer with a metallic precursor (in our case, tetramethylaluminium) and water.

through the dielectric during device packaging, the layer underneath the quantum well must be insulating. If a conducting underlayer, such as GaSb, is used [9] then the Cr/Au top-gate pad can make contact to that layer, and short out the top gate. The second problem arises during the photolithography used to define the top gate.  $\text{Al}_2\text{O}_3$  is etched significantly by MF-319 and, due to the positive tone of the S1813 resist used to define a pattern, the area which we wish to define as the top gate will be exposed to the developer and so will be chemically attacked.

To solve this, we use a bilayer PMMA/S1813 resist approach. The theory behind this is that the S1813 can be exposed and developed as normal and that will act as a shadow mask for the PMMA underneath, which is not attacked by the MF-319. The PMMA can then be flood-exposed and developed without attacking the  $\text{Al}_2\text{O}_3$ . A schematic diagram of this lithography process is shown in Fig. 3.11. 495K PMMA-A8 concentration PMMA was chosen for use during this process. In these resist bi-layer processes, the thickness of the deposited metal should not exceed a third of the thickness of the lowest layer, to ensure good lift-off. As PMMA series resists are recommended to be spun at 4000 rpm to achieve a good coating, and the A8 concentration of PMMA spins to 500 nm, this is the ideal resist for depositing a 100 nm thick Cr/Au gate stack via thermal evaporation.

A UVO cleaner was chosen as the deep ultra-violet (DUV) light source to develop the PMMA. As PMMA is designed as a resist for electron beam lithography, a higher

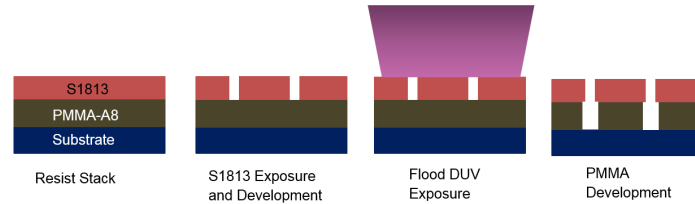


Figure 3.11: Schematic diagram of the S1813-PMMA bilayer resist process used to define the top gate stack.

dose is needed to crosslink the resist layer sufficiently, hence the need for a DUV source. Unfortunately, the UVO cleaner is not the ideal tool, as it is designed to form ozone from ambient oxygen so the DUV produced is strongly absorbed by air. We compensated for this by moving the sample into close proximity with the UV light source within the UVO cleaner, but exposure times remain extremely long (of the order of 30 minutes) for this step. A 7 : 3 solution of isopropyl alcohol and water was chosen as the developer for the PMMA resist. As neither water nor isopropyl alcohol are good solvents of the S1813 resist, this developer solution should not attack the top layer of the resist stack, ensuring a good undercut, aiding in lift off of the Cr/Au top gate stack.

### 3.3.5 Back Gating Processes

In order for us to have full control over the potential landscape in our system, we need both a top and back gate process, to independently modulate the InAs and GaSb quantum wells [16]. We will outline our back-gating process here. It is worth noting that the back gating processes here are all inconsistent. Small variations in either wafer quality or device processing can have knock-on effects to the quality of the back gate. This can lead to situations where one device will have a back gate that is robust up to  $\approx 5$  V at 1.5 K, but another device, from the same fabrication run, will only be robust up to  $\approx 500$  mV.

This variation may arise because in our current device process the Cr/Au ohmic contacts are deposited prior to ALD deposition of the top gate dielectric (at 200 °C). This elevated temperature could result in interdiffusion of metal from the contacts through to the underlayer, which may cause a low-resistance path to develop, leading to less robust gates. Future processes may involve depositing the ohmic contacts after the

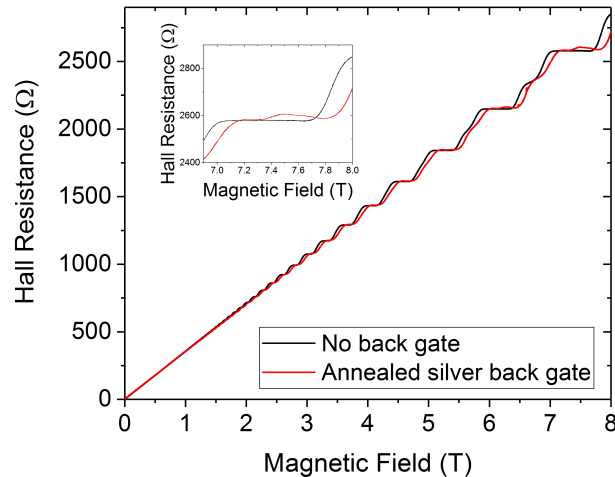


Figure 3.12: Hall resistance up to 8 T on two devices on wafer G0156. The red trace depicts a device with an annealed silver back gate and the black trace has not been annealed during packaging. The inset highlights the odd features in the high field quantum Hall regime, caused by the high resistance contact formed by the silver.

top gate dielectric through a via etch, or lowering the ALD process temperature. This would limit the amount of interdiffusion present within our structures, and hopefully lead to the formation of a more consistent back gating process.

The back gate is formed by making electrical contact to the highly doped substrate. The gate dielectric is then formed of the insulating buffer layers. Two methods were attempted for this purpose. The first was annealing Ag paint into the back of the device in atmosphere during packaging. This was ill advised. While a select few devices produced back gates of exceptional quality, a vast majority of devices did not show sheet resistances consistent with other devices from the same wafer at room temperature. The resistances observed are always lower than that of the pristine devices, consistent with surface oxidation of GaSb into  $\text{Ga}_2\text{O}_3$  and elemental Sb. The Sb layer at the surface can cause parallel conduction through the surface of these structures, altering the transport properties [97]. This is consistent with the behaviour of devices left in atmosphere at ambient temperature, when no  $\text{Al}_2\text{O}_3$  layer is deposited on the surface to passivate the mesa.

Even on devices that show low field transport parameters consistent with other, similar devices, strange features manifest in the high magnetic field quantum Hall regime. We attribute these features to an undesired high resistance contact to the channel. While under normal operation the transport is dominated by the channel, as the Fermi energy enters a gap between the Landau levels, the channel becomes extremely resistive. At this point, the high resistance contact caused by the annealing process (possibly due to oxidation of the exposed material) becomes significant to transport, causing these strange features in the quantum Hall trace even when all gates are grounded, as shown in Fig. 3.12.

Thermally evaporating Cr/Au on the back of the device prior to dielectric deposition is much less harmful to the device than silver paint, but we found that this is only applicable to wafers grown on highly doped GaSb. Cr/Au did not successfully make an ohmic contact to n+ GaAs, and so did not function as a back gate. Contact is made to the metallic back gate through unannealed silver paint, deposited on the chip carrier used to package the device for transport measurements.

---

# CHAPTER 4

---

Cryogenic Measurements

This chapter details the measurement techniques used throughout this thesis. We have already established in chapter 2 that, in order to observe SdH oscillations and the IQHE, we require low temperatures (to mitigate thermal transitions between Landau levels) and high magnetic fields (so that carriers can complete multiple cyclotron orbits without scattering). Therefore we will briefly introduce three cooling mechanisms: pulsed tube cryocoolers; evaporative cooling of  $^4\text{He}$ ; and evaporative cooling of  $^3\text{He}$ . The techniques for measuring the resistances of samples at cryogenic temperatures are also outlined.

### 4.1 Continuous Flow $^4\text{He}$ Cryostat

Most measurements within this thesis were taken on an Oxford instruments continuous-flow  $^4\text{He}$  cryostat, shown schematically in Fig. 4.1. Within this system, the sample space is a vacuum chamber, isolated from the environment by multiple radiation shields. The space between those radiation shields is pumped to a high vacuum. The variable temperature insert (VTI) is then placed in a bath of liquid helium. This helium bath is, in turn, surrounded by a bath of liquid nitrogen to reduce the boil off of liquid helium. The sample is then lowered into this inner vacuum chamber attached to a probe stick, so that the only thermal contact the sample has with the environment comes from the atmosphere within the VTI.

The atmosphere within this inner vacuum chamber can be tightly controlled by admitting some helium into the sample chamber. The sample space is pumped out to a rough vacuum with a rotary pump. This reduced pressure allows He to be drawn from the bath (which is at atmospheric pressure), through a capillary line, and through a section of capillary in thermal contact with a heating element. The flow of helium drawn into the vacuum space can be controlled by a “needle valve”, connected to a stepper motor. This stepper motor can be controlled remotely by a connected PC, allowing consistent flow-rates to be established.

By changing the power supplied to the heating element, the temperature of the incident helium can be changed, and so the temperature of the atmosphere inside the VTI can be tightly controlled. The heating element is within direct thermal contact with a Cernox resistor, which has a well defined and well calibrated temperature dependence. The resistance of this Cernox resistor can be monitored and used to control the temperature of the system in this manner down to 4.2 K. At temperatures higher

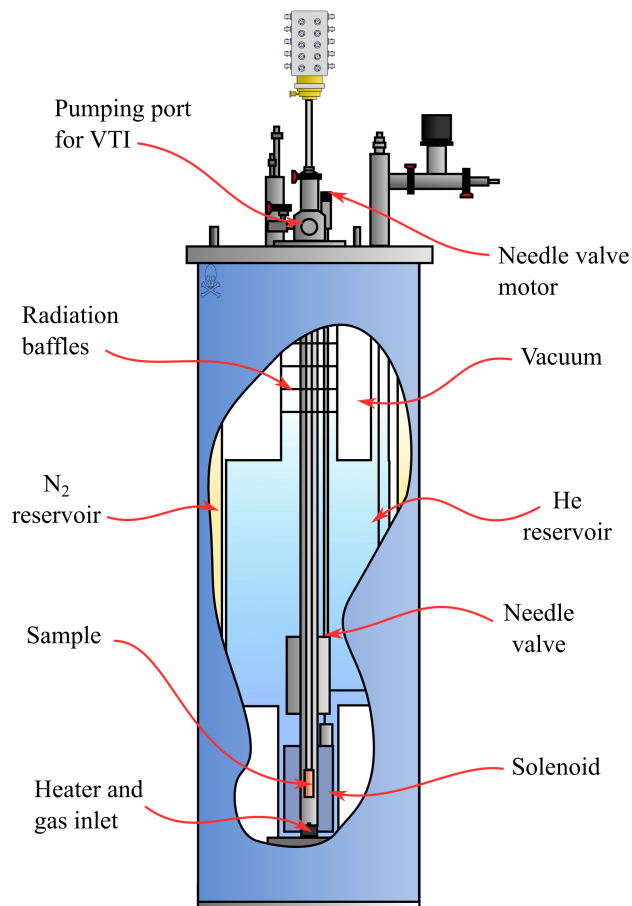


Figure 4.1: Schematic diagram of the continuous flow  $^4\text{He}$  cryostat used in this thesis. From [98]

than this point, a greater flow of gas through the system will lead to increased thermal contact between the suspended sample and the heating element, allowing for faster temperature responses, and greater temperature stability.

As the temperature within the sample space reaches 4.2 K and the helium within the VTI sample space starts to liquefy, an increase in gas in-flow will not increase our cooling power. At this point we use evaporative cooling to remove heat from the system. By pumping on the sample space, we remove gaseous helium from the system and so reduce the vapour pressure of helium within the system. As we decrease the vapour pressure within the system, the boiling point of the liquid helium within the

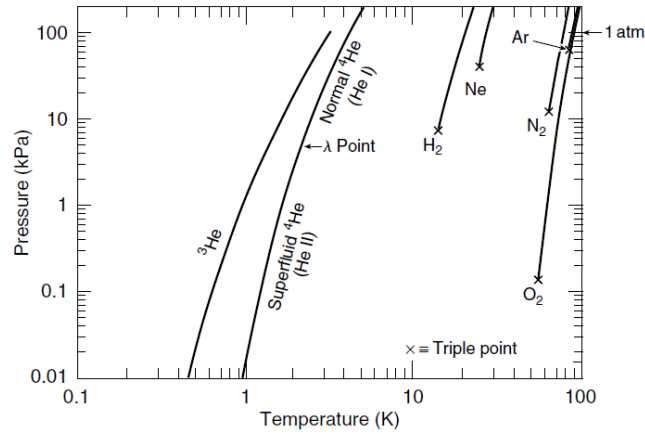


Figure 4.2: Graph of the boiling point of various cryogens as a function of pressure. From [99]

sample space will decrease, the temperature of the liquefied helium will decrease, along with the temperature of the system. However, the vapour pressure varies exponentially with sample temperature. As such, an exponential decrease in pressure is required for an incremental decrease in temperature, as shown in Fig. 4.2 [99].

$^4\text{He}$  also poses an additional problem as a cryogen. As the nucleus is bosonic, it can form a Bose-Einstein condensate that is superfluid below 2.1 K. As a consequence of this, superfluid helium will creep up the sides of the sample space, before it comes into contact with an area of the sample space that is no longer at liquid helium temperatures, where it will evaporate. This puts an additional load on the pump that we use to evacuate the VTI sample space, limiting the pressure we can obtain within the system [100]. In practice, we can obtain 1.3 K within our cryostat, which is reasonable for a rotary pump (which can attain pressures of approximately 0.01 kPa), as in Fig 4.2.

However, even this is impractical to maintain. This assumes that we are only pumping on a fixed volume of liquid cryogen. However, as we evacuate helium from the sample space, we will naturally deplete the amount of liquid helium condensed at the bottom of the cryostat. As such, we leave a small, but finite gas flow through the system, to replenish the condensed liquid helium. In this regime, we wish to minimise the gas in-flow, and so maintain the lowest possible pressure within the sample space. This results in the stable base temperature of our system being 1.5 K, which can be held indefinitely. We can then control the temperature as we did in the high temperature

regime, by applying power to a heating element inside the sample space, and therefore heating the gas inside the cryostat.

## 4.2 Magnetotransport Measurement Techniques

Having established that we can cool our cryostat to 1.5 K, we require a way to measure the resistance of our samples. All of our samples are packaged in square ceramic chip carriers. These chip carriers comprise a recessed, gold plated sample space, surrounded by twenty gold contact pads. The contact pads extend through the entire chip carrier, allowing contact to be made to these pads either by directly soldering the chip carrier to the cryostat wiring or by resting the chip carrier on pins, wired to a “head”, which then connects to the cryostat wiring. The latter is usually preferable as, while it does sacrifice some thermal contact between the sample and cryostat, it allows for easy transfer of samples in and out of the cryostat and minimises the potential damage to the sample during preparation. These sample “heads” are interchangeable and application dependent, in that the orientation the sample makes to the field is fixed by the choice of sample “head”. Each sample “head” contains a separate Cernox resistance thermometer, thermally anchored to the cryostat in exactly the same fashion as the sample. As such, the temperature measured by this sample thermometer is taken as a good measurement of the real temperature of the sample.

The measured sample is stuck down to one of these chip carriers using conductive silver paint. Normally, this silver paint is left to dry in air (at ambient temperature), but if we wish to use this silver paint as a back gate, we then dry the chip carrier in a furnace at 150°C for an hour. Contact is then made from the contact pads on the chip carrier to the ohmic contacts and gate electrodes on the sample by leading a silicon doped aluminium wire from the chip carrier to the device. The aluminium wire is melted onto the desired spot by brief application of an ultrasonic pulse. As the  $\text{Al}_2\text{O}_3$  used as a gate dielectric and passivating layer is so mechanically fragile, the application of this wire and the ultrasonic pulse needed to melt the aluminium punches straight through the dielectric, eliminating the need for a via-etch.

As we are not expecting our samples to have a resistance of over 1 M $\Omega$  [12, 43], we can use a lock-in amplifier (with an internal impedance of 10 M $\Omega$ ) to measure the resistance of our samples. A lock-in amplifier is ideal for cryostat measurements, as not only is it faster than DC techniques, but the applied AC signal averages out thermoelectric

## 4.2 Magnetotransport Measurement Techniques

---

voltages, reducing the impact that multiple solder joints have on the measurement [99]. The principle by which the lock-in amplifier operates is as follows. We supply a pure sine wave AC current with a constant amplitude from a dedicated current source to the sample, and use the waveform from that current source as a reference to the lock-in amplifier. The lock-in amplifier is then connected across the sample as a voltmeter. The signal coming into the lock-in amplifier will be a combination of the resistive response of the sample (oscillating at the reference frequency) and some noise signals (e.g 50 Hz noise from the electrical mains lines inside the building). The phase-sensitive detector within the lock-in amplifier will take that “dirty” input signal and then multiply it by the “clean” reference signal, then average over multiple oscillations. As sine waves of differing frequencies are orthogonal, the output of this phase-sensitive detector will be a DC signal containing the components of the input signal that oscillate at the reference frequency, plus some oscillating noise.

We can eliminate this oscillating noise by placing a low-pass filter in series with the phase-sensitive detector. The time constant of the lock-in amplifier refers to the time constant where the signal coming out of the low-pass filter is attenuated by 3 dB. After this 3 dB point, the low-pass filter will attenuate the signal by an additional 6 dB each time the frequency doubles (known as 6 dB/octave). Up to three additional filters can be added, for up to 24 dB/octave attenuation of noise. The low-pass filters typically restrict the time of the measurement, as a RC filter typically needs five time constants to settle to its final value. Therefore we require a time constant that is long enough to provide a powerful low-pass filter, but short enough that it does not slow our measurements significantly. Therefore, we can eliminate a great deal of noise from our signal as long as we choose our reference frequency to be significantly different to any known noise frequencies or their multiples. Throughout this thesis we choose to apply our reference frequency at 119.77 Hz (far from the line frequency of 50 Hz) and choose a 100 ms time constant for all four of our low-pass filters, (with a total attenuation of 24 dB/octave) so the  $-3$  dB pole is at 1.5 Hz.

Once we have connected lock-in amplifiers so that we can simultaneously measure the longitudinal and transverse resistances (to observe SdH oscillations and IQHE behaviour, respectively), we apply a magnetic field by energising a superconducting solenoid. By passing a current through a solenoid, we create a magnetic field (as Faraday’s law states). We chose not to use a solenoid formed from a conventional metal, such as

copper, as it will dissipate current through its resistance. This dissipation will be seen as resistive heating of the solenoid. At cryogenic temperatures, we cannot afford this extra heat load.

Therefore, the solenoid in our cryostat is constructed from a superconducting  $\text{Nb}_x\text{Ti}_{(1-x)}$  alloy.  $\text{Nb}_{56}\text{Ti}_{44}$  has a critical temperature of 9.2 K, and an upper critical field of  $\approx 9$  T at 4.2 K [101]. This makes  $\text{Nb}_{56}\text{Ti}_{44}$  an ideal material for use in superconducting solenoids, as it will retain its superconducting properties to large magnetic fields when immersed in liquid helium. The solenoid we use in our continuous flow  $^4\text{He}$  cryostat is immersed in the liquid helium bath surrounding the VTI, as in Fig. 4.1, and is therefore kept at 4.2 K. The magnetic fields supplied by this solenoid are therefore limited to 8 T, to avoid areas of the solenoid becoming resistive in a “quench” event. As the inductance of this solenoid is known, by controlling the current we supply to the solenoid, we control the magnetic field across the sample. Data from the lock-in amplifiers, the magnet power supply control and the temperature controllers are then fed into Labview software, programmed by Dr Gavin Burnell, where the data are logged for further analysis.

### 4.3 $^3\text{He}$ Refrigerator

In chapter 5, we require higher magnetic fields than 8 T, and temperatures lower than 1 K. Therefore, we used a  $^3\text{He}$  refrigerator (a so-called Heliox, also provided by Oxford instruments), located in the University of Warwick. As seen in Fig. 4.2,  $^3\text{He}$  naturally has a lower boiling point than  $^4\text{He}$  at a similar pressure. Additionally, the nucleus of  $^3\text{He}$  is a fermion, with a half-integer spin, and so does not form a superfluid condensate at easily accessible temperatures, meaning that evaporative cooling of  $^3\text{He}$  allows us to reach temperatures closer to 300 mK.

However, as  $^3\text{He}$  is not naturally occurring on earth and can only be fabricated by nuclear interactions, it is prohibitively expensive. Therefore, the  $^3\text{He}$  is circulated in a closed system, rather than being pumped out of the cryostat as in the continuous flow  $^4\text{He}$  cryostat. To operate a  $^3\text{He}$  refrigerator, the system must first be cooled to liquefy the  $^3\text{He}$ . This could be accomplished with the evaporative cooling of  $^4\text{He}$ , as described above, but in this case this is achieved with several pulse-tube cryocoolers. These cryocoolers are comprised of three components: a piston; a regenerator with a high thermal conductivity; and a tube with one end in thermal contact with ambient

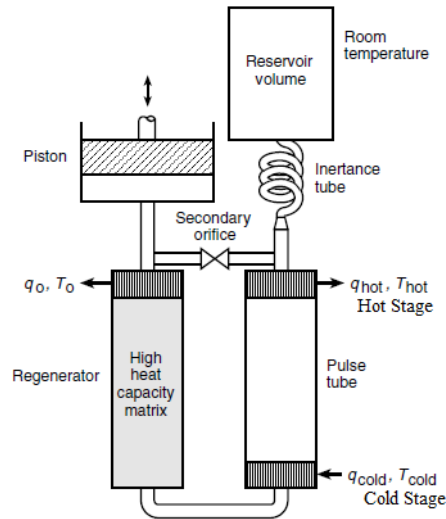


Figure 4.3: Schematic diagram of a typical pulse-tube cryocooler. The entire structure is filled with coolant gas, in our case  $^4\text{He}$ . From [99].

temperature. Crucially, only the regenerator is in thermal contact with the cryostat, so the movement of the piston during a cooling cycle should not introduce vibrations into the cryostat. A schematic diagram of one of these pulse-tube cryocoolers is shown in Fig. 4.3.

The piston will force gas (usually  $^4\text{He}$ ) through the regenerator, into the tube. As the tube is effectively closed, a pressure gradient will form across the tube, with the pressure being at a maximum close to the so called “hot stage”, in contact with ambient temperature. As the “hot stage” will be at ambient temperature, and the pressure there will be maximum, the temperature at the opposite end of the tube, the so-called “cold stage”, must be below ambient temperature, from the ideal gas law. The piston then allows the gas to expand, further lowering the pressure inside the tube, and so further cooling the gas within the tube. A further consequence of this lower pressure is that the cooled gas is drawn through the regenerator. This stage of the cycle is where the useful cooling power is transferred to the system. The cooled gas is then re-compressed by the piston, and the cycle continues. Using these cryocoolers, temperatures of 1.5 K can be achieved [99].

At these temperatures,  $^3\text{He}$  at atmospheric pressure liquefies, as in Fig. 4.2, so we

can start the evaporative cooling of  $^3\text{He}$ . The closed  $^3\text{He}$  system comprises a  $^3\text{He}$  pot, an absorption pump (comprised of activated carbon) and a 1 K plate (where the system is anchored to the cryocoolers). When the system is initially cooled, the absorption pump is in thermal contact with the 1 K plate, and so has absorbed all the  $^3\text{He}$  in the system. The  $^3\text{He}$  pot should be thermally isolated as much as possible from the 1 K plate, and so is typically at a slightly higher temperature at this point. The absorption pump is then locally heated to approximately 15 K, at which point the absorbed  $^3\text{He}$  is out-gassed. The gaseous  $^3\text{He}$  then passes past the 1 K plate, where it liquefies and falls into the  $^3\text{He}$  pot. Due to this influx of cold  $^3\text{He}$  gas, the  $^3\text{He}$  pot is now in thermal contact with the 1 K plate. Once sufficient  $^3\text{He}$  has been condensed, the heat on the absorption pump is released, and the activated carbon inside the pump will start to be cooled by the 1 K plate. As the pump is cooled, it will start to absorb  $^3\text{He}$ , reducing the vapour pressure of  $^3\text{He}$ , and cooling the system down to 300 mK.

The closed nature of the  $^3\text{He}$  system presents several challenges. Firstly, unlike the VTI, the sample cannot be lowered into the  $^3\text{He}$  gas, as the risk of a leak is too great. Therefore, a separate probe stick cannot be used, and instead the sample is directly attached to the cryostat insert, so that the sample is in direct thermal contact to the  $^3\text{He}$  pot. Secondly, and more importantly, there is only a finite amount of  $^3\text{He}$  in the system. As such, this  $^3\text{He}$  refrigerator is a “one-shot” technique. Once the absorption pump has absorbed all the  $^3\text{He}$  in the pot, the cooling power of the pump vanishes, and the temperature of the system will rise. This places a time limit on the measurements that can be attempted with this system.

Due to the finite time in which measurements can be performed in a  $^3\text{He}$  system, controlling the temperature with a heating element located at the sample is counter-productive. If we increase the temperature in this manner, more  $^3\text{He}$  will be boiled off, reducing the amount of time that can be spent at these temperatures. Instead, the temperature of this system is controlled by adjusting the temperature of the absorption pump. The hotter the pump, the less efficiently it will absorb  $^3\text{He}$  gas. This will lead to higher pressures in the  $^3\text{He}$  pot and therefore higher temperatures (up to the temperature of the 1 K plate) within the  $^3\text{He}$  refrigerator.

A slightly different composition of NbTi(Ta) can be used to obtain fields of up to 12 T at 4.2 K [102]. Other than this modified solenoid, the measurement of SdH oscillations and IQHE behaviour is exactly the same as earlier. A sinusoidal current is

applied to the sample with a constant amplitude. The waveform of that current is fed into a lock-in amplifier as a reference, which is then used to measure the resistance of the sample as we change the applied magnetic field.

---

# CHAPTER 5

---

Effects of Limited Coupling on the Transport in  
InAs/(AlSb)/GaSb Quantum Wells

InAs/GaSb coupled quantum wells have been proposed as a candidate 2DTI structure due to the “inverted” band gap, also known as the hybridisation gap, arising from inter-well coupling [5]. However, the conductivity within this hybridisation gap is not zero, due to a finite number of mid-gap states. These mid-gap states can disrupt the topological nature of the transport in this material [12, 43]. Incorporating impurities into these structures, in the form of Si  $\delta$ -dopants at the InAs/GaSb interface [13, 74] or doping the GaSb layer with aluminium [39] have been proposed to localise these mid gap states and enhance the contribution from the topologically protected edge states from residual the bulk conductivity. However, these studies do not take into account the effects that introducing these impurities could have on the inter-well coupling. Therefore, in this chapter we examine the low-temperature magnetotransport effects in an InAs/GaSb coupled quantum well and compare this to a similar system in which the two active layers are separated by an AlSb barrier of intermediate thickness (2.5 nm), simulating a hypothetical scenario where these impurities decouple the two quantum wells, but do not completely eliminate the inter-well coupling [5]. The purpose of this study is to investigate the effect of limited inter-layer tunnelling [25], which is needed to open a hybridisation gap, on the transport properties of the ungated system.

We find that when the InAs and GaSb wells are in intimate contact, the transport through the coupled quantum well structure is analogous to a single InAs 2DEG. However, when the two wells are separated by a thin AlSb barrier, an additional parallel conduction channel is observed. Temperature dependent analysis of the SdH oscillations and the quantum Hall plateaux up to 12 T reveal this parallel conduction channel to be due to uncoupled hole states arising from the GaSb quantum well.

The work discussed in this chapter on the wafer C1295, where the InAs and GaSb quantum wells were separated by a 2.5 nm thick AlSb barrier, was published in Semiconductor Science and Technology [103].

## 5.1 Sample Details

We examine two coupled quantum wells; G0156, which is a coupled quantum well where the two active layers are in intimate contact grown on  $n^+$  GaAs (grown at the University of Leeds by Dr Lianhe Li), and C1295, a coupled quantum well with a 2.5 nm AlSb spacer placed between the active layers, to disrupt the electron hole hybridisation, (grown at the Cavendish laboratory in the University of Cambridge by

## 5.2 Transport in the Case of Intimate Contact

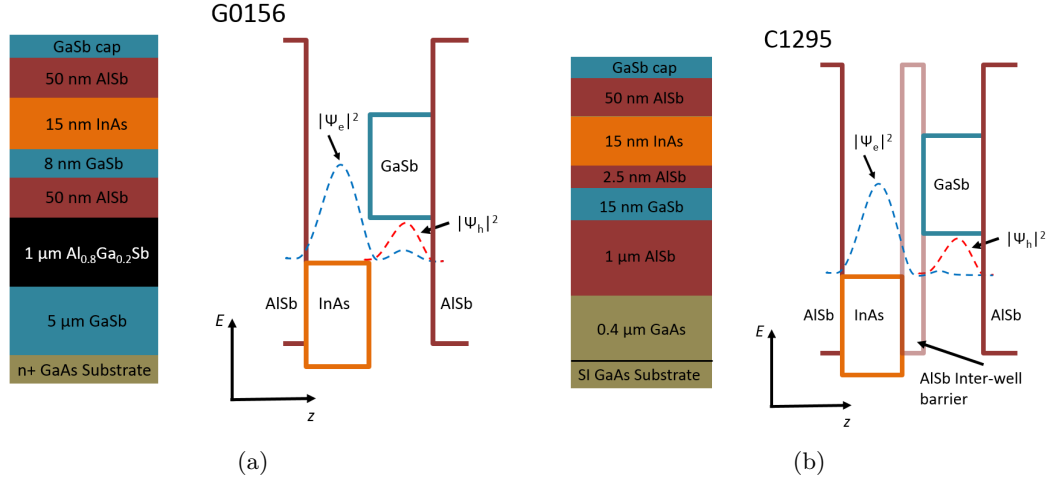


Figure 5.1: Stack structures and band alignments for the two wafers studied in this chapter. The distributions of the electrons (blue dashed lines,  $|\Psi_e|^2$ ) and heavy holes (red dashed lines,  $|\Psi_h|^2$ ) at  $k_{\parallel} = 0$  are also highlighted. Fig. 5.1a shows the stack structure and band alignment for the strongly coupled wafer G0156. Fig. 5.1b shows the stack structure and band alignment for the weakly coupled wafer C1295. Note the significant portion of electron states within the GaSb layer in G0156 [23] that is diminished in C1295, as a result of introducing the inter-layer AlSb barrier.

Professor Edmund Linfield) [44, 61]. This partially decoupled quantum well was grown on semi-insulating GaAs. The layer structure for both of these coupled quantum wells is shown in Fig. 5.1, along with schematic band alignments, detailing how we would expect the inter-well AlSb spacer to change the carrier distribution.

A summary of the electrical transport properties, taken at 2 K via Hall effect measurements, is shown in Table 5.1. Both samples were patterned by wet chemical etching and optical lithography techniques. A point of note is that the contacts on C1295 were formed of an annealed AuGeNi eutectic, whereas the contacts on G0156 were formed of Cr/Au. However, as the lower AlSb barrier in C1295 is 1  $\mu\text{m}$  thick, we disregard any effect of a conducting under-layer in our analysis.

## 5.2 Transport in the Case of Intimate Contact

Wafer	Hall Carrier Density ( $\times 10^{11} \text{ cm}^{-2}$ )	Hall Mobility ( $\text{cm}^2 \text{V}^{-1} \text{s}^{-1}$ )
G0156	$17.5 \pm 0.2$	$111,000 \pm 1000$
C1295	$11.6 \pm 0.1$	$45,000 \pm 500$

Table 5.1: Summary of the low temperature (2 K) transport properties of the wafers studied in this chapter

## 5.2 Transport in the Case of Intimate Contact

Fig. 5.2 shows the magnetoresistance behaviour of the strongly coupled wafer G0156 up to 8 T applied out of plane magnetic field and temperatures up to 10 K. It is apparent that the SdH oscillations arise from a single envelope function above 1 T. Additionally, the minima in the SdH oscillations approach 0  $\Omega$  resistance at the lowest temperatures, as expected for a single 2D carrier gas with minimal parallel conduction.

In equations 2.8 and 2.9, it was shown that the amplitude of the SdH oscillations

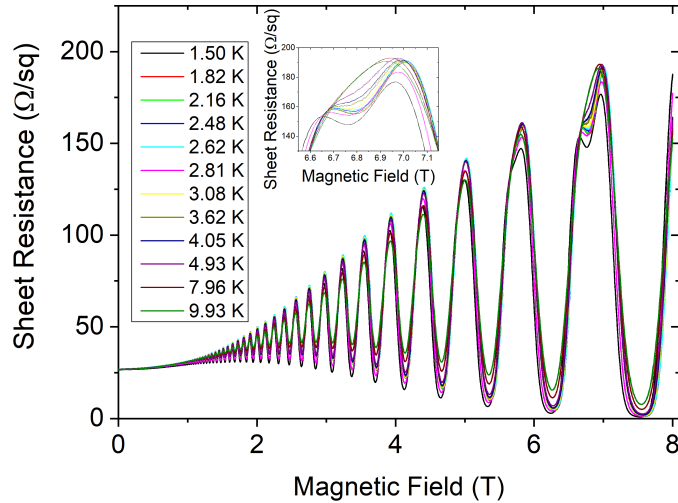


Figure 5.2: Magnetoresistance up to 8 T as a function of temperature up to 10 K for a strongly hybridised wafer, G0156. Inset; the Zeeman split peak at 6.6 T and its temperature dependence.

## 5.2 Transport in the Case of Intimate Contact

---

in a spin-degenerate 2D carrier gas can be modelled as a product of 3 terms, assuming that the Fermi energy is analogous to a single 2DEG ( $E_F = \frac{\pi\hbar^2 n}{m^*}$ ) and that the effective mass is independent of the sample temperature:

$$\frac{\Delta\rho_{xx}(B)}{\rho_{xx}(0)} = 4 \cos\left(\frac{2\pi^2\hbar n}{eB}\right) \exp\left(\frac{-\pi m^* \alpha}{eB\tau_t}\right) \frac{\Psi}{\sinh(\Psi)} \quad (5.1)$$

where;

$$\Psi = \frac{2\pi^2 k_B T m^*}{\hbar e B}. \quad (5.2)$$

Here,  $\tau_t$  is the classical Drude scattering time;  $\alpha = \frac{\tau_t}{\tau_q}$  and is also known as the Dingle ratio,  $\tau_q$  is the single particle momentum relaxation time (also known as the quantum lifetime); and,  $n$  is the carrier density. From the  $\cos\left(\frac{2\pi^2\hbar n}{eB}\right)$  term in equation 5.1, we can see that the frequency of the SdH oscillations in  $B^{-1}$  depends solely on the carrier density responsible for the oscillations. However, the way the oscillations will scale with magnetic field ( $B$ ) and temperature ( $T$ ) will be dependent on both  $\alpha$ , which should be characteristic of the material [104], and  $m^*$ . Since the oscillations in Fig. 5.2 appear to arise from a single envelope function, we infer that the transport in this material arises from a single carrier gas with a single effective mass.

Above 4.5 T, we find that the oscillations at the lowest temperature start to deform, until at 6.6 T the oscillation splits, as show in the inset of Fig. 5.2. We interpret this as the onset of Zeeman splitting, with the spin-degeneracy present in the SdH oscillations being lifted by the strong applied field [60]. As such, the model presented in 5.1 is no longer completely accurate.

We can simplify equation 5.1 by only choosing values of magnetic field that align with the maxima in the oscillations, which reduces the  $\cos\left(\frac{2\pi^2\hbar n}{eB}\right)$  term to a value of unity. To extract all the information from the SdH oscillations and determine the effective mass of the carriers, we need only concern ourselves with the amplitude of the SdH oscillations. As we focus solely on the amplitude of the SdH oscillations, only a single harmonic of the Fourier series presented in equation 2.9 is required (as such  $s = 1$ ). To determine this amplitude ( $\Delta\rho_{xx}(B)$ ) accurately, it is first necessary to subtract a polynomial background from the non-Zeeman split ( $B < 4.5$  T) SdH oscillations. To extract this polynomial background, the maxima and minima of the oscillations are found and plotted. The linear average of these points is then taken, and a polynomial background is then fitted and subtracted. A quadratic background is chosen to simulate the effect of ordinary magnetoresistance of a low mobility parallel

## 5.2 Transport in the Case of Intimate Contact

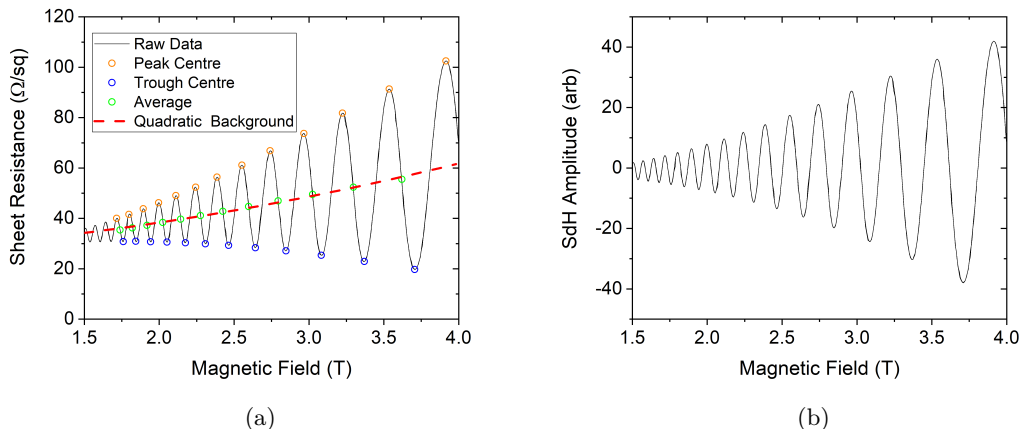


Figure 5.3: Fig. 5.3a: Spin-degenerate SdH oscillations at 1.5 K in G0156 between 1.5 and 4 T, with the peaks highlighted in orange, the troughs highlighted in blue, and the average of these two shown in green. The quadratic fit, used to subtract a baseline is shown in red. Fig. 5.3b: The data in Fig. 5.3a with the extracted background subtracted.

conductor, that may exist within the conductive GaSb buffer structure. This baseline fitting, for the case of 1.5 K is shown in Fig. 5.3.

As we fix our chosen values of magnetic field, equation 5.1 only depends on effective mass, the Dingle ratio, and the temperature of the system. As an ideal 2D system will have a temperature-invariant carrier density and effective mass, by varying the temperature of our sample only the third term in equation 5.1 will change (at a given magnetic field). We can use this dependence to extract the effective mass and Dingle ratio from the evolution of the SdH oscillations as a function of temperature. Therefore, if we assume some value of effective mass, the only unknown will be the Dingle ratio  $\alpha$ , and so a plot of:

$$\ln\left(\frac{\Delta\rho_{xx}(B)}{\rho_{xx}}\frac{\sinh(\Psi)}{\Psi}\right) \quad (5.3)$$

against

$$\frac{1}{\mu B}, \quad (5.4)$$

where  $\mu$  is the Hall mobility, will give a straight line with a gradient of  $-\pi\alpha$  [105]. If a value for  $m^*$  has been assumed that does not approximate the true value of  $m^*$ , the

## 5.2 Transport in the Case of Intimate Contact

---

plot will not be a straight line. To check that our solution is self-consistent, we plot;

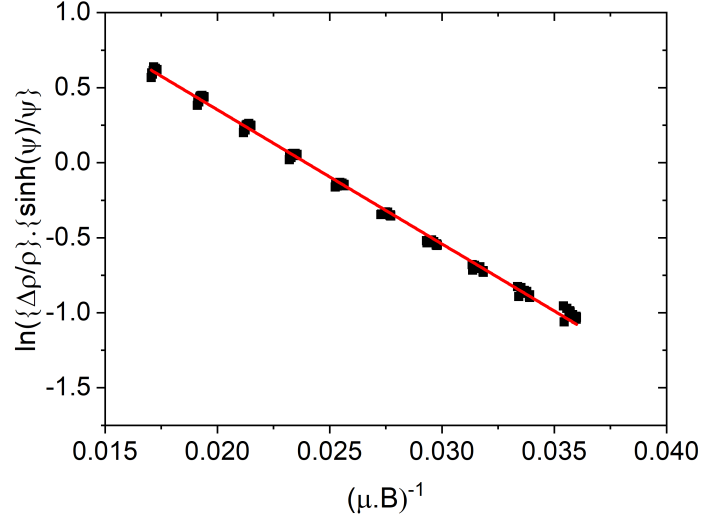
$$\ln\left(\frac{\Delta\rho_{xx}(B)}{\rho_{xx}}\right) \quad (5.5)$$

against

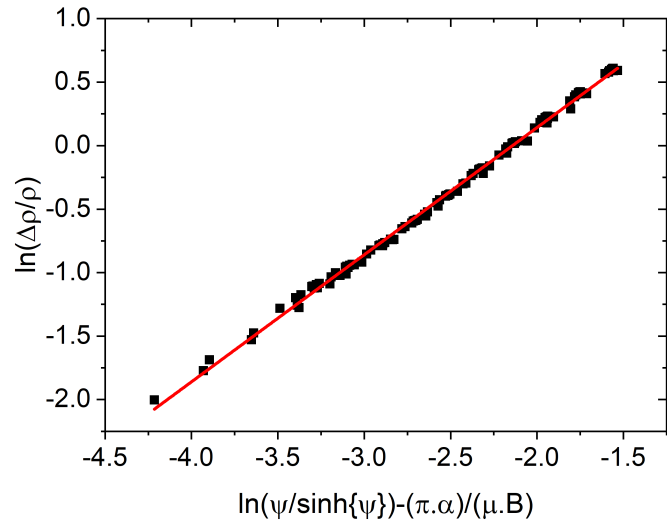
$$\frac{\Psi}{\sinh(\psi)} - \frac{\pi\alpha}{\mu B} \quad (5.6)$$

using the  $\alpha$  gained from the first plot. This plot will have to be a straight line with a gradient of unity. If this is not the case, our solution is incorrect and a new value of  $m^*$  should be assumed.

We repeated this process until self-consistent values of  $m^*$  and  $\alpha$  were obtained. The final iteration of this process, with an iterative step of  $0.005 m_0$ , for the data shown in Fig. 5.2, is given below in Figs 5.4a and 5.4b.



(a)



(b)

Figure 5.4: Plots for self-consistent extraction of Dingle ratio  $\alpha$  and effective mass  $m^*$  in G0156. The linear fit used to extract these quantities is shown in red. These graphs had best fit for the effective mass of  $m^* = (0.040 \pm 0.005) m_0$ , where  $m_0$  is the free electron mass, and Dingle ratio ( $\alpha$ ) =  $28 \pm 3$ .

## 5.2 Transport in the Case of Intimate Contact

---

This value of  $m^* = (0.040 \pm 0.005) m_0$  is close to the accepted literature value of the effective mass for electrons in single InAs quantum wells of  $(0.032 - 0.046) m_0$  [50, 106, 107], and so it is natural for us to assume that our magnetotransport behaviour is dominated by a single electron-like subband at these carrier densities. It is worth noting, however, that more recent studies of InAs quantum wells tend to quote effective masses closer to  $0.032 m_0$  [38, 106]. Our conclusion that transport in this wafer is dominated by a single electron-like subband is further reinforced when we examine the behaviour of the ordinary Hall effect and the IQHE within these samples. Fig. 5.5 shows the behaviour of the Hall resistance over the same temperature range as the data in Fig. 5.2. We find a linear Hall trace at low ( $B < 1$  T) fields, a carrier density that is constant throughout the measured temperature range, and temperature independent quantum Hall plateaux. The ordinary Hall coefficient gives us a carrier density of  $(17.5 \pm 0.2) \times 10^{11} \text{ cm}^{-2}$ , which is consistent with the carrier density derived from the fast Fourier transform of the SdH oscillations, reported as  $(17.8 \pm 0.2) \times 10^{11} \text{ cm}^{-2}$ .

We find that at most values of the applied magnetic field, the IQHE is well quantised to an even integer fraction of the von Klitzing constant ( $\approx 1\%$  deviation from the quantised value). As electrons are doubly spin-degenerate, we expect this even integer quantisation, up until the high magnetic fields, where Zeeman splitting starts to lift the spin-degeneracy. This is best shown at 6.6 T in Fig. 5.5, where a  $\nu = 5$  plateau forms, corresponding with the Zeeman split SdH maxima seen at the same field in Fig. 5.2.

In conclusion, the wafer G0156 shows ungated transport that is comparable to a single InAs 2DEG. The carrier density from both the low field Hall co-efficient and the SdH oscillations are experimentally similar, showing that the most mobile carriers within this material dominate the electronic transport at low fields. Additionally, as the SdH oscillations approach  $0 \Omega$ , there is no bending in the Hall trace as high fields are approached, and the IQHE plateaux are well quantised at integer fractions of the von Klitzing constant. It is clear that at these carrier densities, only a single carrier species is present. Finally, analysis of the envelope function of the SdH oscillations reveals that the effective mass of this material is  $(0.040 \pm 0.005) m_0$ , which is comparable to similar measurements performed on single InAs 2DEGs [50, 106, 107], indicating that the carriers within this material follow a dispersion that closely resembles a single InAs quantum well.

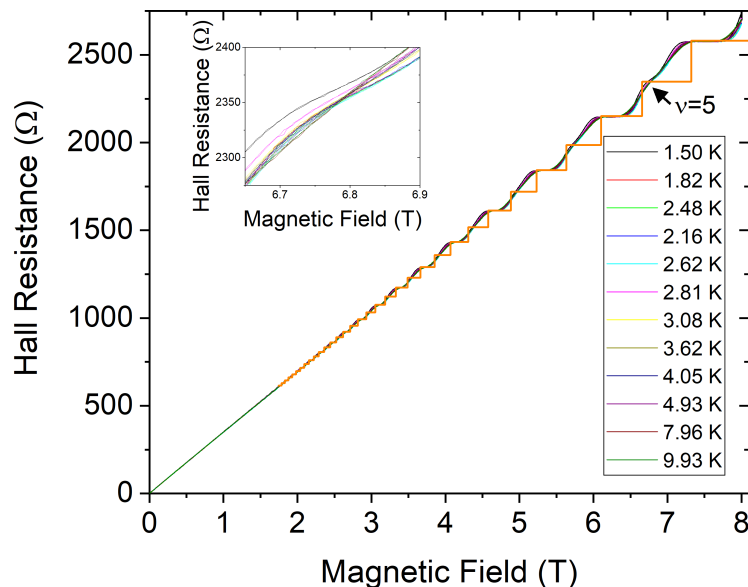


Figure 5.5: Hall resistance up to 8 T as a function of temperature up to 10 K for a strongly hybridised wafer (G0156). The expected positions of the QHE plateaux are shown in orange. The Zeeman split  $\nu = 5$  plateau is highlighted by an arrow. Inset; the highlighted Zeeman split plateau at 6.6 T and its temperature dependence.

### 5.3 Transport in the Case of Disrupted Coupling

In wafer C1295, the two active layers within the quantum well are separated by a 2.5 nm thick AlSb barrier. In this weakly coupled wafer we find that SdH oscillations are observed from 2 T onwards. A fast Fourier transform of this data (to extract the carrier density) reveals that these oscillations, which are periodic in inverse field, are described by single frequency when disregarding Zeeman split peaks [60]. Therefore these oscillations are due to carriers with a density of  $(11.8 \pm 0.1) \times 10^{11} \text{ cm}^{-2}$ , experimentally similar to the Hall carrier density measured with magnetic fields less than 0.2 T applied out of the device plane  $((11.6 \pm 0.1) \times 10^{11} \text{ cm}^{-2}$ , as shown in Table 5.1). These SdH oscillations were observed up to 32.4 K, shown in Fig. 5.6, after which thermal transitions between Landau levels mask the SdH oscillations.

We note that there is a strong background, that is quadratic in field, across all

### 5.3 Transport in the Case of Disrupted Coupling

measured SdH oscillations in Fig. 5.6. As the SdH oscillations no longer approach  $0 \Omega$ , this implies that there is some extra contribution to the transport that is not separated into Landau levels at these fields. This is indicative of some sort of second transport channel, possibly with a lower mobility [37].

The results of the same iterative process described in section 5.2 to find the effective mass and the Dingle ratio, performed by Dr Christopher Morrison, are shown in Fig. 5.7. We note that the Dingle ratio is still relatively high, at  $\alpha = 15 \pm 1$ . This relatively high value of the Dingle ratio suggests that there is a low amount of scattering within the channel from impurities and interfaces and that the dominant contribution is small angle scattering events due to remote impurities [60].

We find that the effective mass of the carriers is  $0.070 \pm 0.005 m_0$ . This is significantly removed from the expected value of effective mass found for single InAs wells ( $(0.032 - 0.046) m_0$ ) of similar carrier densities [50, 106, 107]. Due to this discrepancy, we attribute the majority of transport in this system to be due to hybridised electron-hole states. Additionally, this effective mass aligns extremely well with the

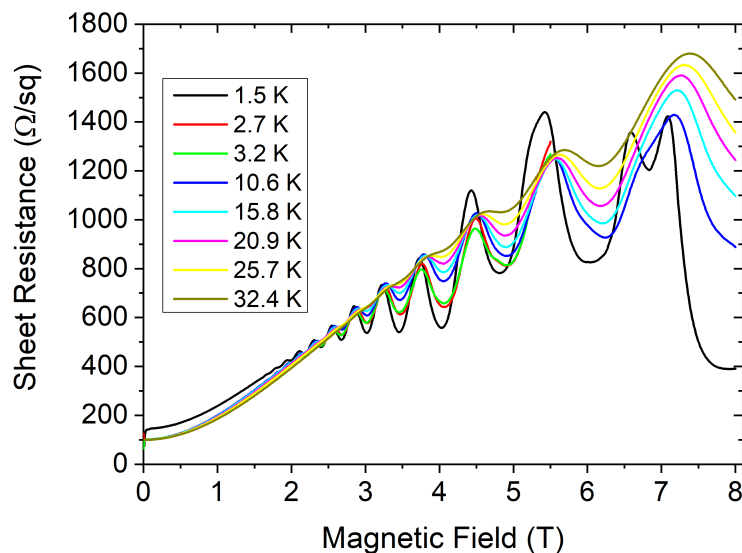


Figure 5.6: Magnetoresistance up to 8 T as a function of temperature up to 10 K for a device on C1295, where the two quantum well layers were separated by a 2.5 nm thick AlSb barrier.

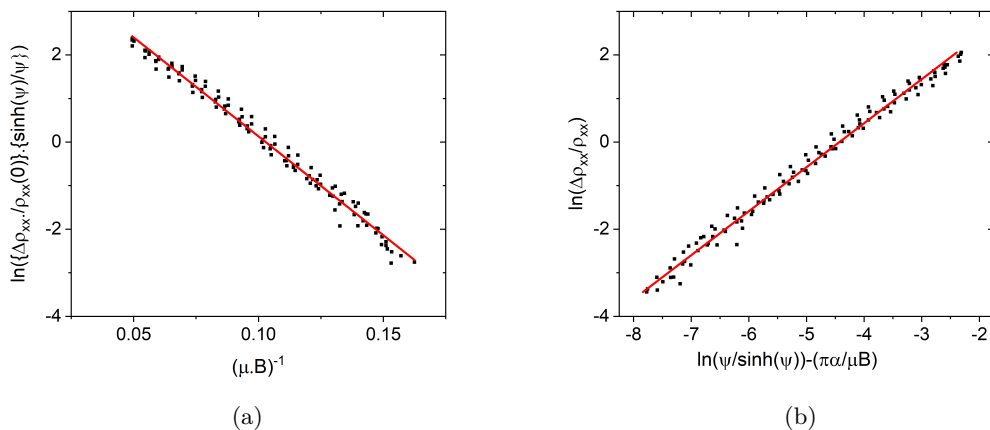


Figure 5.7: Plots for self-consistent extraction of Dingle ratio  $\alpha$  and effective mass  $m^*$  in C1295. The linear fit used to extract these quantities is shown in red. These graphs had best fit values for an effective mass of  $m^* = (0.070 \pm 0.005) m_0$ , where  $m_0$  is the free electron mass, and a Dingle ratio of  $\alpha = 15 \pm 1$

mean of the effective masses of electrons in InAs and holes in GaSb near the band centre ( $\approx 0.071 m_0$ ), which are relevant for transport [106, 108]. This is somewhat counter-intuitive. Why would the partially decoupled system (C1295) show hybridised behaviour, when the strongly coupled system (G0156) shows no such behaviour? We go on to clarify that the reason we observe such behaviour here is due to the AlSb barrier inserted between the InAs and GaSb wells in C1295 limiting the inter-well tunnelling, and therefore closing the hybridisation gap.

Previous studies of hybridised states through cyclotron resonance in a strongly hybridised system [63] and studies of the 2DTI state [74] show that the hybridised nature is largely independent of temperature. This is demonstrated here by the fact that a model using a temperature-independent effective mass describes the data well. In fact, the extracted effective mass and Dingle ratio accurately describes the system up to 32.2 K, after which the SdH oscillations are masked by thermal effects and cannot be accurately analysed.

Additionally, studies of cyclotron resonance in InAs/GaSb heterostructures, where the active layers are in intimate contact (i.e. no inter-well AlSb barrier), have consist-

### 5.3 Transport in the Case of Disrupted Coupling

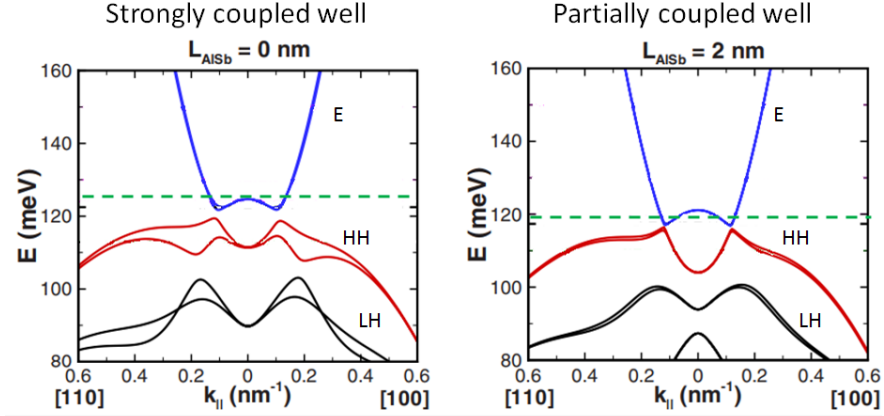


Figure 5.8: In plane dispersion relations for the principal electron (blue, labelled E), heavy hole (red, labelled HH) and light hole (black, labelled LH) bands for two different thicknesses of AlSb spacers ( $L_{\text{AlSb}}$ ). The left figure should be the dispersion of the strongly coupled wafer G0156. The Fermi energy, highlighted by the green dashed line, should result in transport that is analogous to a single 2DEG. The right figure should correspond to the dispersion of the weakly coupled wafer C1295. The Fermi energy (highlighted by the green dashed line) should give rise to SdH oscillations with an effective mass equal to the average between the electron and heavy-hole masses. Adapted from [44].

ently shown that the effective mass is consistent with the single-well case [61, 63, 65, 66]. This has been confirmed by transport measurements of a similar nature to the ones performed here [38], and as such, the effective mass corresponding to the average of electron and hole states in C1295 is interesting.

We understand this effective mass enhancement by first reasoning that the presence of an AlSb spacer, that separates the active InAs and GaSb layers, will limit the penetration of the light hole states from the GaSb into the InAs layer. As these light hole states are needed to establish an anticrossing gap [4, 25], the gap will start to close in energy as we introduce the spacer layer (as shown in Fig. 5.8) [44, 61]. It is worth noting that for intermediate spacer thickness ( $L_{\text{AlSb}} \leq 4$  nm [44]) there is still an element of light hole-electron coupling. This coupling, and the related anticrossing, ensures that the gap at  $k = 0$  will not close, but instead the gap will close at the

### 5.3 Transport in the Case of Disrupted Coupling

---

anticrossing points between the heavy hole subband and the electron subband, which relies on the coupling between the light and heavy holes [25, 28].

However, by limiting this coupling, we reduce the modification the light hole states can make to the conduction band [4]. As such, the curvature of the central maximum in the conduction band behaves more like an unmodified GaSb heavy-hole band [4, 44]. Therefore, if our Fermi energy intersects that central maximum, we will see electron-like states that have dispersion relations that are some combination of electron and heavy hole states, hence the enhanced effective mass, seen experimentally.

In Fig. 5.6, we observe a strong quadratic background to the SdH oscillations, which do not approach  $0 \Omega$  at high fields, indicative of some parallel transport channel. We also see in the insert of Fig. 5.9 that the Hall resistance is non-linear, which suggests the presence of two different carrier species, with different mobilities. In order to understand this, it is helpful to separate the ordinary Hall effect into two regimes, the low field regime, where a carrier is scattered before it can complete a cyclotron orbit, and the high field regime, where cyclotron motion dominates over conventional scattering. Therefore, in the case of co-existing electrons and holes, the Hall coefficient is expressed as [37];

$$R_H = \begin{cases} \frac{p-nb^2}{e(p+nb)^2}, & \text{if; } \omega_c \tau_q \ll 1 \\ \frac{1}{e(p-n)}, & \text{if; } \omega_c \tau_q \gg 1 \end{cases} \quad (5.7)$$

where  $p$  and  $n$  are the hole and electron densities respectively,  $b$  is the ratio of the electron mobility to the hole mobility,  $\omega_c$  is the cyclotron frequency and  $\tau_q$  is the carrier momentum relaxation time. From this we understand that, in the low field region, the Hall coefficient, and so the carrier density calculated from the Hall effect will be weighted based on the mobility of the carriers. However, this will not be the case in the high field regime. In the case where there are two conduction channels, such as co-existing electrons and holes, the Hall coefficient will change as it approaches the high field regime [109]. It is worth noting that in both field regimes there is a positive Hall coefficient in our samples, as shown in Fig. 5.9. This would indicate that electron-like carriers not only play a dominant part in the zero field transport by virtue of their higher mobility, but also are greater in number.

While the non-linearity of the Hall trace is an immediate indicator of parallel conduction, it is important to note that it does not distinguish between carriers that arise from the quantum well channel and carriers that arise from other sources, such as a con-

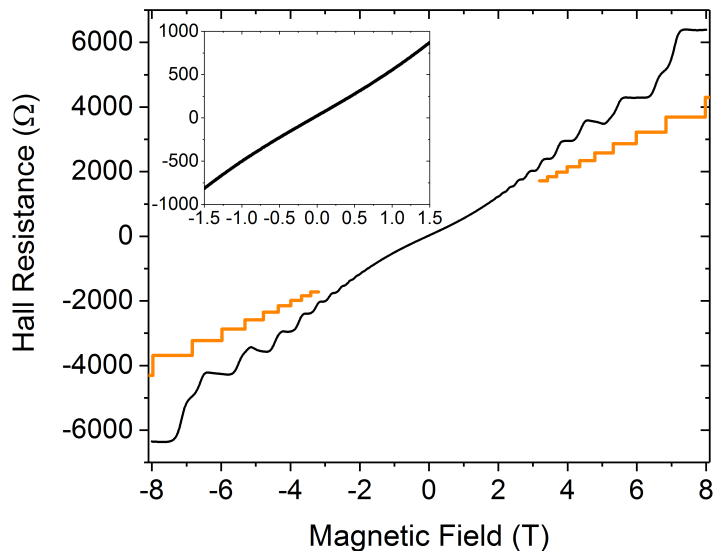


Figure 5.9: Hall resistance up to 8 T for a weakly hybridised wafer, C1295, taken at 1.5 K. The expected positions of the IQHE plateaux, calculated from the ordinary Hall effect ( $B < 0.2$  T), are shown in orange. The insert highlights the non-linearity of the ordinary Hall effect at low magnetic fields ( $|B| \leq 1.5$  T).

ducting buffer layer. To confirm that the carriers arise from the layers confined within the quantum well, it is instructive to look at the positions of the IQHE plateaux.

Fig. 5.9 shows that the bending in the low field Hall trace results in the magnetic field at which these plateaux occur is not consistent with the Hall carrier density or the SdH carrier density. It is also worth noting that at magnetic field values below 5 T, the quantum Hall plateaux do not appear at integer fractions of the von-Klitzing constant. Exact quantisation emerges at 5.5 T at the  $\nu = 6$  plateau. This exact quantisation remains through the  $\nu = 5$  and  $\nu = 4$  at the highest fields.

Exact quantisation of the IQHE would suggest that, at these high fields, there is a negligible density of states near the Fermi energy. However, we can see from Fig. 5.6 that the SdH oscillations at 5.5 T do not approach 0  $\Omega$ , implying that there is still a channel within the quantum well that contributes to transport, rather than some classical channel located within the buffer layers that is pinched off at high magnetic fields. From this, we conclude that there is a second, low mobility, 2D carrier gas

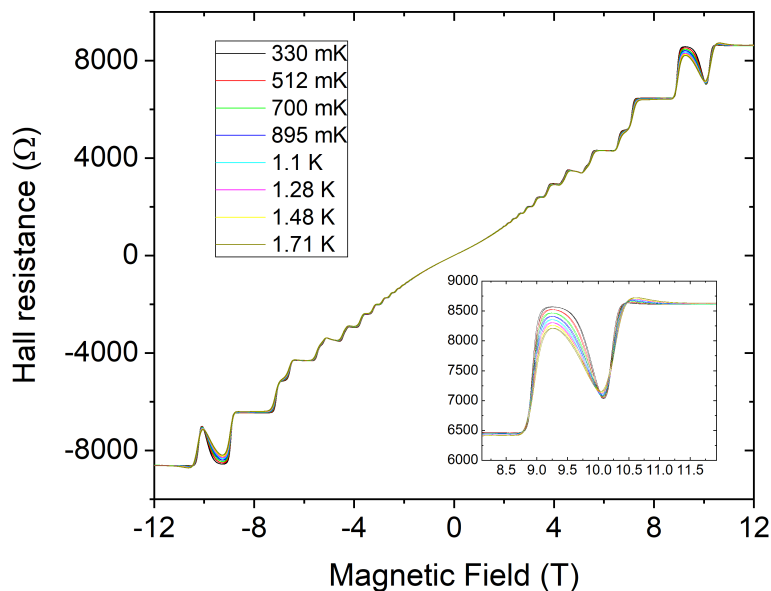


Figure 5.10: Hall resistance up to 12 T for the weakly hybridised wafer, C1295, between 330 mK and 1.71 K. Inset; the anomalous  $\nu \approx 3$  plateau at 9.3 T, and its temperature dependence. Data collected by Dr. Maksym Myronov, analysed by Dr Christopher Morrison.

within the quantum well. This carrier gas is then only quantised into well separated Landau levels at approximately 5.5 T, after which it contributes to the IQHE behaviour normally.

The Hall resistance in the weakly hybridised wafer C1295 was also measured up to an applied magnetic field of 12 T (Fig. 5.10) and down to temperatures of 330 mK, in order to determine the precise origin of this parallel conduction channel. The non-integer quantisation at low magnetic fields persists, even down to 330 mK. Additionally, a  $\nu = 3$  plateau becomes apparent at  $\approx 10$  T. At 9.3 T, and at the lowest measured temperature, we also observe an additional  $\nu \approx 3$  plateau, highlighted in the inset of Fig. 5.10. We can see that only at the lowest measured temperature of 330 mK is this feature well quantised, with lower Hall resistances observed at all other temperatures.

The coexistence of two quantised plateaux at identical filling factors further suggests the presence of two, well confined, states. Additionally, the evolution of the 9.3 T

### 5.3 Transport in the Case of Disrupted Coupling

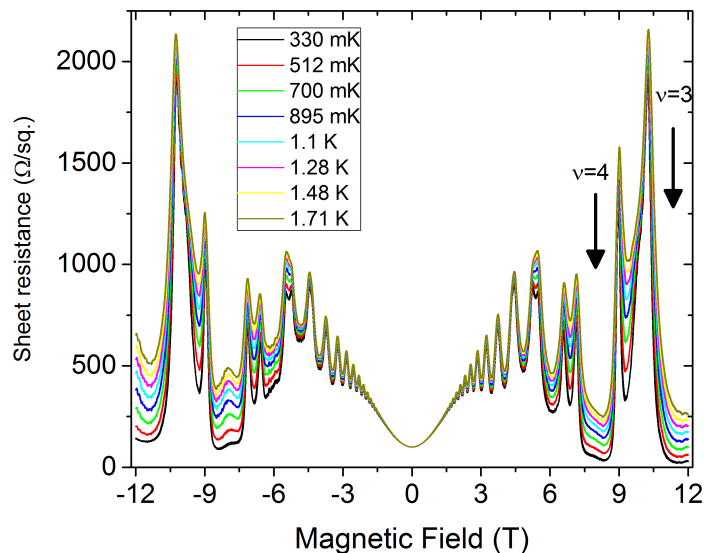


Figure 5.11: Magnetoresistance up to 12 T for a weakly hybridised wafer between 330 mK and 1.71 K. The SdH minima responsible for the conventional  $\nu = 4$  and  $\nu = 3$  IQHE plateaux are highlighted by arrows. Data collected by Dr. Maksym Myronov, analysed by Dr Christopher Morrison.

plateau with temperature suggests that the carriers responsible for this plateau have a much higher effective mass. A larger effective mass would result in a smaller cyclotron frequency  $\omega_c$ , thus making the Landau levels more vulnerable to thermal broadening effects. We go on to show that the carriers responsible for this additional plateau are hole states that are decoupled from the majority channel.

Fig. 5.11 shows the SdH oscillations in wafer C1295 up to 12 T and at temperatures between 330 mK and 1.71 K. The oscillations only approach 0  $\Omega$  resistance at the highest fields and at the lowest temperatures, indicating that it is only under these extreme conditions that the second carrier gas enters the high-field regime, where the carriers can complete multiple cyclotron orbits without scattering.

Of interest is the oscillation that occurs at 9 T, and the accompanying trough at 9.3 T, highlighted in the inset of Fig. 5.10. We note that the plateau at an applied magnetic field of 10.5 T gives us a filling factor  $\nu = 3$ , and the SdH minimum between 7.45 and 8.3 T corresponds to a IQHE plateau at 7.5 T with a filling factor of  $\nu = 4$ .

### 5.3 Transport in the Case of Disrupted Coupling

---

Therefore, we relate the 10.5 T plateau to a Zeeman-split SdH oscillation, and the 7.5 T plateau to a spin-degenerate oscillation.

As such, we associate the 9 T oscillation with this second carrier gas. We note that the temperature dependence of this oscillation is much stronger than any previous or subsequent oscillation, inferring that the effective mass is radically different to the majority carrier gas. This is true if we assume that the nature of the scattering, and as such the Dingle ratio  $\alpha$ , is temperature independent [104]. This assumption appears to be a valid one, since the carrier density and zero field resistance is temperature independent over the measured low temperature range, signifying that the second carrier gas makes a constant contribution to the zero-field transport.

As we fix the Dingle ratio with respect to sample temperature, only the third term in equation 5.1 contains any temperature dependence. Additionally,  $\Psi = \frac{2\pi^2 k_B T m^*}{\hbar e B} \ll 1$  (as we are exclusively considering very high magnetic fields and low temperatures) and thus  $\sinh(\Psi) \approx \Psi$ . Therefore, we can describe the temperature ( $T$ ) dependence of the SdH minimum  $R_{\min}$  at a magnetic field  $B$  with;

$$\ln\left(\frac{R_{\min}}{T}\right) = C - \frac{2\pi^2 k_B m^*}{\hbar e B} T \quad (5.8)$$

where  $C$  is constant with respect to temperature (derived by Dr Christopher Morrison). The temperature dependence and the fit to equation 5.8 are shown in Fig. 5.12.

This fit (red line in Fig. 5.12b) gives a value for the effective mass of these secondary carriers as  $m^* = (0.235 \pm 0.005)m_0$ , which is close to the literature value for the heavy-hole cyclotron mass at high  $k$  in GaSb of  $\approx 0.22m_0$  [21]. This would imply that the holes at  $k = 0$  (with an effective mass of  $\approx 0.11m_0$  [108]) are excluded from transport. The presence of the AlSb spacer of intermediate thickness should not completely close the hybridisation gap at  $k = 0$ , and will first close the hybridisation gap at the anti-crossing points, as there is still an element of light hole-electron coupling [44]. As those low- $k$  states are still forbidden, we see the effective mass of hole states nearer the band-edge. We measure holes, rather than uncoupled electrons, because there are more hole-states near the Fermi level that are outside the hybridisation gapped regime due to the more gradual curvature of the heavy hole valence band when compared to the electron-dominated conduction band, as in Fig. 5.8.

Furthermore, the limited light hole-electron anticrossing caused by the presence of the AlSb spacer will lead to an increasing proportion of the electron and heavy hole Fermi-surfaces being isoenergetic [44, 106]. If the Landau level broadening,  $\Gamma$ , due to

### 5.3 Transport in the Case of Disrupted Coupling

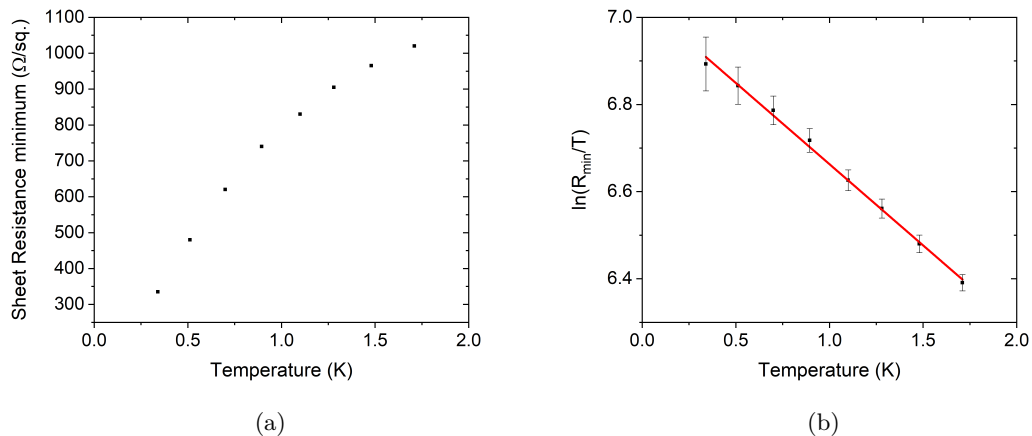


Figure 5.12: Fig. 5.12a, Sheet resistance in C1295 at the 9.3 T minimum plotted as a function of temperature. Fig. 5.12b, the data in Fig. 5.12a plotted as  $\frac{R_{\min}}{T}$  vs  $T$ . The fit to equation 5.8 is shown in red. Data analysed by Dr Christopher Morrison.

scattering becomes much wider than the gap at the anticrossing point, then we can start to see quantum Hall behaviour arising from both carrier types, where the Fermi energy lies in both the electron and hole Landau levels simultaneously [18]. In the case of intimate contact, these states would be separated by the anticrossing gap, and so the system will act as if it is populated by a single carrier gas [9, 12, 38]. Schematic diagrams of these two cases are shown in Fig. 5.13. As the energy level broadening ( $\Gamma = \frac{\hbar}{2\tau_q}$ ) is  $2.74 \pm 0.07$  meV for wafer C1295, we are confident that this is the case, given that strongly hybridised wafers (without an AlSb spacer) show a hybridisation gap of  $\approx 4$  meV [32, 110, 111].

In conclusion, the transport within the partially coupled quantum well structure, C1295, is dominated by hybridised electron-like states, with an effective mass of  $(0.070 \pm 0.005)m_0$ , determined by temperature dependent analysis of the SdH oscillations. This effective mass aligns extremely well with the mean of the effective masses of electrons in InAs and holes in GaSb near the band centre [106, 108], indicating that the Fermi energy crosses a part of the hybridised electron-like bands that have a dispersion relation that is some combination of electron and heavy hole states [4, 44]. Additionally, we observe a parallel conduction channel, hosting uncoupled hole states with an effective mass of

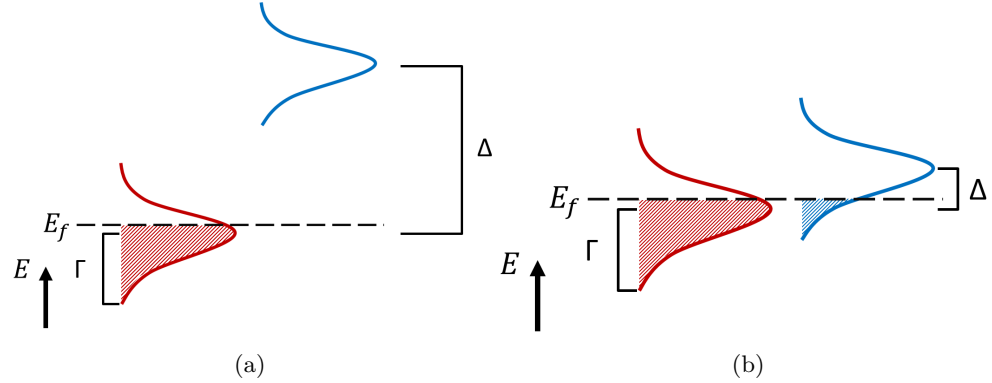


Figure 5.13: Schematic diagrams for the electron (blue) and hole (red) Landau levels illustrating the Fermi energy ( $E_f$ ), the size of the hybridisation gap ( $\Delta$ ) and the level broadening ( $\Gamma$ ). Fig. 5.13a illustrates the case when the layers are in intimate contact, and so the hybridisation gap is much larger than the level broadening. Fig. 5.13b illustrates the effect of an AlSb spacer, reducing the hybridisation gap below the size of the Landau level broadening [18].

$(0.235 \pm 0.005)m_0$ . As this effective mass is similar to the effective mass of heavy-hole states in GaSb at high  $k$  ( $\approx 0.22m_0$  [21]), we conclude that these uncoupled hole states arise from the GaSb layer within the quantum well. The states at low  $k$  contribute to the anticrossing, and so are occupied in this case, but the states near the anticrossing point can bridge the narrow hybridisation gap in this partially coupled system.

## 5.4 Conclusions and Further Work

We have investigated the effective mass and Dingle ratio of carriers in an ungated InAs/GaSb coupled quantum well in intimate contact through analysis of the temperature dependent damping of the SdH oscillations. We also performed similar analysis on a partially de-coupled InAs/AlSb/GaSb quantum well.

We find that for the case of intimate contact, the InAs/GaSb quantum well structure, G0156, produces transport analogous to a single InAs quantum well. An effective mass of  $m^* = (0.040 \pm 0.005) m_0$ , where  $m_0$  is the free electron mass, and a Dingle ratio of  $\alpha = 28 \pm 3$  are determined from temperature-dependent analysis of the SdH oscillations. The quantised Hall plateaux also appear at even integer fractions of the

von-Klitzing constant at magnetic fields consistent with minima in the SdH oscillations. Furthermore, the SdH minima approach 0  $\Omega$  resistance at high magnetic field and low temperature, indicating that there is very little parallel conduction in these structures. These results are consistent with studies of the cyclotron resonance in similar structures [61, 63, 66] as well as studies of the cyclotron resonance of InAs/GaSb superlattices (i.e without the AlSb barriers surrounding the quantum well) [112, 113]. Additionally, similar results have been previously obtained in electrical measurements of InAs/GaSb coupled wells [38, 113].

In contrast, when we insert a AlSb spacer between the active layers of the quantum well, as is the case with wafer C1295, we obtain an effective mass of  $m^* = (0.070 \pm 0.005) m_0$ , where  $m_0$  is the free electron mass, and a Dingle ratio of  $\alpha = 15 \pm 1$ . Additionally, we observe significant bending in the ordinary Hall trace, quantum Hall plateaux that do not occur at integer fractions of the von-Klitzing constant at low fields, and a significant background to the SdH oscillations. All of these are indicative of parallel conduction within the quantum well structure.

It is worth remarking that in both cases, a relatively large value of the Dingle ratio is obtained ( $\alpha \geq 10$ ). This would signify that remote impurities dominate the scattering in both of these structures, rather than defects or impurities within the channel itself [60]. As such, we relate the parallel conduction in C1295 to a de-coupled hole gas lying in the GaSb layer, rather than an impurity layer.

We also find that an anomalous quantum Hall plateau develops at 9.3 T with a filling factor of  $\nu \approx 3$ , alongside another plateau with an identical filling factor at 10.5 T. This anomalous plateau has a temperature dependence that is inconsistent with all the other plateaux, and is accompanied by an additional spin-degenerate SdH oscillation at a magnetic field where other SdH oscillations are Zeeman split.

We fitted the damping of this additional oscillation, under the assumption of temperature independent scattering, and find that this oscillation arises due to carriers with an effective mass of  $m^* = (0.235 \pm 0.005)m_0$ . As such, we assert that the majority of carriers within this weakly coupled system are strongly coupled electron-holes, with a parallel conduction channel carrying uncoupled hole-states, which arise from states outside the hybridisation gap. This is in contrast to the system in intimate contact, where conduction appears to arise from a single carrier gas.

A current limitation of using InAs/GaSb coupled quantum wells for 2DTI devices is

the significant contribution from bulk conduction that exists in many cases [110, 114, 115]. As such, two prevailing methods have been used to suppress bulk conduction from the topological regime, either by adding a layer of Si  $\delta$ -doping to introduce a localisation gap in the bulk (but not topological) dispersion relation [13, 74], or by using a poor quality source of gallium [39] to increase disorder (which the 2DTI phase should be screened against). However, here we have highlighted the need for careful control of these parameters. By explicitly inhibiting the tunnelling between the two layers, the hybridisation gap becomes smaller in energy at the anticrossing point, and a second carrier gas becomes relevant to transport. This second carrier gas could disrupt the 2DTI phase, by allowing the spin filtered edge channels a way to back-scatter that is not topologically protected, and hence must be circumvented in 2DTI devices.

---

# CHAPTER 6

---

Scattering in Coupled Quantum Wells Far from  
Charge Neutrality

---

In this chapter, we consider the effects an inverted band structure, arising from electron-hole coupling, can have the scattering within InAs/GaSb coupled quantum wells away from the charge neutrality point. The motive of this study is to examine the unusual features in the electron mobility found by Nguyen et al. [9] and gain a greater understanding of the transport through the bulk of the quantum well, which could disrupt a potential 2DTI state. We also wish to investigate the behaviour of the electron dominated regime in InAs/GaSb coupled quantum wells in the presence of a gate bias acting on the GaSb layer. It has been noted that, in the regime where the transport is dominated by electrons, application of such a gate bias modulates the carrier density of electron-like states within these coupled quantum wells [9, 38]. To date, this modulation has been attributed to depletion of the GaSb quantum well in the electron dominated regime [12]. If this was the case, we would expect the top and back gates to solely act on the InAs layer. Therefore, should be no region where the top and back gates have a distinct effect on the transport within this electron-dominated regime, but this is not the case in practice.

We investigate the carrier mobility and quantum lifetime in two InAs/GaSb coupled quantum wells within the electron dominated regime at various gate biases. We find that, at the lowest carrier densities, the transport through these coupled wells is analogous to a single 2DEG, where screening from remote impurities determines how the mobility changes with increasing carrier density [53, 116]. However, as the carrier density is increased further, new states near the Fermi energy are detected by an increase in the quantum lifetime [117] and a  $B_{||} = 0$  maximum in the in-plane magnetoresistance [118, 119]. Such features are usually associated with the population of a higher order subband, but as the SdH oscillations appear to be bound by a single envelope function, it appears as if this is not the case here [40].

Finally, when a single subband can be seen in the SdH oscillations, only the total carrier density appears to be important to transport, not the method by which this carrier density is obtained. However, at the highest carrier densities measured here, two electron-like subbands are populated (confirmed by taking the Fourier transform of SdH oscillations at different carrier densities). Within this two-subband regime, and only in this regime, the Hall mobility picks up a dependence on the relative magnitudes of the top and back gate biases, with a more negative back gate bias resulting in a lower Hall mobility for a similar carrier density.

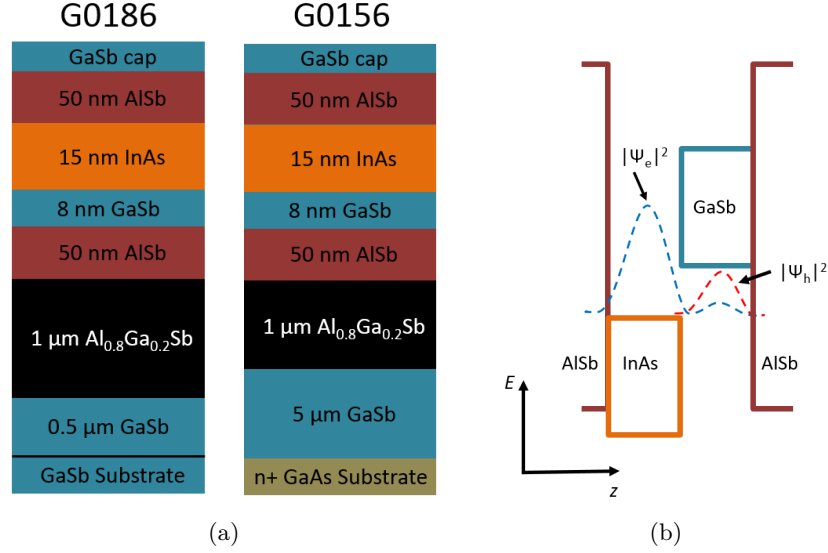


Figure 6.1: Fig. 6.1a shows the stack structures studied within this chapter. Note that in both cases the InAs layer is closer to the top surface and so will be predominately affected by the application of a top gate bias. A schematic band alignment for this structure is shown in Fig. 6.1b, where the distributions of the electrons (blue dashed line,  $|\Psi_e|^2$ ) and heavy holes (red dashed line,  $|\Psi_h|^2$ ) at  $k_{\parallel} = 0$  are also highlighted, following [25]

## 6.1 Sample Details

Two quantum well samples (G0156 and G0186) were patterned into double gated Hall bars, with a separation of 250  $\mu\text{m}$  between the probe arms, by the optical lithography and wet chemical etching techniques outlined in chapter 3. Both of these wafers are composed of a 15 nm InAs layer grown directly on top of a 8 nm GaSb layer. This coupled quantum well structure is then sandwiched between 50 nm thick AlSb barriers, and grown on top of a 1  $\mu\text{m}$  thick  $\text{Al}_{0.8}\text{Ga}_{0.2}\text{Sb}$  buffer layer. G0186 is grown on a highly doped GaSb substrate, with a 0.5  $\mu\text{m}$  thick epitaxial GaSb buffer layer grown to remove any defects. However, G0156 is grown on a lattice mismatched, highly doped, n<sup>+</sup> GaAs substrate, and so a much thicker 4  $\mu\text{m}$  GaSb buffer layer is required to remove the defects associated with the lattice mismatch. The layer structure for both of these coupled quantum wells is shown in Fig. 6.1.

A summary of the as-cooled transport properties for these wafers is shown in Table

Wafer	Carrier Density ( $\times 10^{11} \text{cm}^{-2}$ )	Hall Mobility ( $\text{cm}^2 \text{V}^{-1} \text{s}^{-1}$ )	Effective Mass ( $m_0$ )
G0156	$17.5 \pm 0.2$	$111,000 \pm 1000$	$0.040 \pm 0.005$
G0186	$16.9 \pm 0.2$	$221,000 \pm 2000$	$0.042 \pm 0.005$

Table 6.1: Table of as-cooled transport properties for the two wafers studied in this chapter. The carrier density and Hall mobility are calculated at 1.5 K with  $\pm 0.2$  T applied magnetic field. The effective mass is quoted in units of the free electron rest mass and is calculated from the temperature dependence of the SdH oscillations up to 10 K, as in chapter 5.

6.1. The effective mass was calculated from the temperature dependence of the SdH oscillations [105] up to 10 K with up to 2.5 T magnetic field applied out of the plane of the device and in the absence of any applied gate voltages. The carrier density and Hall mobility were calculated at 1.5 K using up to 0.2 T magnetic field applied out of the device plane, assuming that only 1 electron-like band was relevant to transport. In all cases the measurements were performed using standard lock-in amplifier techniques with a source-drain bias current of  $0.5 \mu\text{A}$ .

The small difference in the as-cooled carrier density is typical for wafers grown by MBE, where slight differences in chamber pressure or sample temperature can drastically alter the surface mobility of adatoms [80]. It is therefore interesting that the Hall mobility differs so much between the two wafers, as the effective mass seems to indicate that both of these wafers show transport analogous to a single InAs 2DEG [50, 106, 107, 120]. We initially attributed this difference in the measured Hall mobilities to the increased number of defects that should exist in the thick GaSb buffer on G0156, which was used to relax the strain between the lattice mismatched substrate and the quantum well.

In order to probe the nature of the scattering within these devices [16], we require both top and back gates. We will initially consider wafer G0186, and then draw comparisons to wafer G0156. Unless otherwise stated, all back gated measurements are performed with a back gate formed of Cr/Au thermally evaporated into the back of the device to minimise the effect of the parallel conduction channel seen in chapter 3, which can occur with an annealed silver paint back gate.

## 6.2 Mobility as a Function of Carrier Density

Measurements of the Hall carrier density and mobility, in G0186, were taken by sweeping the magnetic field between  $\pm 0.2$  T for a range of top and back gate biases, at a fixed temperature of 1.5 K. The results of these measurements, (Fig. 6.2) show that the top and back gates both modulate the Hall carrier density of electron-like carriers as expected. The gates act as if they were modulating a single InAs well, where a negative bias across either gate depletes electrons, whilst a positive bias excites them.

If we model the gates as parallel plate capacitors with a constant dielectric constant of 11 (the average dielectric constant of the stack structure at 300 K [121]) we find that the top gate appears to be  $110 \pm 2$  nm away from the channel at a back gate bias of +2.6 V, and  $112 \pm 2$  nm away from the channel at similar negative back gate bias. This separation is reasonable, as the physical gate-channel separation is of the order of 100 nm, taking into account the 30 nm  $\text{Al}_2\text{O}_3$  dielectric, the 3 nm thick GaSb cap, the 50 nm thick AlSb top barrier and the 15 nm thick InAs channel, and the inaccurate value of  $\epsilon$ , which will be slightly lower at 1.5 K.

This trend for the channel to move further away from the top gate as a more negative back gate bias is applied is somewhat unexpected. If this was a single InAs well, we

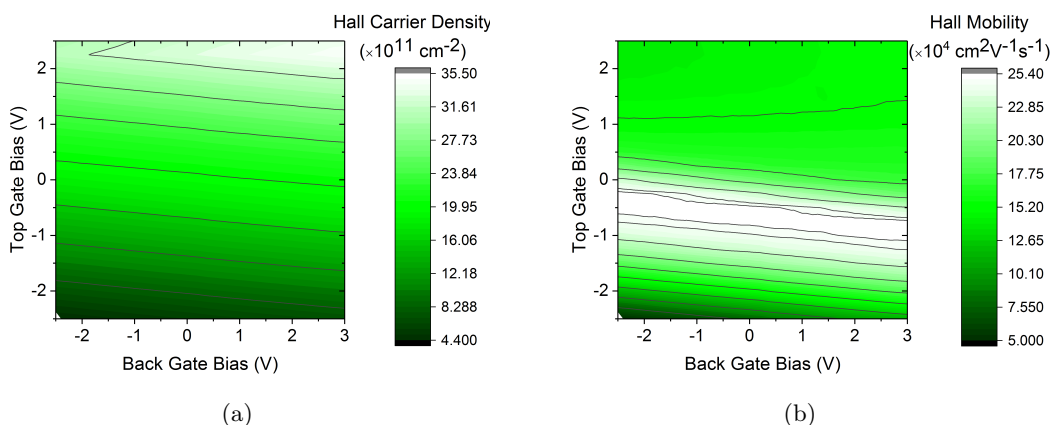


Figure 6.2: Contour maps of the Hall carrier density (in Fig. 6.2a) and the Hall mobility (Fig. 6.2b) as a function of both top and back gate biases in G0186. The black lines indicate contours of constant Hall carrier density and mobility, respectively.

## 6.2 Mobility as a Function of Carrier Density

---

would expect a negative back gate bias to deplete carriers from the bottom of the well, moving the carrier distribution slightly closer to the top gate. However, it is worth noting that this trend is within the error of our measurement. Additionally, no such trend can be seen if we perform similar analysis on the back gate-channel separation, which shows a constant separation of  $1.1 \pm 0.2 \mu\text{m}$ , regardless of the applied top gate bias. Considering this includes the  $1 \mu\text{m}$  thick  $\text{Al}_{0.8}\text{Ga}_{0.2}\text{Sb}$  buffer layer, and the  $0.5 \mu\text{m}$  thick epitaxial GaSb buffer layer, this seems to suggest that the not-intentionally doped GaSb buffer layer remains conducting, even down to 1.5 K.

At low carrier densities, the Hall mobility appears to follow constant contours in the Hall carrier density, no matter the relative top and back gate biases, as shown in Fig. 6.5. This trend continues until the carrier density is increased to a Hall carrier density of  $(20.8 \pm 0.2) \times 10^{11} \text{ cm}^{-2}$ , at which point a more negative back gate bias results in a lower Hall mobility, for a comparable carrier density, highlighted with an arrow in Fig. 6.5. This is confusing, as it implies that at this high carrier density, the top and back gates have different effects on the transport. It is at this carrier density when we start to see SdH oscillations in the high field magnetotransport that are no longer bound by a single envelope function (shown in Fig. 6.3), showing that there is some additional carrier gas contributing to transport at this point.

However, Fig. 6.2a shows that the back gate continues to modulate the carrier density in this regime as before. If the additional carrier gas seen in the SdH oscillations in Fig. 6.3 was due to the occupation of a hole gas within the active GaSb layer, we would expect the low field Hall coefficient,  $R_{\text{H}}$ , to vary as equation 6.1 [37];

$$R_{\text{H}} = \frac{p - nb^2}{e(p + nb)^2} \quad (6.1)$$

where  $n$  and  $p$  are the electron and hole densities, respectively and  $b$  is the ratio between the electron and hole mobilities. Therefore, if this new carrier gas was due to the occupation of a hole subband, we would expect the top gate to have a dominant effect on the Hall mobility and carrier density, as the sign of the Hall coefficient shows that the transport in this material is dominated by electron-like states, which should be localised within the InAs layer. We conclude that this additional carrier gas arises from the second, electron-like subband in the InAs layer, rather than occupation of a hole gas in the GaSb quantum well or buffer layers.

Before we continue to explore the effects of applied gate biases on the mobility within this material, it is necessary to show that the active GaSb layer contributes to

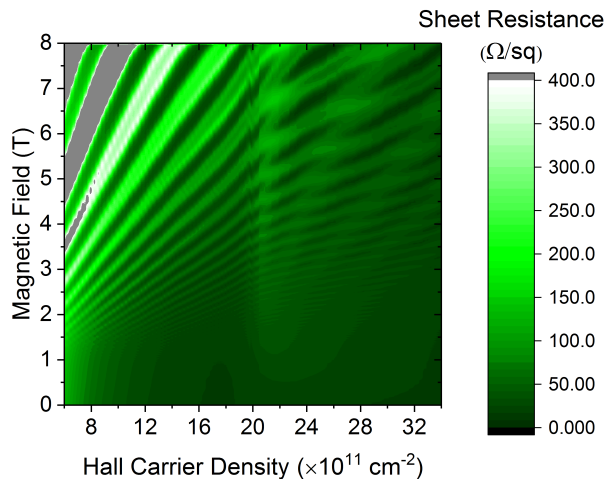


Figure 6.3: SdH oscillations as a function of Hall carrier density, modulated solely by a top gate bias, with the back gate grounded. Note the ring-like structures seen at high carrier densities ( $n \geq 20$ )  $\times 10^{11} \text{ cm}^{-2}$ ), indicative of SdH oscillations arising from a second carrier gas [120].

transport, even if its effects are not immediately visible for the carrier densities studied in Fig. 6.2.

Fig. 6.4a shows the sheet resistance as a function of both top and back gate biases in a device from G0186 at a fixed temperature of 1.5 K. In this case, the back gate was formed from annealing silver paint into the back of the sample, as no Cr/Au back gate was robust up to the required voltage.

We find that the measured sheet resistance generally increases as we apply a more negative back gate bias, as expected, since Fig. 6.2b shows that as we apply a more negative back gate bias, the total carrier density decreases, along with the Hall mobility. However, we see an additional dependence when a top gate bias more negative than  $-2.25 \text{ V}$  is applied. First, at these top gate biases, the back gate has a more pronounced effect on the sheet resistance. Additionally, at highly negative back gate biases, a peak in the sheet resistance emerges. It is worth noting that the back gate bias at which this peak forms becomes less negative for more negative top gate biases, as if we are balancing the carrier concentrations present in the InAs and GaSb quantum wells.

If we fix the top gate bias at  $-3 \text{ V}$  and sweep the back gate through this peak in

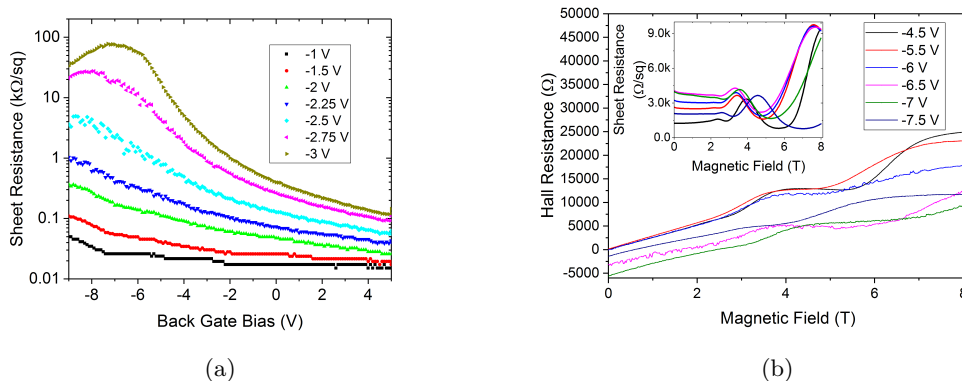


Figure 6.4: Fig. 6.4a shows sheet resistance as a function of applied back gate bias at different applied top gate biases. Fig. 6.4b shows the IQHE behaviour at a constant top gate bias of  $-3$  V at back gate biases of  $-4.5$  V (black),  $-5.5$  V (red),  $-6$  V (blue),  $-6.5$  V (pink),  $-7$  V (green) and  $-7.5$  V (dark blue). The inset shows the SdH oscillations at similar gate biases. In this case, the back gate was formed by annealing silver paint into the back surface of the device

sheet resistance, the origin of this peak becomes somewhat clearer. Before the peak, at a back gate bias of  $-4.5$  V (black curve in Fig. 6.4b), the IQHE behaviour is analogous to a single 2DEG, showing a linear low field Hall coefficient, and a quantum Hall plateau that appears at an integer fraction of the von Klitzing constant. As a more negative back gate bias is applied, the Hall response starts to become non-linear with respect to the applied magnetic field, implying the presence of some new carrier gas contributing to transport. The SdH oscillations (shown in the inset) remain relatively unchanged as we sweep the back gate through this peak region, which also imply that, throughout this region, we are modulating a hole gas, with a low mobility, rather than a high mobility electron gas which would contribute to the SdH oscillations.

Due to the non linearity in the Hall response and the back gate independent SdH oscillations, we equate this peak in sheet resistance to tuning the system into the hybridisation gap [5], close to charge neutrality. This would not occur if the GaSb well was completely depleted and the back gate acted as an additional gate that modulated the InAs layer.

We also note that there is an electron-like carrier density ( $\approx 2 \times 10^{11} \text{ cm}^{-2}$ ) existing

## 6.2 Mobility as a Function of Carrier Density

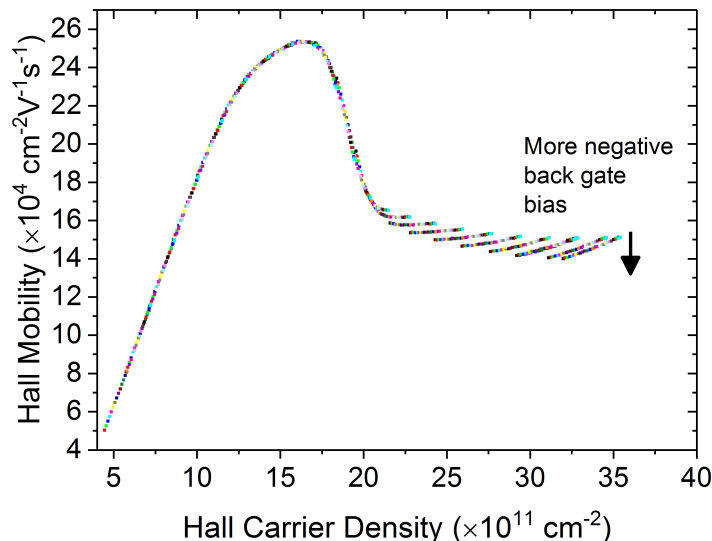


Figure 6.5: Hall mobility as a function of carrier density in G0186. This graph here represents the data in Fig 6.2b plotted as a function of the data in Fig. 6.2a. The different coloured symbols represent different back gate biases between  $\pm 2.5$  V.

at all back gate biases, deduced from the frequency of the SdH oscillations. Additionally, the Hall coefficient is positive at all measured magnetic fields, showing that the majority carriers are electrons throughout this regime [37]. This would infer that there are some mid-gap impurity states, possibly caused by the annealing process needed to form the silver paint back gate in this device, creating a second conduction channel as the system becomes highly resistive, as in chapter 3. If this was not the case, we would expect to observe a transition from an electron-like state to a hole-like state as we pass through a hybridisation gap [32]. Therefore, to probe this hybridised regime further, we would require either a more efficient gating process (to remove these impurity states), or a wafer with a lower 0-bias carrier density (so that less extreme gate biases would be required to reach the hybridisation gap). As we lack these, we will instead focus on the behaviour of the Hall mobility with respect to carrier density, depicted in 6.2.

We re-plot the data in Fig. 6.2b as a function of Hall carrier density in Fig. 6.5. We can see that there is a clear peak in the Hall mobility at a Hall carrier density of  $(15.9 \pm 0.2) \times 10^{11} \text{ cm}^{-2}$ . Additionally, the Hall carrier density alone determines the

mobility, and thus the nature of the scattering, within this heterostructure up until a carrier density of  $(20.8 \pm 0.2) \times 10^{11} \text{ cm}^{-2}$ . At this high carrier density, the mobilities fan out, with a more negative back gate bias resulting in a lower mobility for a similar carrier density.

The trends observed in Fig. 6.5 raise several questions about the effects of applied gate biases on the transport within this system. Why do the relative top and back gate biases only effect the Hall mobility beyond a certain carrier density? What is the significance of the observed peak in Hall mobility? Why does the back gate, acting on the GaSb layer, modulate electron-like carriers at these biases? We attempt to answer these questions by considering the quantum lifetime and transport scattering time (through measurements of the Hall mobility and the envelope function of the SdH oscillations) at a range of gate biases and temperatures, in order to draw conclusions about the effect these gate biases have on the band structure within these coupled quantum wells.

### 6.3 Temperature Scaling of the Mobility

To better understand the behaviour of this InAs/GaSb system as we change the carrier density with an applied gate bias, we first attempt to determine the dominant scattering mechanism through observing the temperature dependence of the mobility. There are two main scattering mechanisms that affect mobility in single 2DEGs: phonon scattering, wherein electrons scatter off periodic perturbations in the lattice potential [122]; and impurity scattering, where some irregularity in the lattice acts as a scattering site. Impurity scattering can be further subdivided into scattering from impurities within the channel, scattering from impurities remote to the channel, and scattering from impurities at the quantum well interfaces [22, 123]. Each of these mechanisms have a well documented temperature dependence [53, 123–125], and so taking measurements of the Hall mobility as a function of sample temperature should reveal the dominant scattering mechanism for a given carrier density. By modulating the carrier density and observing the temperature dependence of the Hall mobility, we can determine whether the dominant scattering mechanism changes across the peak in Hall mobility. The results of this study are shown in Fig. 6.6, where the carrier density was modulated by varying a top gate bias between  $\pm 2.5 \text{ V}$ , in the absence of a back gate bias.

We can see that the peak in Hall mobility at  $(15.9 \pm 0.2) \times 10^{11} \text{ cm}^{-2}$  does not

### 6.3 Temperature Scaling of the Mobility

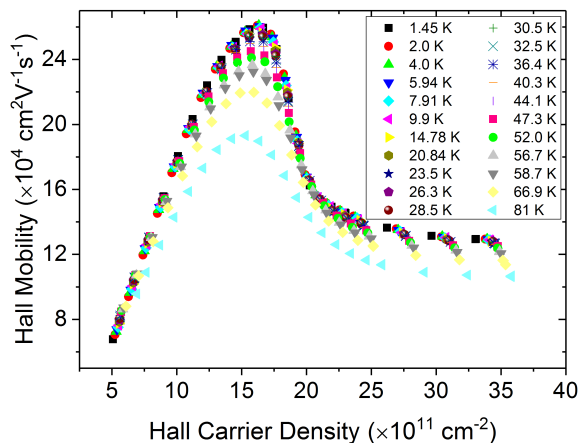


Figure 6.6: Hall mobility as a function of carrier density for different temperatures, up to 81 K. In this case, the carrier density was varied by applying a top gate bias between  $\pm 2.5$  V, in the absence of a back gate bias.

shift in carrier density, even up to the highest measured temperatures. It also becomes apparent that at all carrier densities, the sample temperature does not significantly affect the mobility until  $\approx 40$  K. Each of the scattering mechanisms mentioned here have a different power law dependence on temperature [53, 123–125], and as such, by plotting the log of the Hall mobility against the log of the sample temperature, we can extract the relevant power law dependence with a straight line fit.

Fig. 6.7 shows log-log plots of the Hall mobility against the sample temperature at three relevant carrier densities. In all three cases, there appear to be two temperature regimes, separated by a smooth transition at  $\approx 40$  K. Therefore, two different linear fits are performed in order to understand the nature of the scattering within these low and high temperature regimes. The fit over the low temperature regime ( $T < 20$  K) is shown as a solid red line, whereas the fit over the high temperature regime ( $T > 55$  K) is shown as a dashed blue line in all parts of Fig. 6.7. The gradients extracted from these fits, and thus the related power law exponents, are shown in Table 6.2.

These linear fits are then extrapolated to find the temperature at which the scattering mechanism in the high temperature regime starts to dominate transport. In all cases, this transition occurs at  $53 \pm 3$  K, where the two fits cross. This closely

### 6.3 Temperature Scaling of the Mobility

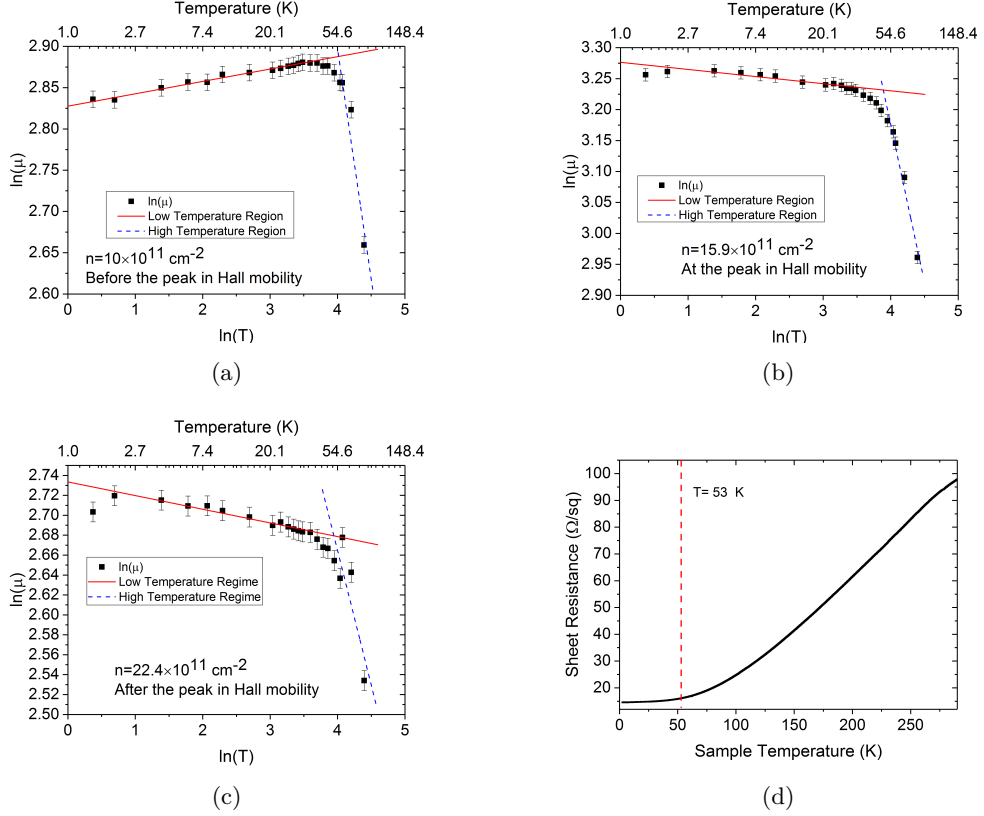


Figure 6.7: Log-log plots of Hall mobility against sample temperature, at a constant carrier density. Fig. 6.7a represents a carrier density of  $(10.0 \pm 0.1) \times 10^{11} \text{ cm}^{-2}$  (well before the peak in Hall mobility), Fig. 6.7b represents a carrier density of  $(15.9 \pm 0.2) \times 10^{11} \text{ cm}^{-2}$  (at the peak in Hall mobility) and Fig. 6.7c represents a carrier density of  $(22.4 \pm 0.2) \times 10^{11} \text{ cm}^{-2}$  (at a carrier density where the relative top and back gate biases is important to the Hall mobility). The solid red lines represent the fit over the low temperature ( $T < 20$  K) regime, whereas the dashed blue lines represent the fit over the high temperature ( $T > 50$  K) regime. For comparison, Fig. 6.7d shows the sheet resistance as a function of temperature on the same sample, with  $T = 53$  K marked by the red, dashed line.

correlates with the temperature at which the resistance reaches a plateau in ungated measurements of the sheet resistance as a function of sample temperature, as shown in Fig. 6.7d, where 53 K is highlighted by a dashed line. This implies that below this

### 6.3 Temperature Scaling of the Mobility

Carrier Density ( $\times 10^{11} \text{cm}^{-2}$ )	Low Temperature Fit	High Temperature Fit
$10.0 \pm 0.1$	$0.015 \pm 0.007$	$-0.6 \pm 0.1$
$15.9 \pm 0.2$	$-0.011 \pm 0.003$	$-0.5 \pm 0.1$
$22.4 \pm 0.2$	$-0.013 \pm 0.008$	$-0.3 \pm 0.1$

Table 6.2: Table of extracted power law exponents from the graphs in Fig. 6.7

temperature phonon-mediated scattering is frozen out [49]. We can see that the high temperature regime for both the low and intermediate carrier densities (Figs. 6.7a and 6.7b, respectively) shows a good fit to a  $\mu \propto T^{-0.5}$  dependence expected from piezoelectrically active acoustic phonons, where  $\mu$  is the Hall mobility [124, 125]. As compound semiconductors, such as InAs, are inherently polar (i.e, indium is positive, whereas arsenic is negative), a deformation in the lattice by a phonon will change the electric field within the structure. Electrons can then scatter from this new potential, causing this thermally activated scattering. It is unclear why the high carrier density regime does not also follow this scaling law, as the presence of two electron-like subbands should not change the piezoelectric potential created by the phonons.

The low temperature regime is more interesting. All three carrier density regimes show mobilities with a very weak temperature dependence, signalling that the dominant scattering mechanism is likely to be scattering from remote or background impurities [53, 104]. Additionally, only the low carrier density region shows a mobility that decreases with decreasing temperature. The other two carrier densities investigated here show similar temperature scaling in the low temperature regime, where the Hall mobility increases as the temperature decreases, as shown in Table 6.2. This sign change would imply that the nature of the scattering processes in this coupled quantum well system fundamentally changes as the carrier density is swept through this mobility peak region. This, combined with the fact that the peak in mobility at  $(15.9 \pm 0.2) \times 10^{11} \text{cm}^{-2}$  Hall carrier density does not appear to shift in carrier density with increasing sample temperature, implies that there is some change in the band structure at this carrier density which changes the possible scattering paths present in the material.

For clarity, we now divide our investigation of the scattering processes into three regimes: a low carrier density regime (Hall carrier density  $< 12 \times 10^{11} \text{cm}^{-2}$ ), where

## 6.4 Scattering in the Low Carrier Density Regime

---

the mobility appears to increase proportionally to the carrier density: the peak regime ( $12 \times 10^{11} \text{ cm}^{-2} \leq \text{Hall carrier density} < 20 \times 10^{11} \text{ cm}^{-2}$ ), detailing the peak and the ensuing drop in Hall mobility: and the high carrier density regime (Hall carrier density  $\geq 20 \times 10^{11} \text{ cm}^{-2}$ ), where two electronic subbands start to be populated and the relative magnitudes of the top and back gate biases have an impact on the total mobility of the system.

### 6.4 Scattering in the Low Carrier Density Regime

The relationship between the mobility and the Hall carrier density when the carrier density is less than  $12 \times 10^{11} \text{ cm}^{-2}$  is perhaps the most analogous to that seen in a single 2DEG. As the electronic carrier density is increased, the screening the carriers provide from impurities also increases, leading to an increase in mobility, usually expressed as  $\mu \propto n^\beta$ , where  $n$  is the Hall carrier density and the exponent  $\beta$  is characteristic of the impurities [120] and the distance between those impurities and the channel [53, 116]. This power law scaling is shown in Fig. 6.8, with the straight line fit used to extract  $\beta = 1.68 \pm 0.05$ . Due to the weak temperature dependence of the mobility within this carrier density regime (as in Table. 6.2), we know that the dominant scattering mechanism is scattering from either impurities removed from the channel or background impurities [53, 104]. As we would expect  $\beta = 0.7$  for background impurities [120], and  $\beta = 1.0$  for an impurity layer close the channel, we attribute this scattering to be from impurities far removed from the transport channel, for which we would expect  $\beta = 1.5$  [116].

It is interesting to note that the data in Fig. 6.8 is collected from a range of top and back gate biases, as the simple scaling of the Hall mobility suggests that only a single carrier gas is present. To precisely ascertain how the back gate affects the carrier density within this coupled quantum well system, we also take the Fourier transform of SdH oscillations as a function of back gate bias at 1.5 K, when the top gate is grounded. The majority of the SdH oscillations should arise from the most mobile carrier within the system, and so the carrier density derived from these oscillations should deviate from the Hall carrier density if a second carrier gas is modulated by action of a back gate. The results of this study are shown in Fig. 6.9a. We can see that, while there is a larger scatter of data associated with calculating the carrier density from the SdH oscillations, both carrier densities show remarkably similar trends as we apply a back gate bias. We

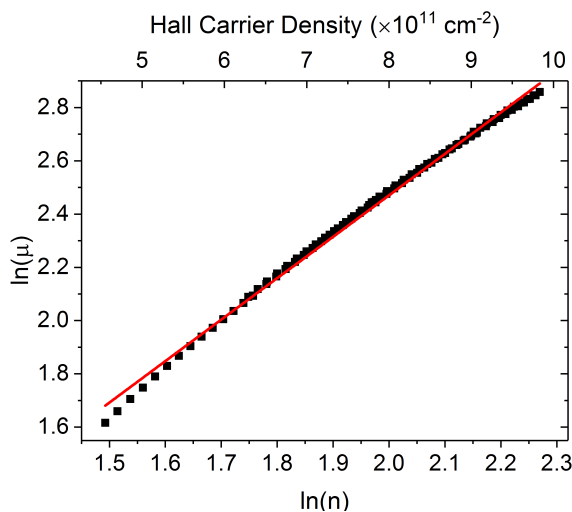


Figure 6.8: The low carrier density region of Fig. 6.5 plotted as a log-log plot of Hall mobility as a function of Hall carrier density. The fit to extract the power law scaling of the mobility is shown in red. As in Fig. 6.5, the back gate is biased between  $\pm 2.5$  V for a range of top gate biases.

note that similar behaviour has been previously noted on coupled quantum wells [9, 38]. Additionally, if the back gate is grounded and the carrier density is modulated solely through the action of a top gate, the same behaviour is observed throughout this low carrier density regime, as shown in Fig. 6.11.

We note that, while the carrier density in Fig. 6.9a is not within the low carrier density regime, identical behaviour is observed when the system is first tuned into the low carrier density regime by a top gate bias and then the carrier density is further modulated by a back gate, as shown in Fig. 6.9b.

Finally, we look at the single particle momentum relaxation time, also known as the quantum lifetime, within this regime [60, 105]. Using the same method outlined in chapter 5, we consider the envelope function of a set of SdH oscillations as a function of temperature. However, it is now possible to apply a gate bias and modulate the carrier density, investigating both the effective mass and Dingle ratio as we do so. We find that the effective mass is constant at  $m^* = 0.035 \pm 0.002 m_0$  (where  $m_0$  is the free electron mass) throughout this region, as shown in Fig. 6.14a. This would seem to indicate that the transport is dominated by a conduction band analogous to that seen

## 6.4 Scattering in the Low Carrier Density Regime

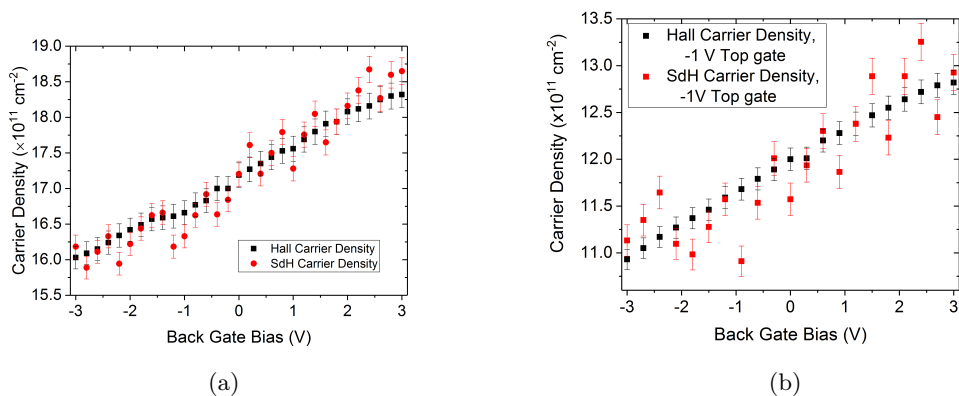


Figure 6.9: Comparison between the low-field ( $B \leq 0.2$  T) Hall carrier density and the carrier density derived from the Fourier transform of the SdH oscillations as a function of back gate bias. The Hall carrier density is shown in black, whereas the SdH carrier density is shown in red. Fig. 6.9a shows the case where the carrier density was modulated solely by applying a back gate bias, with the top gate grounded, whereas Fig. 6.9b shows a similar study where the carrier density was tuned into the low carrier density regime by a  $-1$  V top gate bias.

in InAs quantum wells [50, 106, 107, 120].

Once we have deduced the effective mass,  $m^*$ , we can use the Hall mobility  $\mu$  to determine the transport scattering time  $\tau_t$  through:

$$\tau_t = \frac{m^* \mu}{e} \quad (6.2)$$

which will allow us to determine the quantum lifetime,  $\tau_q$  via the Dingle ratio,  $\alpha = \frac{\tau_t}{\tau_q}$ .

The results of this study, for the low carrier density regime, are shown in Fig. 6.10, where the carrier density was modulated solely through application of a top gate bias. We can see that the quantum lifetime and the transport scattering time increase as we increase the electronic carrier density. This is expected, as the screening against disorder provided by an increase in carrier density should reduce the likelihood of all scattering events [120, 126], not just the large angle events that the transport scattering time is weighted towards.

From the data collected at Hall carrier densities less than  $12 \times 10^{11} \text{ cm}^{-2}$ , it appears as if the InAs/GaSb coupled quantum well contains a single conduction channel

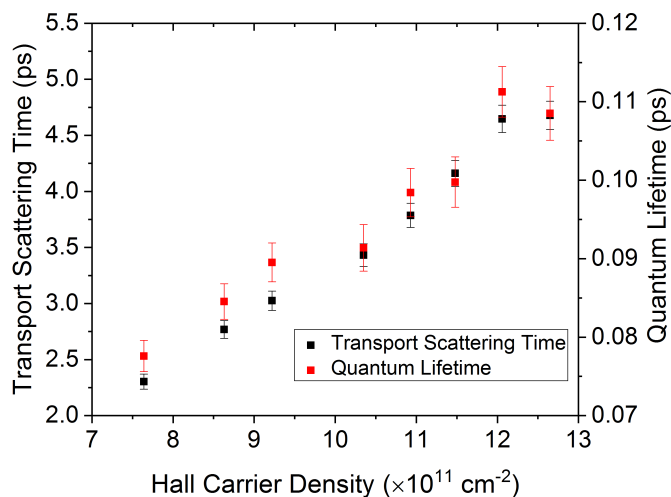


Figure 6.10: Transport scattering time and quantum lifetime as a function of Hall carrier density, in the low density regime. The effective mass and Dingle ratio needed to extract this data was derived from fitting the SdH amplitude as a function of temperature up to 20 K at each top gate bias, with the back gate grounded.

that behaves like an ordinary 2DEG. Increasing the carrier density results in increased screening from remote ionised impurities, as seen in both the Hall mobility (Fig. 6.8) and quantum lifetime (Fig 6.10). Additionally, both the top and back gates have an identical effect on both the electron-like carrier density (as shown in Fig. 6.9) and the Hall mobility, as if the system was a single InAs quantum well.

## 6.5 Scattering in the Peak Regime

In the region where the Hall carrier density is between  $12 \times 10^{11} \text{ cm}^{-2}$  and  $20 \times 10^{11} \text{ cm}^{-2}$ , a peak in Hall mobility is observed, qualitatively similar to those seen in single InAs quantum wells [120], which appears as a second electron subband is populated. If the drop in Hall mobility observed in Fig. 6.5 was due to simple intersubband scattering, we would expect the occupation of the first subband to saturate at the mobility peak [40]. To test this we took Fourier transforms of the SdH oscillations up to 8 T at a constant temperature of 1.5 K, at a range of top gate biases, and compared the carrier density extracted from the Fourier spectrum of the SdH oscillations to the Hall carrier

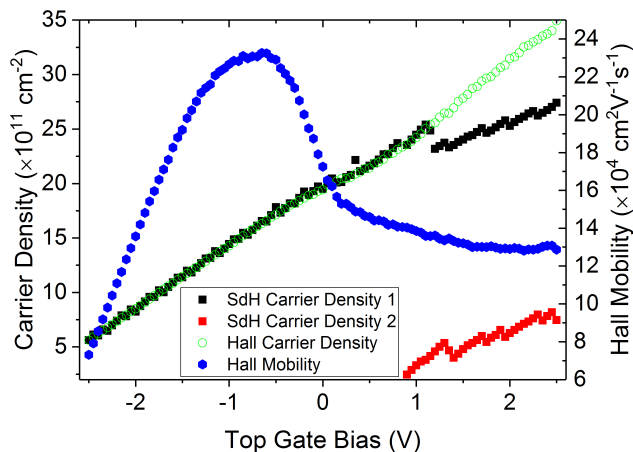


Figure 6.11: Fig. 6.11 shows the carrier density from the Fourier spectrum of the SdH oscillations shown in 6.3 (black and red). The carrier density extracted from the low field ( $B \leq 0.2$  T) Hall coefficient is also shown in green. The Hall mobility (shown in blue) is plotted for comparison.

density. The results of this study are shown in Fig 6.11, with the Hall mobility shown for comparison.

We find that only one peak is seen in the SdH Fourier spectrum for Hall carrier densities below  $(22.7 \pm 0.2) \times 10^{11} \text{ cm}^{-2}$ , and that the carrier density extracted from this Fourier spectrum is experimentally identical to that extracted from the low field ( $B \leq 0.2$  T) Hall coefficient. It is only after this high carrier density that we start seeing a new peak in the Fourier spectrum, shown in Fig 6.11 in red. We note that the carrier density at which we can detect oscillations arising from a second subband ( $(21.7 \pm 0.2) \times 10^{11} \text{ cm}^{-2}$ ) is remarkably similar to the carrier density at which we start to see SdH oscillations no longer bound by a single envelope function, as shown in Fig 6.3.

To confirm this, Fig. 6.12 shows IQHE behaviour and SdH oscillations where the carrier density has been tuned to  $(18.4 \pm 0.2) \times 10^{11} \text{ cm}^{-2}$  by the application of a top gate bias, with the back gate grounded. We can see that the SdH oscillations arise from a single envelope function, and that the quantum Hall plateaux align well with the expected plateaux for even filling factors ( $< 5\%$  deviation from integer fractions of

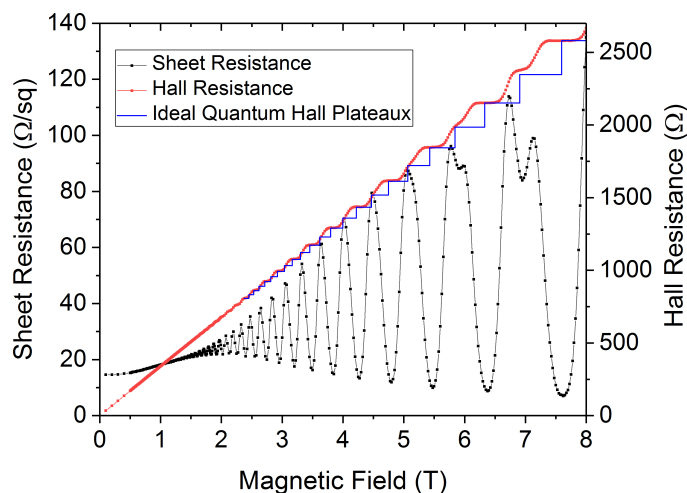


Figure 6.12: SdH oscillations (black) and IQHE plateaux (red) in a device on G0186 at 1.5 K, showing transport consistent with that arising from a single 2DEG. The expected positions of the IQHE plateaux are shown in blue.

the von Klitzing constant). There is no bending in the low-field hall trace, and neither are there any plateaux that arise at odd-integer fractions of the von Klitzing constant [61], which would indicate a significant parallel conduction channel or a second occupied subband.

We note that the SdH oscillations do not approach  $0 \Omega$  sheet resistance at high fields, which may be an indication of some parallel conduction channel. However, as we have shown in Fig. 6.11 that the Hall carrier density is experimentally identical to the carrier density extracted from the Fourier transform of the SdH oscillations, we are confident that the contribution that this channel makes to transport is negligible.

We corroborate this evidence of the absence of two subband transport by considering the gate to channel capacitance [111, 127]. In an ideal 2DEG system, the charge carriers are confined to a single plane and therefore the gate to channel capacitance should be constant. However, the appearance of an additional minimum in energy will enhance the density of available states at the Fermi level, and so will change how the 2DEG within the quantum well screens the electric field applied by a top gate. This change in screening potential will alter the capacitance as we start to observe a second subband

[127].

To measure the capacitance, we made a low-pass RC filter. We place a known 470 k $\Omega$  resistor in series with the top gate and apply a 10 mV AC signal with a low frequency (7 Hz). We then increase the frequency of that signal until the voltage drop across the top gate electrode to the channel (measured with a lock-in amplifier) drops to half its original value. From this, we can extract the capacitance, using

$$G = \frac{1}{\sqrt{1 + (\omega RC)^2}} \quad (6.3)$$

where  $G$  is the ratio between the unattenuated voltage and the final measured voltage (in this case fixed at 0.5),  $R$  is the resistance of the known resistor,  $\omega$  is the angular frequency applied and  $C$  is the capacitance.

A DC offset is then applied on top of the AC signal to alter the carrier density within the quantum well, analogous to applying a top gate bias in other measurements, and the measurement is repeated. The results of this study are shown in Fig 6.13. It is worth noting that after application of the 10 mV AC signal across the top gate there is a significant hysteresis, where the carrier density is now significantly higher than the as-cooled carrier density. It is possible that the high frequencies needed to determine the capacitance (up to 1.65 kHz) cause the top gate to inductively couple to impurities beneath the quantum well, causing the hysteric behaviour in the carrier density.

We can see that the step in the capacitance, associated with the occupation of a second subband, occurs far away from the peak in Hall mobility. In fact this step in capacitance occurs at a Hall carrier density of  $(22.9 \pm 0.2) \times 10^{11} \text{ cm}^{-2}$ , which was measured after completing the capacitance measurements. This carrier density is experimentally identical to the carrier density at which a new peak is seen in the Fourier spectrum of the SdH oscillations, recorded as  $(22.7 \pm 0.2) \times 10^{11} \text{ cm}^{-2}$ . It is worth noting that, even if there was no hysteresis in the carrier density, the step in capacitance would not occur at the peak in Hall mobility, instead arising at a Hall carrier density of  $(16.9 \pm 0.2) \times 10^{11} \text{ cm}^{-2}$ , after the peak in Hall mobility (.

Having shown that the occupation of a conventional second excited electronic subband is not responsible for the local maximum in Hall mobility, we once again consider the quantum lifetime of the carriers as we sweep the carrier density through the peak regime. We find that the Dingle ratio reaches a maximum at the mobility peak, and then proceeds to rapidly fall off as the Hall mobility decreases, as shown in Fig. 6.14b.

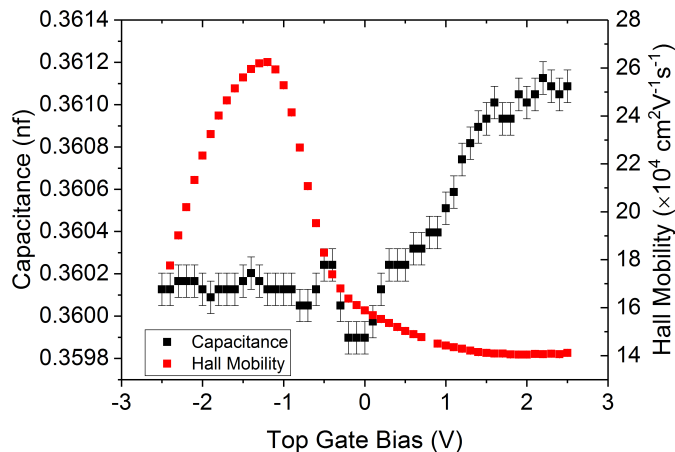


Figure 6.13: Top gate to channel capacitance plotted as a function of DC top gate bias at 1.5 K, with the back gate grounded. The subsequently measured Hall mobility is plotted in red, for comparison

We also note that the effective mass reaches a maximum as we sweep the carrier density through the peak regime, implying that there is some change in the band structure across the mobility peak, even though the SdH oscillations still arise from a single envelope function, as in Fig. 6.12. The effective mass, Dingle ratio, transport scattering time and the quantum lifetimes associated with this result are shown in Fig. 6.14.

The quantum lifetime shows some interesting features within this regime. After initially increasing with increasing carrier density (as in section 6.4), the quantum lifetime saturates at a carrier density of  $(15.5 \pm 0.2) \times 10^{11} \text{ cm}^{-2}$ . This could be due to the screening potential of the first occupied subband saturating at this point [120, 126]. Subsequently, we find that there is a sudden drop in the quantum lifetime at a carrier density of  $(17.6 \pm 0.2) \times 10^{11} \text{ cm}^{-2}$ , followed by an increase in the quantum lifetime, even as the transport scattering time decreases.

An increase in quantum lifetime would imply that low angle scattering events become unfavourable, which can occur as a new subband is populated. Specifically, as a new subband becomes occupied, the states occupying that new subband will screen the system from impurities, as in the single subband case. However, the states occupying this new subband are limited by the size of the new subband in  $k$ -space. Therefore,

## 6.5 Scattering in the Peak Regime

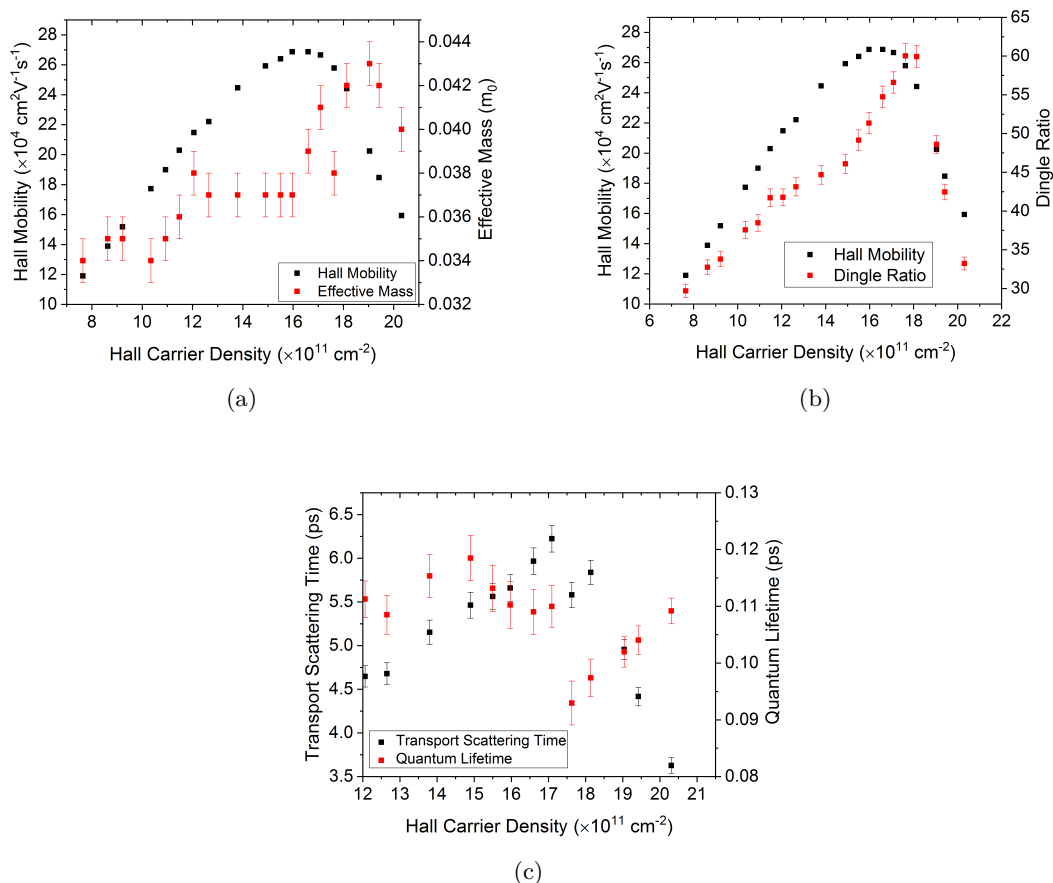


Figure 6.14: Fig. 6.14a shows the effective mass (in units of free electron mass) and the variation in Hall mobility across the peak and low carrier density regimes. Fig. 6.14b shows the ratio between the transport scattering time and the quantum lifetime (also known as the Dingle ratio) and the variation in Hall mobility across the peak and low carrier density regimes. Fig. 6.14c shows the transport scattering time and quantum lifetime as a function of Hall carrier density, in the peak regime. The effective mass and Dingle ratio needed to extract this data was derived from fitting the SdH amplitude as a function of temperature up to 20 K at each top gate bias.

the screening provided by the states within this new subband will be greatly reduced if the momentum transferred in a scattering event is greater than  $2k_F$ , where  $k_F$  is the wavevector of the new state at the Fermi energy [117, 128]. This will selectively screen

the scattering within the system, so that scattering events with a small momentum transfer, and therefore a small scattering angle, become unfavoured, which results in the increase in the quantum lifetime we see.

Additionally, we measured the in-plane magnetoresistance of the wafer. Applying a magnetic field in the plane of the device will modify the momentum of the carriers by the magnetic vector potential, such that the momentum at some applied magnetic field will be  $p_B = (p_0 + qA)$ , where  $A$  is the magnetic vector potential and  $q$  is the charge on the particle. This modifies the simple 2D Hamiltonian from  $E = \frac{p_0^2}{2m^*}$  to

$$E = \frac{1}{2m^*}(p_0^2 + 2qAp_0 + q^2A^2) \quad (6.4)$$

where  $p_0$  is the momentum of the carrier in the absence of a magnetic field.

The result of this modification to the Hamiltonian is that if only a single subband is present, the Fermi surface will be distorted and will no longer be isotropic. This leads to a positive magnetoresistance, as increasing the magnetic field will increase the distortion of the Fermi surface, reducing the average quantum lifetime, and so increasing the scattering rate [129]. However, if two states with different momenta exist near to the Fermi energy, this may change as the second term in equation 6.4 will move the two states relative to each other [129, 130]. This will be further enhanced if the two states have opposite charges (i.e the sign of  $q$  is different for each subband) [35].

If scattering between the two momentum states is permitted, such as scattering between the first and second occupied subbands [40], or scattering within a band with low- $k$  states arising from quantum well coupling [118, 131], then the position of the low- $k$  state can be shifted with an applied field, away from  $k = 0$ . This shift of  $k$ -states will reduce the number of scattering paths available and the resistance of the system will decrease. A schematic diagram of the effects of an in plane magnetic field is shown in Fig. 6.15. The suppression of scattering, associated with the shift of a second subband with respect to the first occupied subband due to the in-plane magnetic field, is usually seen as a maximum in the resistance at zero applied in plane field. In particular, as the two subbands are shifted relative to one another, the width (in magnetic field) of the zero-field maximum in resistance will be related to the Fermi wavevector,  $k_F$  of the inner subband. This makes the in-plane magnetoresistance an extremely sensitive probe of the band structure, as it depends on the availability of states in  $k$ -space that act as scattering paths, not the occupation of those states. [35, 118, 119].

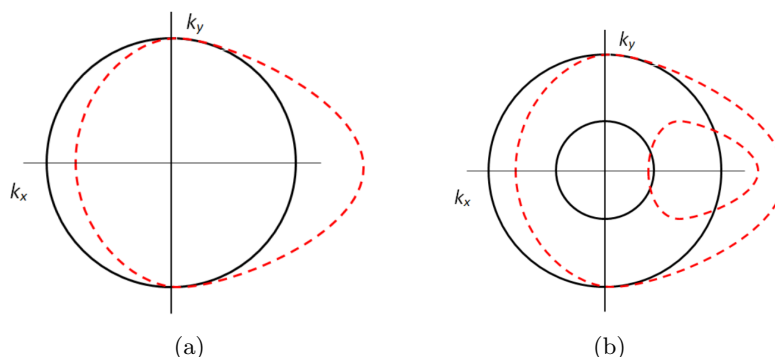


Figure 6.15: Schematic diagrams of the 2D Fermi surface at a constant energy at 0 magnetic field (solid black lines) and including an in-plane magnetic field in the  $x$  direction (dashed red lines). Fig. 6.15a illustrates the case where a single subband is occupied, whereas Fig. 6.15b shows the case in which there are additional low- $k$  states at the Fermi energy. Following [129].

In the absence of an applied gate bias, the magnetoresistance, shown in Fig. 6.16, is much larger when the current is applied parallel to the magnetic field ( $B_x$ ,  $R_{xx}$ ) than in the case where the current is applied perpendicular to the magnetic field ( $B_x$ ,  $R_{yy}$ ). It is unclear precisely why this anisotropy exists. Similar studies on GaAs/AlGaAs quantum wells have noted that anisotropies similar to the ones we observe here can be linked to “stripes” forming during MBE growth. If current is applied parallel to these stripes, the magnetic flux of the external field passing through the 2DEG will be minimal. However, if the current is applied perpendicular to these stripes, there will be an additional flux passing through the 2DEG as it follows the surface contour, increasing the observed magnetoresistance [132, 133]. It is worth noting that these anisotropies have also been linked to the in-plane field coupling to the spin-orbit interactions within GaAs/AlGaAs 2DEGs [134].

In Fig. 6.16, we observe that there is a maximum in the resistance for an in-plane magnetic field  $B_{||} = 0$ , when the magnetic field is applied perpendicular to the current ( $B_x$ ,  $R_{yy}$ ). We can also see that, in this orientation, after the sheet resistance reaches a minimum at a finite in-plane field, the magnetoresistance returns to being parabolic with increasing applied magnetic field. This indicates that the scattering paths between the high- $k$  and low- $k$  states have been quenched and the main contri-

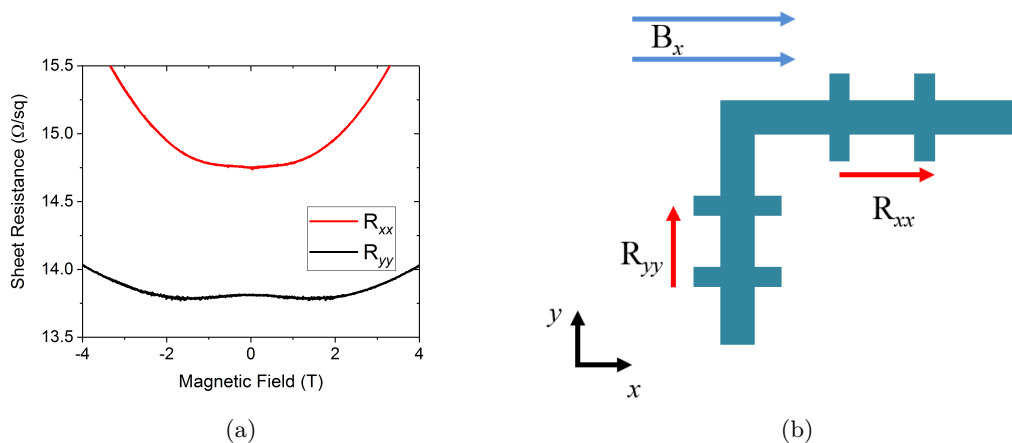


Figure 6.16: Fig. 6.16a shows the in-plane magnetoresistance in a device of G0186 at 1.5 K, in the absence of a gate bias, for two different current orientations. The black curve shows the field orientated at right angles to the current direction, whereas the red curve shows the current orientated parallel to the magnetic field. This current-field alignment is shown schematically in Fig 6.16b, where the blue arrows represent the direction of the applied magnetic field, and the red arrows represent the direction along which the magnetoresistance was measured.

tribution to the magnetoresistance comes from the distortion to the Fermi surface, as in the single-subband case [129, 130].

If we consider Fig. 6.15b, an applied magnetic field in the  $x$  direction will shift the low- $k$  set of states away from  $k_x = 0$ . However, if we apply a current along the  $y$  axis, the majority of states we observe in our transport measurement will lie at  $k_x = 0$ . Therefore, as we apply an in-plane field, there will come a point where the low- $k$  set of states will no longer cross  $k_x = 0$  (the dashed lines in Fig. 6.15b), and so scattering between the high- $k$  and low- $k$  states will be suppressed. We can use this behaviour to extract some information about the Fermi surface, as the full width at half-maximum (FWHM) of the  $B_{||} = 0$  resistance maximum will be proportional to the Fermi wavevector,  $k_F$ , of these low- $k$  states [119].

We therefore investigate the in plane magnetoresistance as a function of top gate bias when the current is applied perpendicular to the magnetic field ( $B_x$ ,  $R_{yy}$ ). We find that only at gate biases within the mobility peak regime is there a resistance maximum

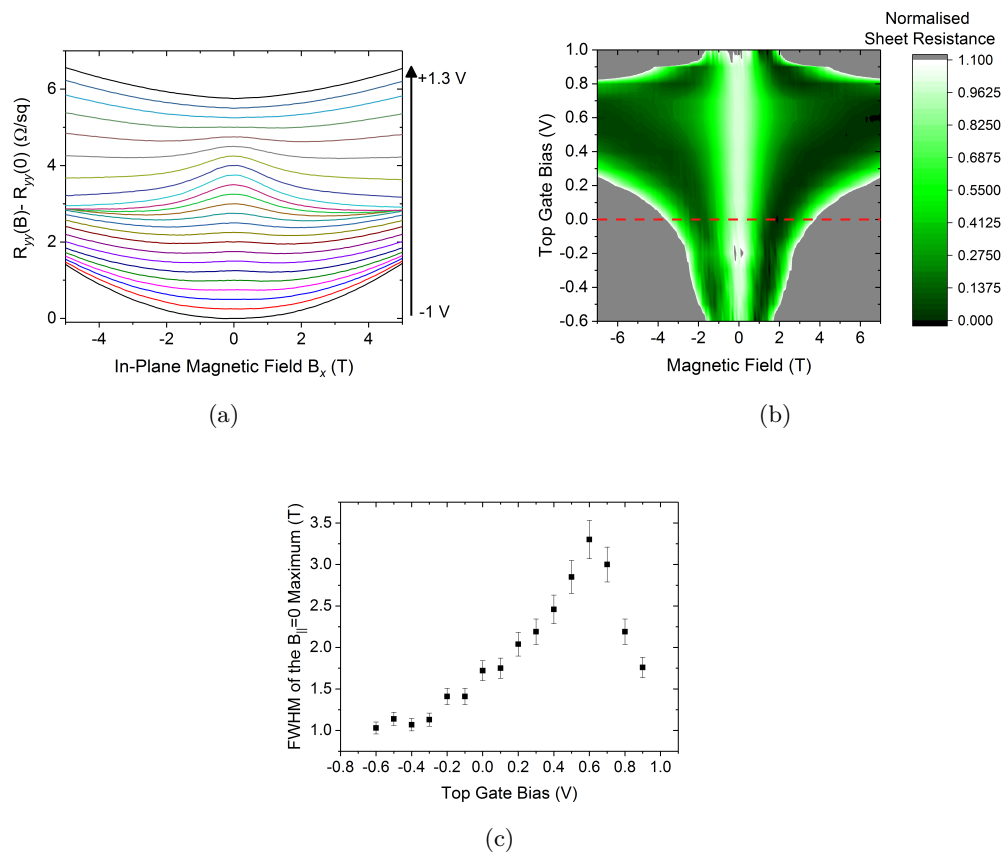


Figure 6.17: Fig. 6.17a shows the change in the in-plane magnetoresistance in a device of G0186 at 1.5 K for a range of top gate voltages (with a top gate step of 0.1 V), where the magnetic field was applied perpendicular to the current direction ( $B_x$ ,  $R_{yy}$ ). The curves are artificially offset for clarity. Fig. 6.17b is a contour plot of the normalised sheet resistance as a function of both top gate bias and applied in-plane magnetic field in the region where a  $B_{||} = 0$  maximum is present. The grey areas show where the resistance increases past the  $B_{||} = 0$  value, and therefore where the magnetoresistance returns to being parabolic, as in the single subband case. The black curve in Fig. 6.16a is a cross-section of Fig. 6.17b at the red dashed line. Fig. 6.17c shows the FWHM extracted from Fig. 6.17b as a function of top gate bias. The peak region is identified as being between  $\pm 0.6$  V top gate bias from subsequent measurements of the carrier density.

at  $B_{||} = 0$ , first appearing at  $-0.6$  V applied top gate bias. At more negative biases, the magnetoresistance is approximately parabolic, as we expect from transport that appears to arise from a single occupied subband. When a large positive top gate bias has been applied, and as such the system is in the high carrier density regime, the magnetoresistance is no longer parabolic, instead appearing “V” shaped, without a noticeable  $B_{||} = 0$  maximum.

We note, from Fig. 6.16a, that the magnitude of the  $B_{||} = 0$  maximum in sheet resistance ( $0.15 \pm 0.01 \Omega$ ) is small compared with the change in sheet resistance due to application of a top gate bias ( $\approx 25 \Omega/\text{V}$  in the mobility peak regime). As such, in order to illustrate how an applied gate bias changes the  $B_{||} = 0$  maximum in resistance, we normalise our sheet resistance data, so that the sheet resistance at  $B_{||} = 0$  is 1, and the minimum resistance is 0. This data is then shown in Fig. 6.17.

When  $-0.6$  V top gate bias is applied (at the onset of the  $B_{||} = 0$  maximum in resistance) the measured sheet resistance is comparable with that seen at a Hall carrier density of  $(14 \pm 1) \times 10^{11} \text{ cm}^{-2}$ , in the absence of a magnetic field (on the same device). Coincidentally, this carrier density is where the Hall mobility in Fig. 6.5 starts to deviate significantly from the simple  $\mu \propto n^{1.64}$  dependence that is seen in the low carrier density regime.

Having normalised our data it is now easy to see that, as we apply a more positive top gate bias, and move through the mobility peak regime, the  $B_{||} = 0$  resistance maximum becomes more prominent. This continues to be the case until a top gate bias of  $+0.6$  V is applied, after which a more positive top gate bias results in a narrower  $B_{||} = 0$  maximum.

In order to quantify this, we calculate the FWHM of the  $B_{||} = 0$  resistance maximum, and plot this in Fig. 6.17c as a function of top gate bias. The FWHM increases as we move through the mobility peak regime. As such, we conclude that this regime is characterised by the appearance of a new set of states near the Fermi energy that grow as we apply a more positive top gate bias, and therefore increase the carrier density.

The FWHM reaches a maximum at a  $+0.6$  V applied top gate bias, where the measured sheet resistance, in the absence of a magnetic field, is comparable with that seen at a Hall carrier density of  $(20 \pm 1) \times 10^{11} \text{ cm}^{-2}$  in the absence of a magnetic field. This carrier density corresponds with the carrier density at which the relative magnitudes of the top and back gate biases start becoming relevant to the electronic transport

---

## 6.6 Scattering in the High Carrier Density Regime

(as shown in Fig. 6.5), and where the envelope function of the SdH oscillations start to change (as shown in Fig. 6.3), signalling the occupation of a second, electron-like subband and onset of the high carrier density regime. We will discuss the importance of this correlation in section 6.8.

When the carrier density is between  $12 \times 10^{11} \text{ cm}^{-2}$  and  $20 \times 10^{11} \text{ cm}^{-2}$ , a peak in Hall mobility is observed, qualitatively similar to those seen in single InAs quantum wells [120], which appears as a second electron subband is populated. However, we have shown that, unlike conventional InAs quantum wells, the peak in Hall mobility seen here does not coincide with the population of a conventional electron-like subband, as shown in Fig. 6.11. However, we observe the appearance of states available for scattering at a carrier density of  $(14 \pm 1) \times 10^{11} \text{ cm}^{-2}$ , from the in-plane magnetoresistance. This is then followed by an increase in the quantum lifetime, consistent with the population of those states, at a carrier density of  $(17.6 \pm 0.2) \times 10^{11} \text{ cm}^{-2}$ , even though no new states are observed in the SdH oscillations at these carrier densities (as in Fig. 6.12).

## 6.6 Scattering in the High Carrier Density Regime

When high positive gate biases are applied such that the Hall carrier density  $\geq 20 \times 10^{11} \text{ cm}^{-2}$ , a second electronic subband starts to become relevant to transport, as seen in the SdH oscillations in Fig. 6.3 and in the Fourier spectrum of those same oscillations in Fig. 6.11.

In this high density regime, we find that the relative magnitudes of the top and back gate biases have a measurable effect on the Hall mobility (shown in Fig. 6.18, which highlights the relevant section of Fig. 6.5) from the point highlighted with a red arrow in Fig. 6.18. Specifically, if we compare two points in Fig. 6.18 with similar carrier densities, a more negative back gate bias will result in a lower Hall mobility. Furthermore, when we consider the in plane magnetoresistance in the high carrier density region, we notice that the FWHM of the  $B_{\parallel} = 0$  maximum in resistance decreases before the vanishing entirely at a carrier density of  $(22 \pm 1) \times 10^{11} \text{ cm}^{-2}$  (as shown in Fig. 6.17). This implies that in this regime, we can no longer shift the bands relative to one-another. This is surprising, since we would expect to be able to shift the position of the second electron-like subband relative to the first excited electron subband [119]. We discuss this further in section 6.8.

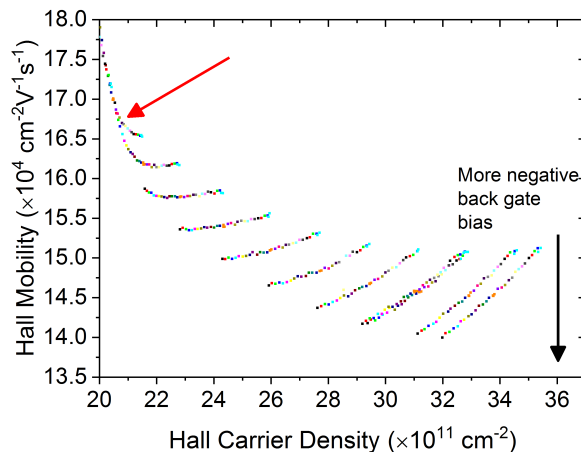


Figure 6.18: Hall mobility as a function of Hall carrier density in the high carrier density regime at 1.5 K. The different coloured points represent different back gate biases between  $\pm 2.5$  V. The transition from the unified trend in mobility with Hall carrier density to the regime where the relative top and back gate biases are important to transport is highlighted with a red arrow.

## 6.7 Wafer Dependence of Scattering

Hall mobility and quantum lifetime measurements were repeated on devices made from wafer G0156. G0156 is a nominally similar wafer to G0186, but was grown on  $n^+$  GaAs, with a 4  $\mu\text{m}$  thick GaSb buffer layer to remove strain related defects from the channel. Initially, we performed ordinary Hall effect measurements as a function of both top and back gate bias. We plot the extracted Hall mobility as a function of Hall carrier density in Fig. 6.19.

We note that, as in wafer G0186, the back gate affects the Hall and SdH carrier densities equally. We also observe qualitatively similar behaviour in the Hall mobility. However, we find that the peak in mobility shifts to a lower density of  $(14.9 \pm 0.1) \times 10^{11} \text{ cm}^{-2}$ , compared to  $(15.9 \pm 0.2) \times 10^{11} \text{ cm}^{-2}$  (G0186). Additionally, a second electronic subband is seen in the Fourier spectrum of the SdH oscillations at the lower carrier density of  $(18.9 \pm 0.2) \times 10^{11} \text{ cm}^{-2}$ , when compared to the carrier density where SdH oscillations in G0186 are no longer bound by a single envelope function,  $(20.1 \pm 0.2) \times 10^{11} \text{ cm}^{-2}$ . These shifts in the carrier densities could be due

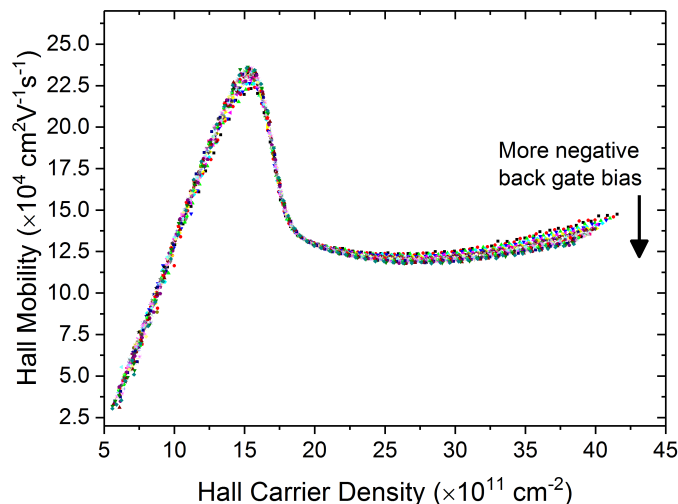


Figure 6.19: Hall mobility as a function of Hall carrier density in wafer G0156, grown on GaAs. The different colours represent different back gate biases between  $\pm 3$  V.

to the strain placed on the quantum well by growing the heterostructure on the lattice mismatched  $n^+$  GaAs substrate [23]. However, they could also be due to small inconsistencies in the MBE growth conditions [80].

As shown in Fig. 6.20, the scattering within G0156 has a very weak temperature dependence up until  $47 \pm 3$  K, after which acoustic phonon mediated scattering dominates transport. Additionally, the Hall mobility in the low carrier density regime is characterised by  $\mu \propto n^\beta$ , where  $\beta = 1.30 \pm 0.05$ , indicating that the dominant scattering is from remote impurity states, as in G0186 (where  $\beta = 1.68 \pm 0.05$ ). We also note that, after a carrier density of  $(18.0 \pm 0.2) \times 10^{11} \text{ cm}^{-2}$ , the relative magnitudes of the top and back gate biases start being relevant to the Hall mobility, with a more negative back gate bias resulting in a lower Hall mobility for a similar carrier density, as in the high carrier density regime in G0186.

Finally, we consider the quantum lifetime and effective mass of carriers within wafer G0156 as we sweep the top gate voltage. The effective mass shows a similar dependence to wafer G0186. The measured effective mass does not change significantly throughout the low carrier density regime, but increases to a maximum at a Hall carrier density shortly after the peak in the Hall mobility, shown in Fig. 6.21a. However, the quantum

## 6.7 Wafer Dependence of Scattering

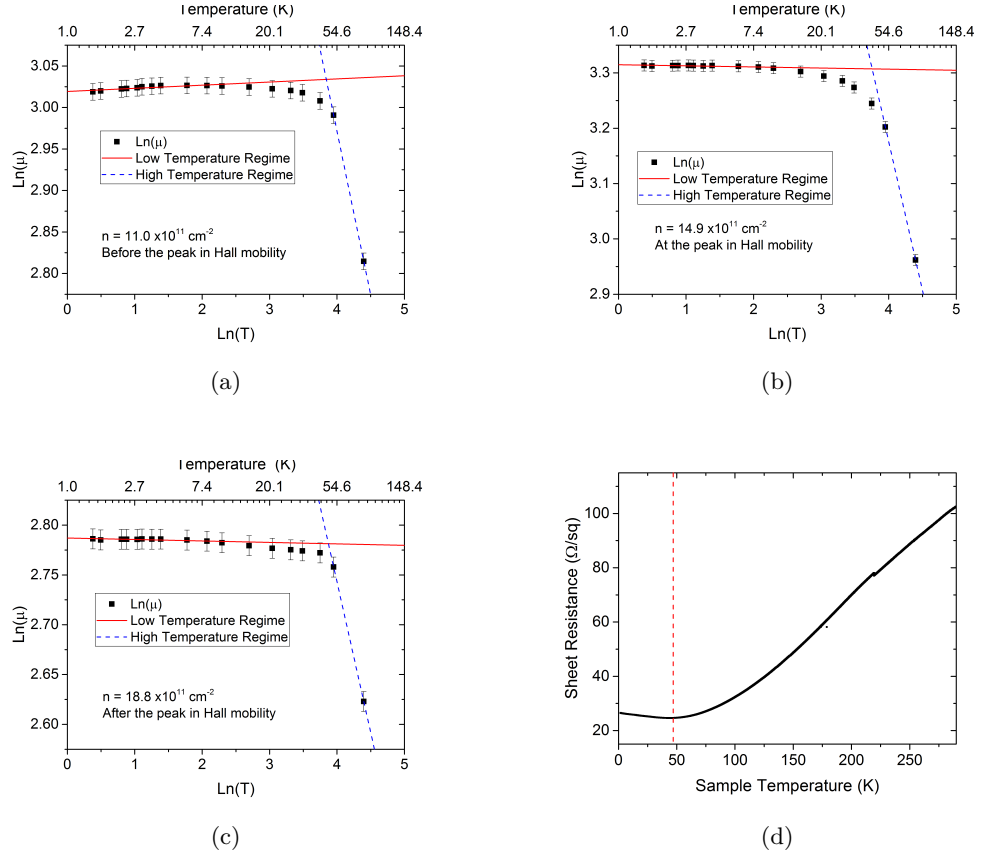


Figure 6.20: Log-log plots of the Hall mobility against sample temperature at a constant carrier density in wafer G0156, used to determine the dominant scattering mechanism. The solid red lines represent the fit over the low temperature ( $T < 20$  K) regime, whereas the dashed blue lines represent the fit over the high temperature ( $T > 50$  K) regime. Fig. 6.20a represents a carrier density of  $(11.1 \pm 0.1) \times 10^{11} \text{ cm}^{-2}$  (in the low carrier density regime); Fig. 6.20b represents a carrier density of  $(14.9 \pm 0.2) \times 10^{11} \text{ cm}^{-2}$  (at the peak in Hall mobility) and Fig. 6.20c represents a carrier density of  $(18.8 \pm 0.2) \times 10^{11} \text{ cm}^{-2}$  (in the high carrier density regime). For comparison, Fig. 6.20d shows the sheet resistance as a function of temperature on the same sample, with  $T = 47$  K marked by the red, dashed line.

lifetime does not show the sudden drop at the mobility peak, seen in Fig. 6.14c, although the rise in quantum lifetime even as the transport scattering time falls is still

Carrier Density ( $\times 10^{11} \text{cm}^{-2}$ )	Low Temperature Fit	High Temperature Fit
$11.0 \pm 0.1$	$0.040 \pm 0.008$	$-0.4 \pm 0.1$
$14.9 \pm 0.2$	$-0.020 \pm 0.008$	$-0.5 \pm 0.1$
$18.8 \pm 0.2$	$-0.001 \pm 0.008$	$-0.3 \pm 0.1$

Table 6.3: Table of extracted power law exponents from the graphs in Fig. 6.20

present, as shown in Fig. 6.21c. We note, however, that there is still the rise in quantum lifetime after the peak in Hall mobility, indicating that the peak in mobility here is also due to the appearance of a new set of states at the Fermi energy. In conclusion, the two separate wafers, grown on separate substrates, show remarkably similar behaviours when the carrier density is modulated by an applied gate voltage.

## 6.8 Discussion

We have shown, through measurements of the Hall mobility, quantum lifetime, and in-plane magnetoresistance, that the transport within coupled, InAs/GaSb quantum wells can be described by three regimes. The first of these regimes is the low carrier density regime, where the scattering is limited by screening from the 2DEG within the InAs layer. This is followed by an intermediate carrier density regime, where new states appear near the Fermi energy, creating a  $B_{\parallel} = 0$  maximum in the in-plane magnetoresistance. As these states are populated, a fall in the Hall mobility and a simultaneous rise in the quantum lifetime is observed, all in the absence of a second carrier gas contributing to the SdH oscillations. Finally, at the highest measured carrier densities two electron-like subbands are visible in the SdH oscillations. In this regime the Hall mobility becomes dependent on the relative top and back gate biases, whereas at all lower carrier densities the carrier mobility depended solely on the total Hall carrier density of the system. It is worth noting, however, that the dominant scattering mechanism at all carrier densities (below  $T \leq 50$  K) is scattering from remote impurities. This is determined from the temperature dependence of the mobility, the screening provided in the low carrier density region, and the high Dingle ratio within the low and peak carrier density regimes [60].

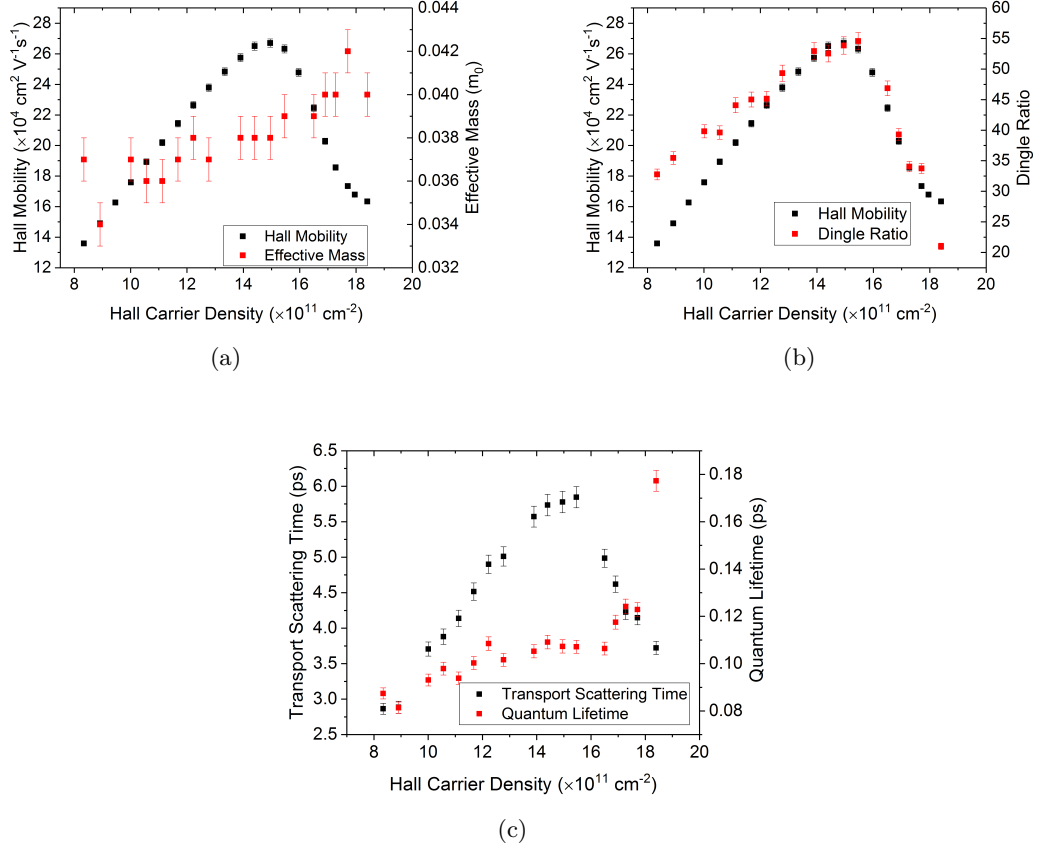


Figure 6.21: Fig. 6.21a shows the effective mass and variation in Hall mobility in wafer G0156 as a function of top gate bias. Fig. 6.21b shows the Dingle ratio and variation in Hall mobility over the same gate bias range. Fig. 6.21c shows the transport scattering time and quantum lifetime, derived from Figs 6.21a and 6.21b. The effective mass and Dingle ratio needed to extract this data was derived from fitting the SdH amplitude as a function of temperature up to 20 K at each top gate bias.

The low carrier density regime shows behaviour analogous to a single 2DEG. No matter how the top and back gates are biased, an increase in carrier density results in an increase in the screening from the remote impurities. However, from Figs. 6.18 and 6.19, in the high carrier density regime, we know that the back gate does not affect the mobility, and therefore the band structure, in the same way as the front gate, implying that the back gate influences the energies within the GaSb layer. This seems

reasonable, as studies on coupled quantum wells tuned into the charge-neutral regime solely by depleting carriers in the InAs layer show that the intrinsic carrier density in the GaSb layer is approximately  $(0.2 - 0.6) \times 10^{11} \text{ cm}^{-2}$  [10, 32, 135]. As double GaAs/Al<sub>x</sub>Ga<sub>1-x</sub>As quantum wells show that a carrier density greater than  $0.7 \times 10^{11} \text{ cm}^{-2}$  in a lower well can completely screen the action of a back gate from the upper quantum well [34], the electric field produced by the back gate should be affected by the GaSb layer, and be screened from the InAs layer. How then, does the back gate modulate the electron-like carrier density at all, given that we see no evidence of electron-hole transport at these gate biases?

We attribute the modulation of the carrier density with an applied back gate voltage to a shift of the anticrossing point in energy as we apply a bias to the GaSb layer. To illustrate the effect that applying a gate bias has on the band structure of this heterostructure, we define a simplified model of the coupled quantum well system, as in chapter 2. We consider the first and second excited electron subbands, and the highest heavy-hole subband. We neglect electron-electron interactions and SOC. We also assume that the first electron subband and the second electron subband couple to the highest heavy-hole subband in exactly the same way, with exactly the same coupling strength. Specifically, there should be nothing limiting the coupling between higher order electron subbands and the hole subbands, as all electron-like subbands extend into the GaSb layer [25], but the coupling strength may be weaker [30]. Under these assumptions, the Hamiltonian of the system becomes:

$$\begin{bmatrix} H_{e1} & 0 & \Delta \\ 0 & H_{e2} & \Delta \\ \Delta & \Delta & H_h \end{bmatrix}, \quad (6.5)$$

where the values of  $H$  are the Hamiltonians of the uncoupled subbands, the subscripts e1, e2, and h represent the dispersions of the first electron subband, the second electron subband, and the highest energy heavy hole subbands respectively, and  $\Delta$  is the strength of the electron-hole coupling. We assume that the uncoupled electron Hamiltonians are parabolic, with an effective mass of  $0.032 m_0$ , and the hole subband is similarly parabolic, with an effective mass of  $-0.4 m_0$  [21]. In our models, we treat  $\Delta$  as a constant with respect to  $k$ . This is technically incorrect [4], but it is useful to illustrate schematically the effect that inter-band coupling has on the dispersion relations within this coupled quantum well system.

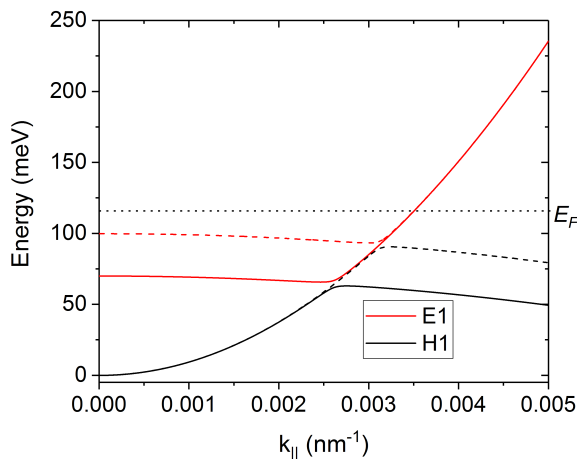


Figure 6.22: Dispersion relations of the first excited electron (red) and heavy hole (black) bands in the absence of an applied negative back gate bias (solid lines) and in the presence of a negative voltage applied across the back gate, shifting the hole bands up by 30 meV (dashed lines). Band offsets were taken from [25]. The bottom of the uncoupled InAs band is set as zero energy. An example Fermi energy that would be in the low carrier density regime is shown by the black dotted line.

As a small change in heavy-hole subband energy should not change the strength of the coupling,  $\Delta$ , we numerically compute the eigenvalues of equation 6.5 [4]. We then repeat the calculation in the case where the uncoupled heavy hole subband has been shifted 30 meV higher without any change to the energies of the electron subbands. This should be analogous to applying a negative bias voltage to the back gate in our system, if the resulting electric field is completely screened from the InAs layer. We plot the first electron-like (E1) and hole-like (H1) subbands in Fig. 6.22. It is worth noting that this 30 meV shift is approximately two orders of magnitude larger than any energy shift we have been able to create with our back gates, and is used to emphasise the effect [49].

As any inter-well tunnelling event will have to conserve angular momentum, the spin  $\pm\frac{1}{2}$  electron-like states cannot couple directly to the spin  $\pm\frac{3}{2}$  heavy hole states. Therefore, an intermediary state is required, in the form of the spin  $\pm\frac{1}{2}$  light holes, which the electrons can couple directly to. These light holes then mix with the heavy

holes at finite  $k_{\parallel}$ , when spin is no longer a good quantum number [4]. As such, at  $k_{\parallel} = 0$ ,  $\Delta$  in equation 6.5 vanishes, and the energy eigenvalues of the matrix become the energies of the uncoupled electron and hole subbands. Therefore, at  $k_{\parallel} = 0$ , due to the electron-hole anticrossing, the energy of the conduction band (E1) must be equivalent to the energy of the uncoupled heavy hole band (H1) at the same wavevector.

If we apply a gate bias to the GaSb layer and shift the maximum of the uncoupled heavy hole band (H1), the effect on the coupled system will be to shift the energy of the hybridised electron-like subband (E1) at  $k_{\parallel} = 0$ . In this way, as long as our Fermi energy is mid-conduction band (i.e. the Fermi energy crosses E1 but does not cross any states in H1), applying a small bias to the back gate will modulate electron-like states, by shifting the energy at which the InAs conduction bands anticross the GaSb valence bands. For example, if we apply a negative back gate bias (as in Fig. 6.22) this will result in states being depleted from the bottom of E1. This will decrease the carrier density, resulting in the behaviour we see in Figs. 6.2a and 6.9.

Therefore, in the low carrier density regime, both the top and back gates should have an identical effect on the bandstructure and the Hall mobility. As a negative bias across either gate will deplete electron-like states from the conduction band, the screening the 2DEG provides will be similarly reduced, resulting in the behaviour seen in Fig. 6.8. We note that we have not considered the second electron-like subband in this model, as it is too high in energy.

As we increase the carrier density, we enter the mobility peak regime, where we know that a new set of states appear in  $k$ -space, initially detected by the emergence of a  $B_{\parallel} = 0$  maximum in the in-plane magnetoresistance, shown in Fig. 6.17. As we move through this regime, the screening from these new states begins to affect the quantum lifetime and the Hall mobility drops as shown in Fig. 6.14.

To model this regime, we return to the model described in equation 6.5, and move both electron bands down in energy while keeping the hole band fixed, as if a positive bias voltage was applied across the top gate and the resulting electric field is completely screened from the GaSb layer. The dispersion relations of the first (E1) and second (E2) excited electron-like subbands are plotted in Fig. 6.23, where we show a dispersion relation shifted 50 meV down relative to the case where no energy shift has taken place (the dispersion of the hole-like subband H1 is not shown for simplicity). Note that the solid lines in Fig. 6.23 are exactly the same as the solid lines in Fig. 6.22. If we

consider the system as a single 2DEG, with a Fermi energy of  $E_F = \frac{\pi \hbar^2 n}{m^*}$  [49], this 50 meV energy shift would result in the excitation of  $6.7 \times 10^{11} \text{ cm}^{-2}$  extra electron-like carriers, and so is well within the capabilities of our top gate.

If we just consider the first excited subband (E1), we note that the energy minimum of this subband moves to a lower energy as we apply a more positive top gate bias. This is expected, as we effectively move the anticrossing point between the electron (E1) and highest hole (H1) subbands down in energy by shifting the energy of the InAs layer with the applied bias. As we move this anticrossing point down in energy, more states will become available, allowing us to excite carriers by applying a more positive top gate bias. This continues the trend seen in the low carrier density regime, where the top and back gates both have an effect on the electron-like carrier density.

More interesting is the behaviour of the bands near  $k_{\parallel} = 0$ . Recall that, within this system, we have neglected electron-electron interactions. However, due to the second electron-like subband (E2) being energetically close to what was formerly the uncoupled hole dispersion (E1 at  $k_{\parallel} = 0$ ), a new anticrossing gap forms [30]. This will mean that, should our Fermi energy be within this new anticrossing gap (as in Fig. 6.23), there will be a range of energies where, due to this new anticrossing gap, the second electron-like subband, E2, will be unable to cross the Fermi energy. This additional anticrossing explains why we see vacant states near the Fermi energy in the in-plane magnetoresistance in wafer G0186, even though no new states are populated until a much higher carrier density is reached. These vacant states are responsible for the  $B_{\parallel} = 0$  maximum seen at low carrier densities in Fig 6.17.

As we apply a more positive gate bias (to either gate) and increase the carrier density through the peak regime, the bottom of the second electron-like subband (E2) eventually crosses the Fermi energy. As it does so, the states at the bottom of the second electron-like subband will become populated. However, due to the anticrossing shown in Fig. 6.23, these states will have the dispersion of a heavy-hole band, and as such will have poor mobility in comparison to the first electron-like subband (E1). It is worth emphasising that although these hybridised states at the bottom of E2 have a hole-like dispersion, they are electron-like states, with a negative charge [4], and as such we do not see electron-hole transport in our Hall data. Due to this low mobility, they do not appear in the SdH oscillations at accessible magnetic fields.

Scattering between the first electron-like subband and this new hybridised subband

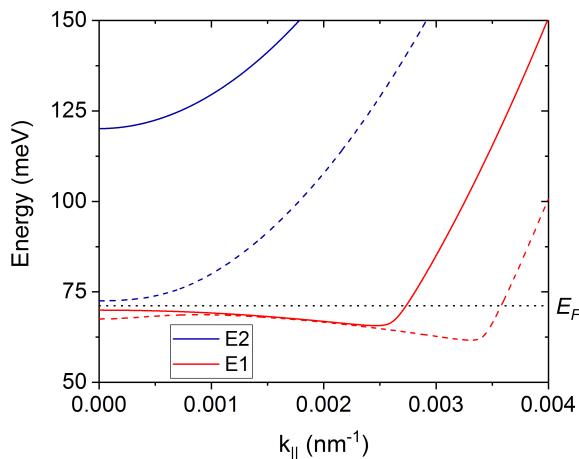


Figure 6.23: Dispersion relations of the first (red) and second (blue) excited electron subbands in the absence of an applied gate bias (solid lines, replicated from Fig. 6.22) and in the presence of a positive voltage applied across the top gate, shifting the electron bands down by 50 meV (dashed lines). An example Fermi energy is indicated by the dotted black line. This should be the state the of system at the onset of the peak regime. Band offsets were taken from [25]. The bottom of the uncoupled InAs band is set as zero energy.

causes the Hall mobility to drop, as shown in Figs. 6.5 and 6.19. Additionally, the presence of a new subband alters the screening potential of the system, resulting in the increase in quantum lifetime as the Hall mobility drops, displayed in Figs. 6.14c and 6.21c. In this way, the peak in Hall mobility is analogous to the peak in carrier mobility arising from inter-subband scattering seen in conventional InAs quantum wells [120]. However, due to the anticrossing behaviour exhibited in these coupled quantum wells, the population of a second, electron-like subband is not visible in the SdH oscillations until the carrier density is increased still further, as shown in Fig. 6.11.

The anticrossing between the second excited electron subband and the heavy hole subband may go some way to explaining the change in the low temperature dependence of the Hall mobility observed in Fig. 6.7 and Table 6.2. As there are now states available for scattering that do not cross the Fermi energy, a finite energy is needed to access these states. As the temperature of the system is increased, more of these states will

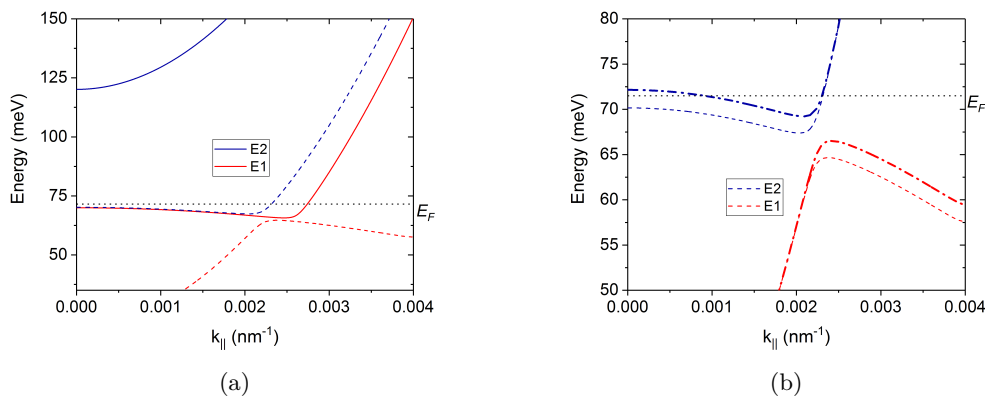


Figure 6.24: Dispersion relations of the first (red) and second (blue) excited electron subbands. An example Fermi energy is indicated by the dotted black line. Fig. 6.24a shows the relevant subbands in the absence of an applied gate bias (solid lines, replicated from Fig. 6.22) and in the presence of a positive voltage applied across the top gate, shifting the electron bands down by 100 meV (dashed lines). Both traces in Fig. 6.24b show the relevant bands under a positive top gate bias shifting the electron bands down by 100 meV. As such, the dashed trace in this figure corresponds to the dashed trace in Fig. 6.24a. However, the thick dash-dot-dash trace shows the effects of applying an additional negative back gate bias, shifting the hole bands up 2 meV, as would occur within the high carrier density regime. Band offsets were taken from [25]. The bottom of the uncoupled InAs band is set as zero energy.

become available for scattering, increasing the number of scattering paths available, and thus decreasing the mobility. In the low carrier density regime, no such process exists, and so the mobility does not follow this trend with increasing temperature.

As an increasingly more positive top gate bias is applied, we enter the high carrier density regime, where the second excited electron-like subband is visible in the SdH oscillations. At this point, the energy of the second electron-like subband has been forced down sufficiently to cross the Fermi energy, as in Fig 6.24, where the electron-like bands have been shifted down 100 meV. Note that the solid lines in Fig. 6.24 correspond to the solid lines in Figs. 6.22 and 6.23.

We know that, in this regime, that the  $B_{||} = 0$  sheet resistance maximum in the in-

plane magnetoresistance disappears, and that the Hall mobilities acquire a dependence on the relative top and back gate biases. Fig. 6.24a shows that the states at the Fermi energy in the first and second electron-like subbands now both follow the dispersion of uncoupled electron bands in this regime.

Due to the  $q$  dependence of the second term within equation 6.4, it is much easier to shift the hole-like dispersions within the GaSb layer (with a charge of  $+e$ ) with respect to the electron-like dispersions within the InAs layer (with a charge of  $-e$ ), when compared to shifting two electron-like dispersions relative to one-another [35, 41]. Specifically, it has been found that in-plane fields as high as 11 T are needed to suppress scattering between two subbands arising from the same quantum well [129, 130], whereas fields of 3 T are enough to significantly shift the InAs dispersion with respect to the GaSb dispersion [16, 35, 41] in coupled quantum well structures. As such, the effect of an in-plane magnetic field on the 2D Fermi surface will be diminished in the high carrier density limit, resulting in the disappearance of the  $B_{\parallel} = 0$  maximum as a high positive top gate voltages are applied.

Applying a gate bias to the GaSb layer, will then shift the energy of the uncoupled hole bands. As we do so, we will shift the anticrossing point (in energy and in  $k$ ) between the heavy hole band (H1) and both the first (E1) and second (E2) electron-like subbands, as in Fig. 6.22. This will have two effects. Firstly, it will be easier to populate the second electron-like subband as we apply a more positive top gate bias. Such a bias will shift the uncoupled hole bands down in energy, and so will also shift the anticrossing point between the highest heavy hole subband and the second electron-like subband down in energy. However, the size of the anticrossing gap is fixed by the level of electron-light hole coupling [4, 25], and so, if the anticrossing point is shifted down in energy, a smaller top gate bias (and thus a smaller carrier density) will be needed to enter the high carrier density regime. We can see this effect in Figs 6.2b and 6.18.

Secondly, by shifting the anticrossing point between the second electron-like (E2) and heavy hole (H1) subbands, the proportion of states within the second electron-like subband that follow a hole-like dispersion can be altered, which will change the effective mass of the E2 subband. In Fig. 6.24b the effect of applying a negative gate bias to the GaSb layers is illustrated. Such a bias moves the dispersion of the uncoupled hole bands higher in energy and as such, increases the contribution the heavy hole subband makes to the dispersion of the second electron-like subband. By including more states

with a hole-like dispersion, and as such with a large effective mass [21], in this second electron-like subband, the mobility of that electron-like subband will decrease. This explains the trend observed in Figs 6.2b and 6.18, where a more negative back gate bias results in a lower Hall mobility for comparable carrier densities.

## 6.9 Conclusions and Further Work

We have investigated the scattering within gated InAs/GaSb coupled quantum well heterostructures through magnetotransport measurements within the electron dominated regime.

We find that the scattering within this class of quantum well can be described by three regimes: at low, intermediate and high carrier densities. In all three regimes, the temperature dependence of the Hall mobility indicates that the scattering is dominated by remote impurities until phonon mediated scattering starts to dominate at higher temperatures ( $T \geq 50$  K).

The low carrier density regime shows scattering similar to a single 2DEG, with the Hall mobility showing a power law dependence on the Hall carrier density, indicative of the screening provided by the electron cloud against impurities far removed from the transport channel. It is worth noting that, in this regime, the Hall mobility is independent of the relative top and back gate biases, and instead is reliant entirely on the total carrier density. We find that application of a back gate bias modulates the Hall carrier density and the carrier density extracted from the Fourier transform of the SdH oscillations equally. This shows that a back gate bias modulates electron-like states within the coupled quantum well.

We conclude that, in the low carrier density regime if we bias the back gate, we shift the GaSb dispersion relation in energy, and as such we also shift the anticrossing point between the heavy hole-like states and the electron-like states in both energy and  $k$ , as shown in Fig. 6.22. As we do so, we change the number of states in the conduction band, altering the observed, electron-like carrier density. This shows that for these carrier densities, it is the relative energies of the InAs conduction bands and GaSb valence bands that are important to transport, and the back gate does not act as a separate gate on the InAs layer itself [12].

In the intermediate carrier density region, the mobility deviates from the trend seen at low carrier densities, which is explained by the appearance of new states near the

Fermi energy, as seen in investigations of the in-plane magnetoresistance, displayed in Fig. 6.17. As we increase the carrier density through this regime, we note that the Hall mobility reaches a maximum and then proceeds to drop dramatically, which is accompanied by a rise in the quantum lifetime, and a change in the effective mass of the system. The behaviour of the Hall mobility and quantum lifetime are most often associated with the appearance of a higher order subband, but the second excited electronic subband does not appear to contribute to transport until a higher carrier density is reached.

We infer that the mobility peak is due to hybridisation between the second electron-like subband and the highest heavy-hole subband. The mobility peak does not shift with the relative applied front and back gate biases, and therefore this feature must be due, at least in part, to electron-hole hybridisation. As we apply a gate bias (top or back), and move the uncoupled energies of the highest energy heavy-hole subband and the second electron-like subband into alignment, a new anticrossing gap will open between these two bands, as in Fig. 6.23. This will mean that the second electron-like subband will not become occupied until a higher energy, as it must first overcome this anticrossing gap.

The first states to become populated within this new, hybridised, subband will be states with a heavy-hole like dispersion at  $k = 0$  [4, 30]. These states will have a high effective mass, and as such a low mobility. Therefore these new states will not be detected by traditional SdH measurements at the fields studied here. Due to their low mobility, very few of these states will need to be populated to have a large effect on the Hall mobility.

As we increase the carrier density further, a second electronic subband eventually becomes populated, showing SdH oscillations that can no longer be described by a single envelope function. At this point, we infer that the energy of the second, electron-like subband has moved sufficiently down in energy that the Fermi energy now is above some of the unhybridised states at a finite  $k$ , as in Fig. 6.24a.

In the high carrier density regime, the relative magnitude of the electric fields provided by the top and back gates becomes relevant to the electronic transport, as shown in Fig. 6.18. We reason that this gate dependence is due to a similar shift in anticrossing observed in the low carrier density regime. As we shift the energies of the hole-like subbands higher in energy, a greater proportion of the second electron-

like subband dispersion relation will look like a heavy-hole band [30], decreasing the mobility of that subband, and thus the system as a whole.

We note that a similar feature has been observed by Nguyen et al. [9] on a coupled InAs/GaSb quantum well. In that study, the carrier density is modulated with an applied back gate bias. However, the quantum well studied there is formed of a 12.5 nm thick InAs layer grown in direct contact with a 5 nm thick GaSb layer (compared with 15/8 nm InAs/GaSb in our case). They observe two separate peaks in mobility, one at a carrier density of  $\approx 14 \times 10^{11} \text{ cm}^{-2}$  and another at  $\approx 24 \times 10^{11} \text{ cm}^{-2}$ . We reason that the peak in mobility at the lower carrier density is due to the additional anticrossing discussed here, whilst the peak at the higher carrier density is due to the population of a second excited electron subband, as stated in the paper.

This chapter has explored the dependence of the magnetotransport through the electron dominated regime in InAs/GaSb coupled quantum well structures, by considering the formation of hybridised states between both the first and second electron-like subbands, and the highest energy heavy hole subband. Further work would allow this hybridisation to be explored in detail, possibly through limiting the quantum well coupling by inserting an inter-well AlSb barrier [44, 61], or including impurity states at the InAs/GaSb interface [74].

---

# CHAPTER 7

---

Spin-Orbit Coupling in InAs/GaSb  
Heterostructures Away from Charge Neutrality

In an ideal 2DTI material, we would only consider the spin-orbit coupling (SOC) arising from the nuclear electric field. This would cause the spin-filtered edge states to be polarised exclusively out of the device plane [6]. However, the stack structure of InAs/GaSb coupled quantum wells is inherently asymmetric, giving rise to a new electric field. Additionally, the zinc-blende crystal structure existing throughout the InAs/GaSb heterostructure also lacks a centre of inversion symmetry, resulting in yet another electric field. The electric fields arising from these asymmetries result in the Rashba and Dresselhaus spin-orbit couplings respectively [27]. While these additional sources of SOC do not break time reversal symmetry (and so should not disrupt the topological nature of the transport through this state [5]), additional SOC terms can cause the spin-polarisation axis of the 2DTI edge states to be tilted into the plane of the device, or for this polarisation axis to become  $k$ -dependent [19, 20]. Therefore, this chapter deals with the SOC within two separate InAs/GaSb coupled quantum wells far from charge neutrality. The purpose of this study is to determine the magnitude of the Rashba and Dresselhaus SOC terms, and how the SOC within this material changes with an applied gate bias or with small changes in the quantum well growth conditions.

Here we show the relative magnitudes of the Dresselhaus and  $k$ -linear Rashba SOC terms in an InAs/GaSb 2DTI candidate in both the single and double carrier regime, showing that not only is the Dresselhaus parameter constant across all top gate bias conditions, as expected, but it is also robust against small changes in growth conditions. Additionally, the much larger Rashba parameter increases as we deplete carriers from the active region, implying that an internal potential gradient caused by the stack structure is instrumental to the SOC observed.

The work in this chapter has been published in Physical review B [136], and presented in poster format at ICPS 2018.

## 7.1 Sample Details

Using optical lithography and wet etching techniques discussed in chapter 3, the coupled quantum wells G0156 and G0153 were patterned into top-gated, right angled Hall bars with a separation of 250  $\mu\text{m}$  between the probe arms. Both of these quantum wells were grown on  $n^+$  GaAs substrates, and both of these quantum wells are composed of a 15 nm thick InAs layer on top of a 8 nm thick GaSb layer, sandwiched between two 50 nm thick AlSb barriers. However, wafer G0156 was grown at a slightly higher As

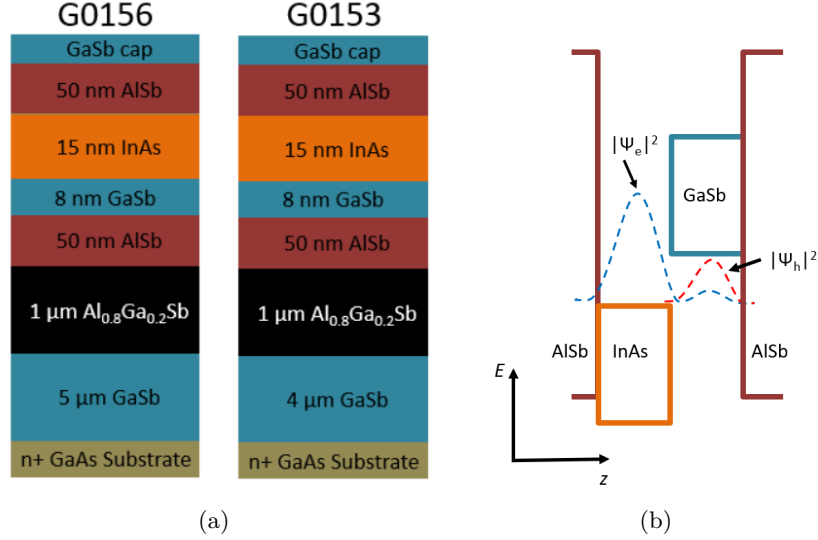


Figure 7.1: Fig. 7.1a shows the stack structures studied within this chapter. A schematic band alignment for this structure is shown in Fig. 7.1b, where the distributions of the electrons (blue dashed line,  $|\Psi_e|^2$ ) and heavy holes (red dashed line,  $|\Psi_h|^2$ ) at  $k_{\parallel} = 0$  are also highlighted, following [25]

over-pressure ( $4.6 \times 10^{-6}$  mbar for G0156 compared with  $3.35 \times 10^{-6}$  mbar for G0153). The layer structure for both of these coupled quantum wells is shown in Fig. 7.1.

A summary of the zero gate bias transport parameters is presented in Table 7.1. The effective mass was calculated from the temperature dependence of the SdH oscillations [105] up to 10 K with up to 2.5 T magnetic field applied out of the plane of the device. The carrier density and Hall mobility were calculated at 1.5 K using up to 0.2 T magnetic field applied out of the device plane. In all cases, the measurements were performed using standard lock-in amplifier techniques with a source-drain bias current of 1  $\mu\text{A}$ .

Hall resistance data up to 8 T applied magnetic field for both G0153 and G0156 at 1.5 K and with zero applied top gate bias is shown in Fig. 7.2. We can see that the Hall resistance in G0153 shows a slight bending of the Hall trace at applied magnetic fields of less than 1 T, as well as the appearance of plateaux in the Hall resistance at values that would indicate an odd filling factor at intermediate fields. Additionally, the high field plateaux do not occur at the expected magnetic field. This behaviour is not present in

## 7.2 Observation of Spin-Orbit coupling in InAs/GaSb heterostructures

Wafer	Carrier Density ( $\times 10^{11} \text{cm}^{-2}$ )	Hall Mobility ( $\text{cm}^2 \text{V}^{-1} \text{s}^{-1}$ )	Effective Mass ( $m_0$ )
G0153	$17.6 \pm 0.2$	$137,000 \pm 1000$	$0.032 \pm 0.005$
G0156	$17.5 \pm 0.2$	$111,000 \pm 1000$	$0.040 \pm 0.005$

Table 7.1: Table of zero gate bias transport properties for the two wafers studied in this chapter. The Hall measurements were taken at 1.5 K, and the effective mass measurement was derived from the temperature dependence of the SdH oscillations up to 10 K. For these measurements, current was applied down the [100] axis. Effective mass is quoted in units of the free electron rest mass.

G0156, neither is it present at any top gate bias in G0156. We take this to indicate that the transport in G0156 is due to a single carrier gas at the gate biases investigated in this chapter, whereas the transport in G0153 contains a significant contribution from a hole gas localised within the GaSb layer that is de-coupled from the majority of the transport [61]. Despite this, both wafers show transport that is dominated by electrons at all biases investigated here, as shown by the sign of the ordinary Hall co-efficient.

However, we note that the SdH oscillations within both of these wafers (shown below in Fig. 7.3) are contained in a single envelope function with a unified temperature dependence up to 10 K, indicating that a single carrier species is responsible for the SdH oscillations. This, along with the calculated value of the effective mass being close to the expected effective mass for electrons in InAs quantum wells of  $(0.032 - 0.046) m_0$  [50, 106, 107], suggests that the magnetoresistance behaviour in these wafers arises due to a single electron-like subband at these temperatures.

## 7.2 Observation of Spin-Orbit coupling in InAs/GaSb heterostructures

In order to observe the SOC behaviour present and its dependence on applied top gate bias within these wafers, magnetoresistance measurements were performed at various gate biases. Data was collected by stepping the magnetic field between 8 T and 0 T, and sweeping the gate at each point. All measurements of the SOC were performed at 1.5 K. We found that when the applied gate bias in both wafers was increased

## 7.2 Observation of Spin-Orbit coupling in InAs/GaSb heterostructures

beyond  $\pm 1$  V, the observed SdH oscillations no longer returned to the as-cooled state shown in Fig. 7.3, instead producing SdH oscillations that were no longer enclosed in a single envelope function. This would indicate the presence of a second carrier gas, which possibly could have been excited by charge traps underneath the quantum well. However, we assume that we are only modulating the carrier density in the InAs layer nearer the top of the stack structure at biases below  $\pm 1$  V. Therefore, all other layers are screened from the electric field produced by the top gate at these voltages by the 2DEG localised within the InAs layer. If the structure was heated from 1.5 K to 300 K and subsequently cooled, the SdH oscillations returned to their original state, implying that the charge traps were allowed to discharge.

This was first attempted in G0156 when the current was applied along the [100] crystallographic axis. The observed SdH oscillations were then plotted as a function of inverse magnetic field, interpolated to get an even spacing between points, and a discrete Fourier transform analysed. An example of the SdH oscillations observed when  $-1$  V

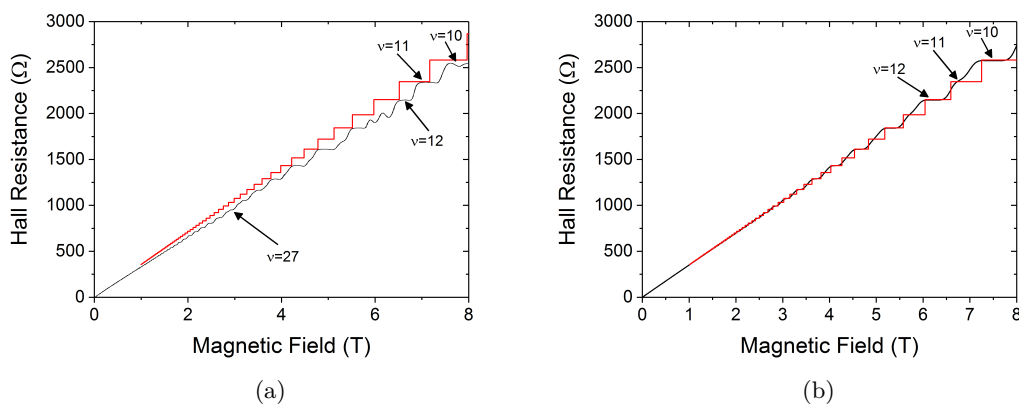


Figure 7.2: Hall resistance up to 8 T for wafers studied in this chapter. Fig. 7.2a shows the Hall resistance in G0153, whereas Fig. 7.2b shows the Hall resistance in G0156. In both cases, the measured data is displayed in black, with the expected 0 K plateaux positions from the low field (applied field  $< 0.2$  T) Hall measurements displayed in red. The  $\nu = 10$ , 11 and 12 plateaux are highlighted by arrows in both Fig 7.2a and 7.2b, along with an interesting odd-integer plateau at low magnetic field ( $\nu = 27$ ) in Fig. 7.2a, indicating the presence of a second carrier gas.

## 7.2 Observation of Spin-Orbit coupling in InAs/GaSb heterostructures

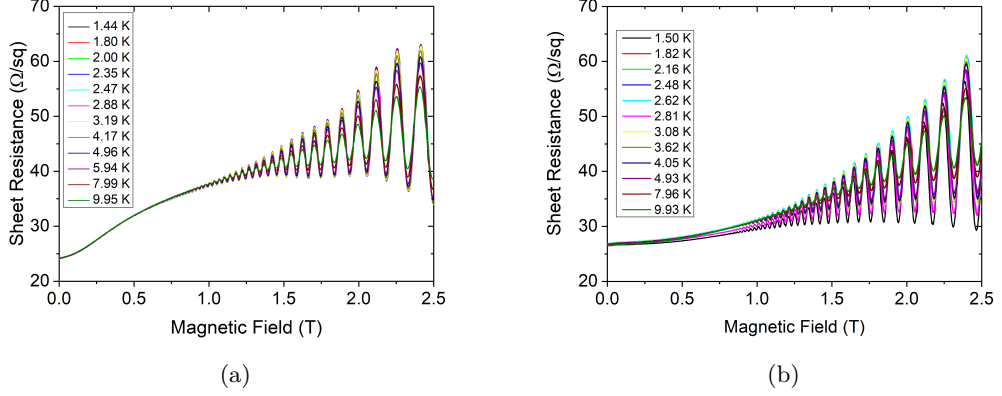


Figure 7.3: Magnetoresistance up to 2.5 T (in the absence of a gate bias) as a function of temperature up to 10 K, used to extract the effective mass for wafers studied in this chapter. Fig. 7.3a shows the magnetoresistance in wafer G0153, whereas Fig. 7.3b shows the magnetoresistance in wafer G0156.

top gate bias is applied is shown in Fig. 7.4a, with the related Fourier transform shown in Fig. 7.4b. At most gate biases, two significant peaks were observed in the Fourier spectrum. We equate both of those peaks to a spin-split carrier density, the higher of which is aligned to the spin-splitting field caused by the total SOC in the material [50, 51].

This measurement was then repeated on 3 more devices on G0156, where current is applied along the [010], [110] and  $[1\bar{1}0]$  crystallographic axes. All 4 of these measurements were repeated on 2 more sets of devices on G0156 to confirm that the observed effect was independent of fabrication conditions.

Since our SdH oscillations appear to be due to a single, spin-split, electron-like sub-band, they can be analysed with the following expression [50];

$$\Omega = \frac{(n^+ - n^-)h^2}{m^*} \sqrt{\frac{\pi}{2(n^+ + n^-) - 2(n^+ - n^-)}} \quad (7.1)$$

where  $\Omega$  is the total spin orbit coupling parameter,  $m^*$  is the effective mass and  $n^+$  and  $n^-$  are the carrier densities associated with the peaks aligned and anti-aligned to the total spin-splitting field, respectively.

Above a +0.2 V top gate bias, a new set of SdH oscillations appear that are not

### 7.3 Crystallographic Axis-Dependent Measurements of the Spin Orbit Coupling in G0156

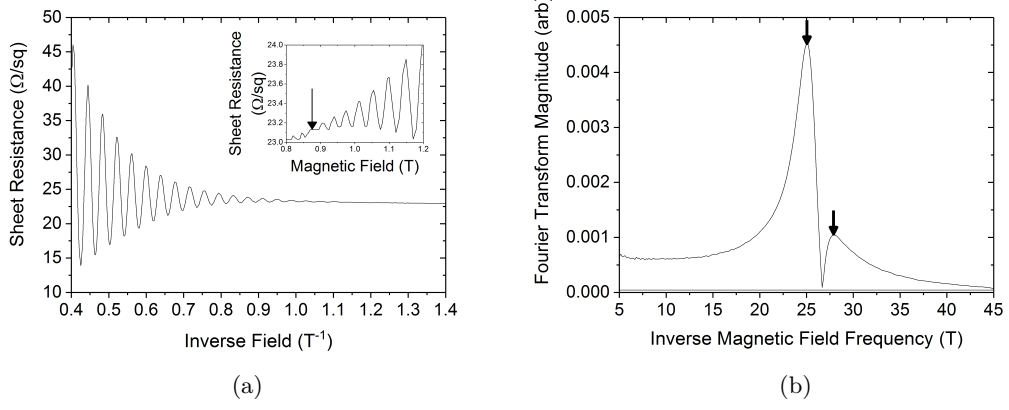


Figure 7.4: Fig. 7.4a SdH oscillations plotted as a function of inverse field used in the Fourier analysis at  $-1$  V applied top gate bias in G0156. A beating mode, indicating the two separate frequencies is highlighted in the inset. Fig. 7.4b is a discrete Fourier transform of Fig. 7.4a. The two frequencies, corresponding to the two spin-split carrier densities are highlighted with arrows.

contained within a single envelope function, along with a new peak in the Fourier spectrum. We take this to be indicative of occupation of a second occupied electron sub-band, and as such our model for spin orbit coupling is no longer valid after this point [51], as inter-subband scattering does not conserve spin. As we fill an excited level, inter-subband scattering will begin to play a significant part in the spin relaxation [137], masking the effect of the Rashba and Dresselhaus SOC. As such we neglect data taken at gate biases more positive than  $+0.2$  V in our analysis.

### 7.3 Crystallographic Axis-Dependent Measurements of the Spin Orbit Coupling in G0156

Figure 7.5 plots the total SOC parameter across the measured axes in G0156. We find that the total SOC parameter measured across the  $[100]$  and the  $[010]$  crystallographic axes are experimentally identical. This is expected, as the Dresselhaus spin-splitting field will be parallel to the current along these crystallographic axes [52]. Given this, we plot a single set of SOC parameters representing these two crystallographic axes. This

### 7.3 Crystallographic Axis-Dependent Measurements of the Spin Orbit Coupling in G0156

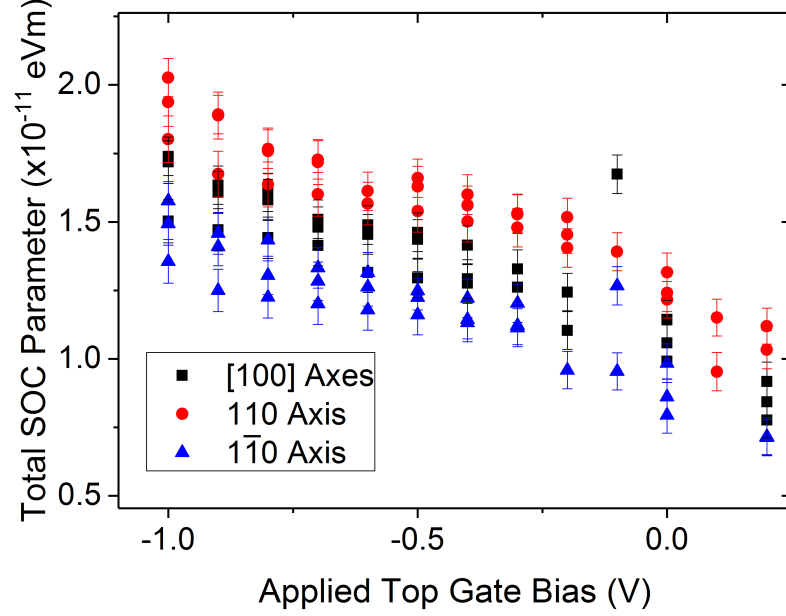


Figure 7.5: Total SOC parameters  $\Omega$  along the [100],[110] and  $[1\bar{1}0]$  axes as a function of applied top gate bias in wafer G0156.

is also an important check, as it shows that our fabricated devices are well aligned to the relevant crystallographic axes. If this was not the case, we would expect a significant difference between the [100] and the [010] crystallographic axes.

From Fig. 7.5, we notice that the total SOC parameter increases as the top gate voltage is made more negative for measurements along all crystallographic axes. While there is a small increase in the difference between the carrier densities associated with the spin-orbit field aligned and anti-aligned peaks (i.e.  $n^+ - n^-$ ) in the discrete Fourier transformed SdH oscillations as the top gate voltage becomes more negative, the main reason for this trend appears to be the drop in carrier density associated with depletion of electrons from the InAs layer. This would signify that a greater proportion of the electrons become aligned with the total SOC field as the top gate voltage becomes more negative.

We interpret this increase in the total SOC parameter with more negative gate biases by reasoning that the asymmetry present in the stack structure will add some

### 7.3 Crystallographic Axis-Dependent Measurements of the Spin Orbit Coupling in G0156

---

built-in electric field [51, 138] that will contribute to all orders of the Rashba spin orbit coupling [52, 139, 140]. Specifically, as the intrinsically n-type InAs layer is grown on top of the intrinsically p-type GaSb layer [3], a potential gradient will be formed across the active layers within the quantum well. Applying a negative gate voltage will introduce an external electric field, that will act in tandem with this internal electric field, resulting in the observed behaviour.

This behaviour has also been observed in coupled quantum wells with similar stack structures, but with the action of both top and back gates by Beukman et. al. [38], through which they are able to obtain a constant carrier density while changing the internal bias conditions. They find that when a more negative top gate bias is applied, the Rashba SOC increases, even if the carrier density is kept constant. Interestingly, they also find that the Rashba SOC seems robust against the electric field applied from a back gate in their electron-dominated region. This is possibly due to the electric field from the back gate being screened by a hole gas present in the GaSb layer, and so the electron gas responsible for the SdH oscillations, and therefore the observed SOC, extracted in that body of work is unaffected.

The electric field responsible for the Rashba spin orbit coupling will always lie along the growth direction or in the direction of the applied electric field. Thus, in top gated devices grown along the [001] crystallographic axis, such as the ones discussed here, the spin-splitting field will always be perpendicular to the current. Due to this alignment, the spin-splitting caused by the Rashba SOC will have a constant magnitude across all crystallographic axes. However, as the crystalline asymmetry, and therefore the electric field that gives rise to the Dresselhaus SOC, is dependent on the crystal structure, the spin splitting field experienced by the current carrying electrons will vary from axis to axis in this case. This angular dependence can thus be used to separate the angle invariant Rashba SOC from the crystal axis dependent Dresselhaus SOC [27, 52]. A schematic diagram of this axial dependence is shown in Fig. 7.6.

Thus, the crystallographic axis dependence observed in Fig. 7.5 fits with our expectations. We expect the [110] crystallographic axis to have an elevated SOC parameter when compared to the [100] and [010] axes, as the Dresselhaus SOC will make an additive contribution to the total SOC. The reverse will also be true when the current is applied down the  $[1\bar{1}0]$  crystallographic axis, where the Dresselhaus will have a subtractive effect. By using this angular dependence, we can deconvolute the Rashba and

### 7.3 Crystallographic Axis-Dependent Measurements of the Spin Orbit Coupling in G0156

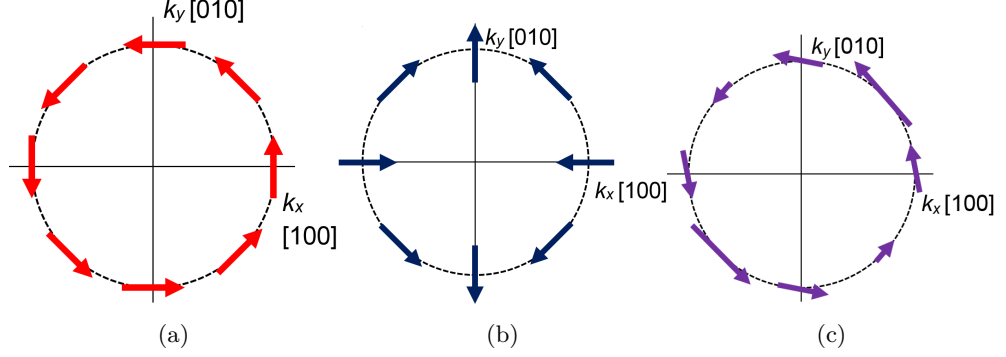


Figure 7.6: Schematic diagrams of the 2D Fermi-surface, showing the relative orientations of the effective SOC magnetic field in a quantum well grown along the [001] axis. Fig 7.6a shows the orientation of the effective magnetic field arising from Rashba SOC, while Fig 7.6b shows same information for the Dresselhaus SOC. Fig 7.6c shows the total magnetic field due to SOC experienced in this class of quantum well, where the length of arrow is proportional to the strength of the spin-splitting experienced by the carriers. Here, we assume that the Rashba term makes a dominant contribution to the SOC.

Dresselhaus SOC from the total SOC parameter,  $\Omega$ , with the following equation [52];

$$\Omega = \sqrt{\alpha^2 + \beta^2 + 2\alpha\beta \cos(2\theta)} \quad (7.2)$$

where  $\alpha$  and  $\beta$  are the SOC parameters associated with the Rashba and Dresselhaus SOC, respectively, and  $\theta$  is the angle between the crystallographic axis the current is applied down and the [110] axis. This fit, for the case of zero applied top gate bias is shown in Fig. 7.7a. As the [100] and [010] axes are experimentally identical, we are confident that the values of  $\Omega$  that we see across the [110] and  $[1\bar{1}0]$  axes are the maximum and minimum values for  $\Omega$ , respectively, due to the  $\cos(2\theta)$  term present in in equation 7.2.

A plot of the two contributions to the total SOC extracted by this method is shown in Fig. 7.7 as a function of top gate bias. As we expect, not only does the extracted Rashba parameter align well with the total SOC observed for the [100] and [010] axes, where we would expect the contribution from the Dresselhaus SOC to be negligible [52], but it also contains all gate dependence of the total SOC parameter that we observe across all axes.

### 7.3 Crystallographic Axis-Dependent Measurements of the Spin Orbit Coupling in G0156

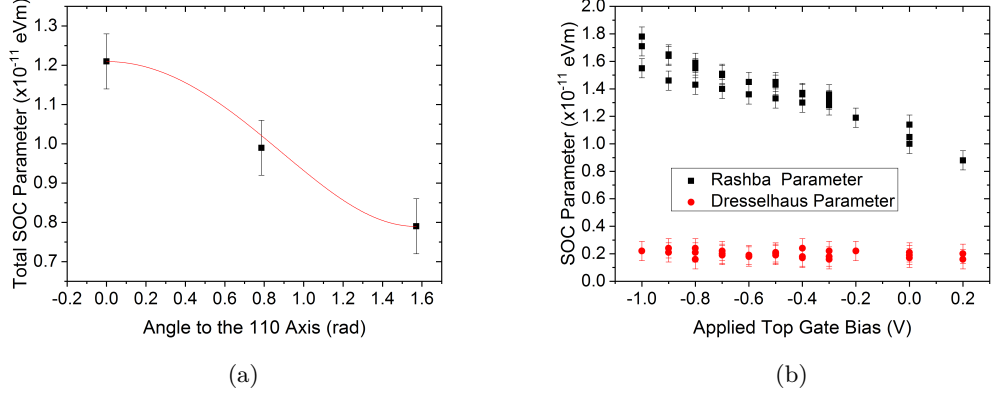


Figure 7.7: Fig. 7.7a shows the total SOC parameter at zero top gate voltage in G0156, plotted as a function of angle to the [110] axis, showing the expected  $\cos(2\theta)$  dependence. The fit to equation 7.2 is shown in red. Fig. 7.7b shows the Rashba and Dresselhaus parameters found from fitting equation 7.2 to the relevant data in Fig.7.5.

We find the Dresselhaus SOC parameter to be  $(0.20 \pm 0.07) \times 10^{-11}$  eVm across all applied gate biases. At 0 V applied bias this would result in a Dresselhaus spin splitting energy of  $(1.30 \pm 0.5)$  meV [138]. Interestingly, this aligns well with the predicted value of the splitting due to bulk-inversion asymmetry in HgTe quantum wells [71] and InAs/GaSb coupled quantum wells [115] of 1.6 meV.

The Rashba parameter was calculated to vary between  $(0.88 \pm 0.07) \times 10^{-11}$  eVm at 0.2 V applied top gate bias and  $(1.78 \pm 0.07) \times 10^{-11}$  eVm at  $-1.0$  V applied bias. This is significant, as typical measurements on InAs quantum wells with a doped underlayer (to supply the structural inversion asymmetry needed for the Rashba SOC), place the maximum measured Rashba parameter to be approximately  $1 \times 10^{-11}$  eVm [52, 138]. We reason that the presence of a GaSb layer integrated into the active portion of the quantum well will induce a greater asymmetry term within the quantum well when compared to dopants remote to the transport channel.

## 7.4 Effects of Growth Conditions on Spin-Orbit Coupling within InAs/GaSb Heterostructures

---

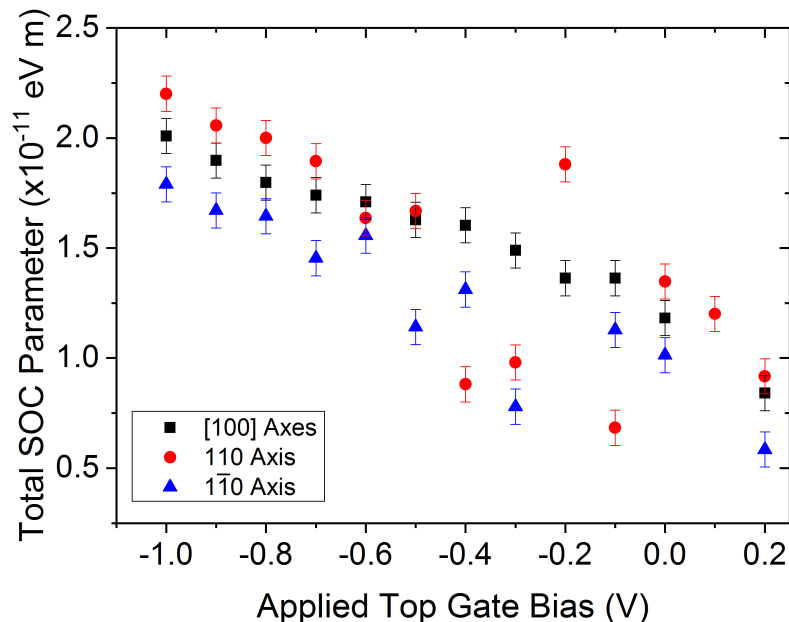


Figure 7.8: Collection of total SOC parameters  $\Omega$  along the [100], [110] and [1 $\bar{1}$ 0] axes as a function of applied top gate bias in wafer G0153.

## 7.4 Effects of Growth Conditions on Spin-Orbit Coupling within InAs/GaSb Heterostructures

These measurements were then repeated on a set of devices grown on G0153, a nominally identical wafer, where the hole gas localised in the GaSb layer in the quantum well plays a significant part in the zero top gate bias transport. It is worth noting that, although both an electron gas and a hole gas play a significant part in the transport, the transport is still heavily electron-dominated. This is drawn from the sign of the Hall coefficient and the fact that the total SdH carrier density is similar to the low field ( $< 0.2$  T) Hall carrier density. We therefore neglect the influence of electron-hole scattering [141, 142] and topological effects on the spin-dynamics of this heterostructure. The results of this study are shown in Fig. 7.8.

We note that the scatter of the total SOC parameters measured along the [110] and [1 $\bar{1}$ 0] axes for intermediate gate biases ( $-0.1$  V to  $-0.6$  V) is much larger for G0153

## 7.4 Effects of Growth Conditions on Spin-Orbit Coupling within InAs/GaSb Heterostructures

---

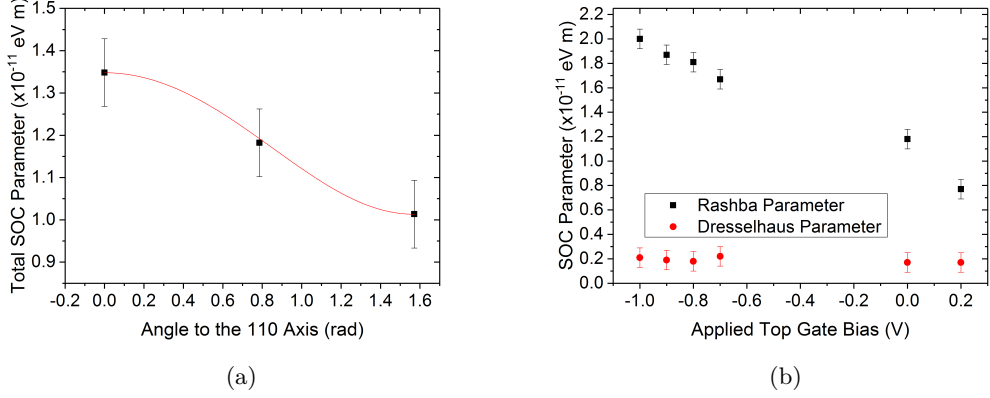


Figure 7.9: Fig. 7.9a, total SOC parameter at zero gate bias in G0153, plotted as a function of angle to the [110] axis. The fit to equation 7.2 is shown in red. Fig. 7.9b, Rashba and Dresselhaus parameters found from fitting equation 7.2 to the relevant data in Fig.7.8.

than it is for G0156. This results in non-physical solutions to equation 7.2 and as such we neglect those points from further analysis. It is unclear why this is the case, as the SOC parameters measured along the [100] and [010] axes follow a trend similar to that seen in G0156, and track with the calculated Rashba parameters shown in Fig. 7.9b.

Despite the lower effective mass in wafer G0153 (as shown in Table 7.1), we can see from Fig. 7.9b that the Dresselhaus parameter is identical to the single carrier case, measured at  $(0.20 \pm 0.08) \times 10^{-11}$  eVm across all applied top gate biases. As such, we can infer that small changes in the crystallographic properties of the quantum well do not change the potential gradient that gives rise to the Dresselhaus SOC. However, since the wafers studied here were grown so that the InAs layers were terminated with InSb-like surfaces [22], other contributions to the Dresselhaus SOC, such as the crystalline asymmetries at the interface, have not been studied here.

On the other hand we note that the Rashba parameter is elevated at all negative top gate biases in wafer G0153, when compared to similar gate biases in wafer G0156. We interpret this increase by reasoning that a more highly charged GaSb layer will induce a greater potential gradient across the quantum well, and so result in a greater contribution to the Rashba SOC.

## 7.5 Conclusions and Further Work

We have investigated the SOC within InAs/GaSb coupled quantum wells along different crystallographic axes in both the single and double carrier, electron dominated regimes, and explicitly deconvoluted the Rashba and Dresselhaus terms as a function of gate bias.

We find that the  $k$ -linear Rashba SOC is sensitive to top gate bias conditions and the precise heterostructure growth. We determine values for the Rashba parameter varying between  $(0.88 \pm 0.07) \times 10^{-11}$  eVm at 0.2 V applied top gate bias and  $(1.78 \pm 0.07) \times 10^{-11}$  eVm at  $-1.0$  V applied bias, respectively, in Wafer G0156, and  $(0.77 \pm 0.08) \times 10^{-11}$  eVm and  $(2.00 \pm 0.08) \times 10^{-11}$  eVm at similar top gate biases in Wafer G0153.

In contrast, the Dresselhaus SOC is constant across all top gate biases. In addition, it appears insensitive to small variations in in sample properties arising from changes in the growth conditions of the InAs layer, as our value of  $(0.20 \pm 0.07) \times 10^{-11}$  eVm in the single carrier regime aligns well with our measurements in the double carrier regime, where we find a Dresselhaus parameter of  $(0.20 \pm 0.08) \times 10^{-11}$  eVm. Our data also agrees well with recent measurements by Beukman et al [38], who determined the Dresselhaus parameter as  $0.28 \times 10^{-11}$  eVm.

A challenge in current semiconductor spintronics is to obtain a device in which the Rashba and Dresselhaus SOC's are of equal magnitude. Once this condition is met, certain crystallographic axes should display an absence of spin-relaxation [143], allowing novel devices such as a non-ballistic spin-field effect transistor to be fabricated [144]. The samples measured here show a maximum Rashba to Dresselhaus ratio of  $3 \pm 1$ . It is possible, either by further modifying the Rashba parameter through additional changes in the growth conditions or by modifying the nature of the interface [145], that InAs/GaSb coupled quantum wells could become an interesting platform to develop such non-ballistic spin devices.

We note that we have not studied the SOC close to the hybridisation gap, where topological behaviour will begin to have a significant effect on transport. However, the technique discussed here may not then be applicable owing to the low electron-like carrier density as the hybridisation gap is approached and the resonant behaviour of the sample resistance within a gapped regime. In addition, due to the comparable carrier densities of electrons and holes within the heterostructure as the topologically

interesting region is approached, additional spin relaxation mechanisms are expected to be apparent, such as Bir Aronov Pikus (BAP) scattering [141, 142]. BAP scattering arises due to exchange interactions between electrons and unpolarised holes (or polarised heavy holes and unpolarised light holes [146]) which will allow particles to undergo spin relaxation on a much shorter time-scale, which would mask the Rashba and Dresselhaus SOC contributions.

To compound this, due to the number of defects introduced by methods used to screen bulk conduction from the QSHE regime [39, 74], Elliott-Yafet scattering may also play a part in the spin-scattering close to the hybridisation gap. Interactions between current carrying electrons and impurity sites can cause spin-relaxation [147, 148], where scattering off an impurity band can cause a spin-flip.

Future studies in this regime would, however, provide fascinating insights into the nature of the topological state seen in this class of material. Furthermore, the internal electric fields within the material could be engineered, e.g. by swapping positions of the active InAs and GaSb layers, changing quantum well thicknesses, or adjusting their carrier densities, enabling tailoring of spin-orbit coupling in the topological regime.

---

# CHAPTER 8

---

Conclusions and Outlook

The interest in QSHE systems has rekindled research into InAs/GaSb coupled quantum wells. The band inversion provided by electron-hole anticrossing leads to the existence of gap-closing states which protected by the symmetries of the system. However, recent research efforts have focused on the properties of the gapped regime, with the properties of the electron-dominated regime being somewhat neglected. This thesis set out to probe the properties of this regime and determine how this electron dominated regime is distinct from a single InAs quantum well. The main results gained from this study, and the way in which they could impact future 2DTI research is summarised here.

## 8.1 Conclusions

The work in this thesis has focused on the characterisation of InAs/GaSb coupled quantum wells away from charge neutrality, in order to understand the properties of this interesting coupled system as it is tuned into a 2DTI state. Wafers received from several different MBE systems were fabricated into double gated Hall bars by the processes outlined in chapter 3.

Chapter 5 deals with the as-cooled properties of two coupled wells, one of which has a 2.5 nm AlSb spacer inserted between the two quantum well layers. We find that when the wells are in intimate contact, the transport is analogous to a conventional 2DEG with SdH oscillations arising from a single envelope function and well quantised IQHE behaviour. It is only when the coupling between the two wells is disrupted, either by changing the stoichiometry of the quantum well (by altering the growth conditions as in chapter 7), or by inserting an AlSb barrier between the two wells (as in chapter 5) that the quantum wells show two-carrier transport in the absence of an applied gate bias. Additionally, only the system with the disrupted inter-layer coupling shows SdH oscillations that arise from this second carrier gas.

From temperature dependent analysis of the SdH oscillations within these two coupled quantum wells, it was found that the carriers in the strongly coupled well (without the inter-layer AlSb barrier) were electrons with an effective mass analogous to that in a single InAs quantum well. If similar analysis is performed on the quantum well with the inter-layer AlSb barrier, we find two carrier species, one with an enhanced effective mass and one with an effective mass similar to that of hole-states within GaSb. This second carrier was only visible at the highest magnetic fields and the lowest temperatures. We therefore conclude that, by increasing the separation between the two

quantum wells, we close the hybridisation gap present in the strongly coupled case. By reducing the magnitude of this hybridisation gap, we can start to observe states arising from hole bands, which are broadened by scattering. In the case of strong coupling, the broadening of the states by scattering is smaller than the hybridisation gap, and so these states aren't observed in our transport data.

This analysis, for the strongly coupled quantum wells, is then expanded on in chapter 6. By applying a gate bias to the coupled well and considering the in-plane magnetoresistance and the quantum lifetime, it was found that a new set of states exist near the Fermi energy, even before a second, electron-like subband can be seen in the SdH oscillations. Additionally, the Hall mobility in this system is independent of the relative top and back gate biases, until this second electron-like subband can be detected (in the SdH oscillations). At that point, a more negative back gate bias results in a lower Hall mobility for a similar carrier density. Therefore, we conclude that, even in the heavily electron dominated regime studied in this thesis, the back gate acting on the GaSb layer shifts the energies of the GaSb bands and the anticrossing point (in energy and in  $k$ ) between the electron-like and hole-like bands. This is contrary to previous assumptions, where it was stated that the back gate acts as an additional gate on the InAs layer, as no hole-like transport is detected within this electron-dominated regime [12]. The new states that we see near the Fermi energy would then be attributed to electron-like states travelling through a hole-like dispersion, created by the second electron-like subband anticrossing with the highest energy heavy-hole subband.

Finally, we probed the SOC within this class of coupled quantum well in chapter 7. We find that the Dresselhaus SOC within this class of material is constant with respect to the applied top gate bias, and independent of small changes in the growth conditions. However, the Rashba SOC can be easily controlled by an applied top gate bias with a more negative bias resulting in a stronger SOC. Additionally, a small change in growth conditions led to a hole gas decoupling from the transport within the quantum well. In this two carrier case, a larger Rashba component was observed, showing that the internal electric fields, created by the structural inversion symmetry, are critical to the SOC observed in these coupled quantum wells. It is worth noting that the Rashba SOC observed here is much greater than that found in similar measurements performed on single InAs quantum wells [50, 52], showing that the structural inversion symmetry is much enhanced by integrating the p-type GaSb layer into the quantum well, rather

than having the structural inversion asymmetry supplied by a remote doping layer.

## 8.2 Outlook and Further Work

We note that, throughout our research, we were unable to reliably tune the system into the topologically non-trivial hybridisation gap. In the immediate future, new coupled quantum wells, perhaps with reduced well widths, could be grown to reduce the as-cooled carrier density. This would make reaching a charge neutral regime easier, and allow us to probe the topologically protected edge states observed within this class of material. One topic of study, once these new coupled quantum wells are obtained, would be the inter-layer Si doping used to localise mid-gap states and thereby increase the resistance of the gapped regime [13, 74]. We have established that, by physically separating the quantum well layers, we can reduce the size of the hybridisation gap in energy. Theoretically there should be some optimal doping level where the electron-hole hybridisation is not significantly impeded, but the mid-gap states are well localised.

Once a 2DTI state has been experimentally verified, a natural experiment may be to test the limits of the quantised conductance in the presence of inter-edge tunnelling. Most measurements on these topological materials are on Hall-bar devices with widths of several micrometers to minimise this tunnelling, but no study as of yet exists to examine this effect. Ortiz et. al [19] predicted that the strong SOC within these materials and the “generic helical edge modes” created by the SOC would create a gap in the edge state dispersion in ribbons of 2DTI material  $\approx 200$  nm wide. Creating devices on this scale may require dry etching techniques not explored in chapter 3 [89], but should be well within the realms of possibility. Such a study would be vital if 2DTI devices were to be realised.

The topological excitonic insulator phase discussed by Du et al. is also of interest [10, 13]. Specifically, it appears as if this state is extremely robust against the application of a magnetic field. In fact it has been noted that the quantised nature of the conductance persists to 35 T in-plane field [10] or 2 T applied out of plane field [13]. This is extremely odd, as similar measurements on HgTe quantum wells show that the quantised conductance is destroyed by application of an out of plane magnetic field of less than 0.05 T [76]. Therefore a detailed, systematic study of the quantised conductance with respect to out of plane magnetic field would be useful.

Particularly interesting would be the effects of a gate voltage on the magnetic field-

induced breakdown of the quantised resistance. It has been noted on multiple occasions [10, 13, 92, 149] that as the system is tuned into the inverted regime, the resistance plateaus at the quantised value. This can be understood by reasoning that any mid-gap state should contain transport dominated by the gap closing edge modes. However, a potential excitonic state should be particle-hole symmetric [78], and so should be independent of the position of the Fermi energy within the gap. If modulating that Fermi energy, with an applied gate bias, changes the magnetic field necessary to disrupt the quantised conduction through this QSHE state, it could reveal some fascinating insights into the nature of the quantised conduction seen within these coupled quantum wells.

Spin injection into a QSHE material would also be of fundamental physical interest. Not only would this result in the potential observation of the quantised spin-Hall voltage predicted in this state, it has been predicted that, by selectively modulating one edge state, the total spin carried by a 2DTI can be canted [7]. This opens the door for a potential QSHE-transistor structure where spins can be selectively passed through the device based on the bias applied to the modulated edge.

Finally, even if the 2DTI phase within this material remains elusive, InAs/GaSb superlattices have been used extensively for their useful optical transitions. In fact, the tunable intersubband transition studied in chapter 6 could result in an efficient THz lasing structure, depending on the size of the second electron-like subband-hole hybridisation gap [150].

---

# APPENDIX A

---

Device Fabrication Recipe

---

A large part of the cleanroom work outlined in this thesis was based around trying to replicate rival group's device processes, which are not widely reported in the literature. As such, this recipe attempts to be as detailed as possible, in order to provide the stepping stone that I wish I had at the start of my PhD.

Of particular concern to anyone wishing to follow this recipe is the mesa etch time and the flood expose of the PMMA/S1813 bi-layer. The etch time for a 100 nm deep etch was found to vary between 10 and 20 minutes, depending on the wafer. It is unclear why this is the case, but since our material was at a premium, no systematic study on this was undertaken. Secondly, as stated in chapter 3, a UVO cleaner is not an optimal DUV source, and so the 30 minute exposure stated here is gross overkill if a dedicated DUV flood source is available.

#### 1. Mesa Etch

- (a) Make Etchant. N.B.: The etchant can be made directly before etching the sample, but due to the elevated temperature needed to dissolve the citric acid, leave the etchant to stand for at least 10 minutes before etching to achieve a consistent etch rate
  - i. Mix 13.75 g anhydrous citric acid and 13.75 ml DI water (50 % citric acid solution by mass)
  - ii. Heat on a hotplate at  $\approx 130^{\circ}\text{C}$ , stirring occasionally
  - iii. Measure 110 ml DI water
  - iv. Mix 2.5 ml 33.3 % hydrogen peroxide with DI water
  - v. Add 1.5 ml 85 % ortho-phosphoric acid to water-peroxide mix
  - vi. Add the citric acid solution
- (b) Spin S1813 onto sample at 4 krpm for 40s
- (c) Soft-bake at  $115^{\circ}\text{C}$  for 3 minutes
- (d) Align and expose on mask aligner
- (e) Develop in MF319 developer for 60 s, DI water rinse
- (f) Post-development hard bake at  $130^{\circ}\text{C}$  for 2 minutes
- (g) Etch sample until 100 – 120 nm etch depth is achieved
- (h) Terminate etch in DI water

- 
- (i) Wash resist off in Acetone and IPA
2. Ohmic contacts
- (a) Spin S1813 onto sample at 4 krpm for 40s
  - (b) Soft-bake at 115°C for 3 minutes
  - (c) 2 minute soak in chlorobenzene
  - (d) Align and expose on mask aligner
  - (e) Develop in MF319 developer for 60 s, DI water rinse
  - (f) Thermally evaporate Cr/Au ohmic contacts in the ratio 5/95 nm.
  - (g) Lift off in acetone, with gentle agitation with a dropper. DO NOT USE ULTRASONIC AGITATION. This can cause scratches in the mesa, and in the worst case cause your sample to crack.
  - (h) Wash resist residues off in Acetone and IPA
3. Back Gate Deposition (only relevant for a quantum well grown on GaSb)
- (a) Spin S1813 onto sample at 4 krpm for 40s
  - (b) Soft-bake at 115°C for 3 minutes
  - (c) Secure sample on the evaporator holder, upside down, so that the surface with the mesa+contacts is touching a clean glass side
  - (d) Thermally evaporate Cr/Au back gate contact in the ratio 5/95 nm.
  - (e) Wash resist off in Acetone and IPA
4. Top gate process
- (a) Deposit Al<sub>2</sub>O<sub>3</sub> via ALD. Use a water precursor for 300 cycles at 200°C.
  - (b) Spin on PMMA 495 K A 8 at 4 krpm for 40s
  - (c) Soft-bake at 180°C for 2 minutes.
  - (d) Spin S1813 onto sample at 4 krpm for 40s
  - (e) Soft-bake at 115°C for 3 minutes
  - (f) Align and expose on mask aligner
  - (g) Develop in MF319 developer for 60 s, DI water rinse

- 
- (h) Expose PMMA in UVO cleaner for 30 minutes
  - (i) Develop in 7 : 3 IPA: DI water mix for approx 3 minutes, inspect lithography at 2 minutes under dark-field to avoid over-development. Terminate development in IPA
  - (j) Thermally evaporate Cr/Au ohmic contacts in the ratio 5/95 nm.
  - (k) Lift off in acetone, with gentle agitation with a dropper.

#### 5. Scribing and Packaging

- (a) Spin S1813 onto sample at 4 krpm for 40s (to protect the surface)
- (b) Soft-bake at 115°C for 3 minutes
- (c) Using a diamond scribe, make a notch in one side of the sample, break along that line
- (d) Wash resist off in Acetone and IPA
- (e) Glue sample into chip-carrier with silver paint, leave to dry for approx 1 hr.
- (f) Wirebond the sample with silicon doped aluminium wire.

## REFERENCES

- [1] Y. Gul et al. “Quantum ballistic transport in strained epitaxial germanium”. In: *Applied Physics Letters* 111.23 (2017), p. 233512.
- [2] R. L. Samaraweera et al. “Coherent backscattering in quasi-ballistic ultra-high mobility GaAs/AlGaAs 2DES”. In: *Scientific Reports* 8 (2018), p. 10061.
- [3] H. Kroemer. “The 6.1 angstrom family (InAs, GaSb, AlSb) and its heterostructures: a selective review”. In: *Physica E-Low-Dimensional Systems and Nanostructures* 20.3-4 (2004), pp. 196–203.
- [4] S. de Leon, L. D. Shvartsman and B. Laikhtman. “Band structure of coupled InAs/GaSb quantum wells”. In: *Physical Review B* 60.3 (1999), pp. 1861–1870.
- [5] C. X. Liu et al. “Quantum spin Hall effect in inverted Type-II semiconductors”. In: *Physical Review Letters* 100.23 (2008), p. 236601.
- [6] C. L. Kane and E. J. Mele. “Z(2) topological order and the quantum spin Hall effect”. In: *Physical Review Letters* 95.14 (2005), p. 146802.
- [7] Xiao X. et al. “All-electric spin modulator based on a two-dimensional topological insulator”. In: *Applied Physics Letters* 108.2 (2016).
- [8] J. Nilsson, A. R. Akhmerov and C. W. J. Beenakker. “Splitting of a Cooper pair by a pair of Majorana bound states”. In: *Physical Review Letters* 101.12 (2008).
- [9] B. M. Nguyen et al. “High mobility back-gated InAs/GaSb double quantum well grown on GaSb substrate”. In: *Applied Physics Letters* 106.3 (2015), p. 032107.
- [10] L. J. Du et al. “Evidence for a topological excitonic insulator in InAs/GaSb bilayers”. In: *Nature Communications* 8 (2017), p. 1971.

- 
- [11] B. Shojaei et al. “Materials considerations for forming the topological insulator phase in InAs/GaSb heterostructures”. In: *Physical Review Materials* 2.6 (2018), p. 064603.
- [12] I. Knez, R. R. Du and G. Sullivan. “Finite conductivity in mesoscopic Hall bars of inverted InAs/GaSb quantum wells”. In: *Physical Review B* 81.20 (2010), p. 201301.
- [13] L. J. Du et al. “Robust Helical Edge Transport in Gated InAs/GaSb Bilayers”. In: *Physical Review Letters* 114.9 (2015), p. 096802.
- [14] L. J. Du et al. “Tuning Edge States in Strained-Layer InAs/GaInSb Quantum Spin Hall Insulators”. In: *Physical Review Letters* 119.5 (2017), p. 056803.
- [15] S. Mueller et al. “Nonlocal transport via edge states in InAs/GaSb coupled quantum wells”. In: *Physical Review B* 92.8 (2015), p. 081303.
- [16] F. M. Qu et al. “Electric and Magnetic Tuning Between the Trivial and Topological Phases in InAs/GaSb Double Quantum Wells”. In: *Physical Review Letters* 115.3 (2015), p. 036803.
- [17] V. S. Pribiag et al. “Edge-mode superconductivity in a two-dimensional topological insulator”. In: *Nature Nanotechnology* 10.7 (2015), pp. 593–597.
- [18] K. Suzuki et al. “Landau-level hybridization and the quantum Hall effect in InAs/(AlSb)/GaSb electron-hole systems”. In: *Physical Review Letters* 93.1 (2004), p. 016803.
- [19] L. Ortiz et al. “Generic helical edge states due to Rashba spin-orbit coupling in a topological insulator”. In: *Physical Review B* 93.20 (2016), p. 205431.
- [20] A. Rod, T. L. Schmidt and S. Rachel. “Spin texture of generic helical edge states”. In: *Physical Review B* 91.24 (2015), p. 245112.
- [21] I. Vurgaftman, J. R. Meyer and L. R. Ram-Mohan. “Band parameters for III-V compound semiconductors and their alloys”. In: *Journal of Applied Physics* 89.11 (2001), pp. 5815–5875.
- [22] G. Tuttle, H. Kroemer and J. H. English. “Effects of Interface Layer Sequencing on the Transport-Properties of InAs/AlSb Quantum-Wells - Evidence for Antisite Donors at the InAs/AlSb Interface”. In: *Journal of Applied Physics* 67.6 (1990), pp. 3032–3037.

- 
- [23] A. Zakharova, S. T. Yen and K. A. Chao. “Strain-induced semimetal-semiconductor transition in InAs/GaSb broken-gap quantum wells”. In: *Physical Review B* 66.8 (2002), p. 085312.
- [24] M. Altarelli. “Electronic-Structure and Semiconductor-Semimetal Transition in InAs-GaSb Super-Lattices”. In: *Physical Review B* 28.2 (1983), pp. 842–845.
- [25] A. Zakharova, S. T. Yen and K. A. Chao. “Hybridization of electron, light-hole, and heavy-hole states in InAs/GaSb quantum wells”. In: *Physical Review B* 64.23 (2001), p. 235332.
- [26] E. Halvorsen, Y. Galperin and K. A. Chao. “Optical transitions in broken gap heterostructures”. In: *Physical Review B* 61.24 (2000), pp. 16743–16749.
- [27] S. D. Ganichev et al. “Experimental separation of Rashba and Dresselhaus spin splittings in semiconductor quantum wells”. In: *Physical Review Letters* 92.25 (2004), p. 256601.
- [28] W. Xu et al. “Band hybridization and spin-splitting in InAs/AlSb/GaSb type II and broken-gap quantum wells”. In: *Journal of Applied Physics* 108.5 (2010), p. 053709.
- [29] G. Bastard. “Theoretical Investigations of Super-Lattice Band-Structure in the Envelope-Function Approximation”. In: *Physical Review B* 25.12 (1982), pp. 7584–7597.
- [30] I. Lapushkin et al. “A self-consistent investigation of the semimetal-semiconductor transition in InAs/GaSb quantum wells under external electric fields”. In: *Journal of Physics-Condensed Matter* 16.26 (2004), pp. 4677–4684.
- [31] V. V. R. Kishore, B. Partoens and F. M. Peeters. “Electronic structure of InAs/GaSb core-shell nanowires”. In: *Physical Review B* 86.16 (2012).
- [32] F. Nichele et al. “Insulating State and Giant Nonlocal Response in an InAs/GaSb Quantum Well in the Quantum Hall Regime”. In: *Physical Review Letters* 112.3 (2014), p. 036802.
- [33] L. J. Cooper et al. “Resistance resonance induced by electron-hole hybridization in a strongly coupled InAs/GaSb/AlSb heterostructure”. In: *Physical Review B* 57.19 (1998), pp. 11915–11918.

- 
- [34] I. S. Millard et al. “Compressibility studies of double electron and double hole gas systems”. In: *Applied Physics Letters* 68.23 (1996), pp. 3323–3325.
- [35] M. Karalic et al. “Experimental signatures of the inverted phase in InAs/GaSb coupled quantum wells”. In: *Physical Review B* 94.24 (2016), p. 241402.
- [36] I. Knez, R. R. Du and G. Sullivan. “Andreev Reflection of Helical Edge Modes in InAs/GaSb Quantum Spin Hall Insulator”. In: *Physical Review Letters* 109.18 (2012), p. 186603.
- [37] M. A. Reed, W. P. Kirk and P. S. Kobiela. “Investigation of Parallel Conduction in GaAs/Al<sub>X</sub>Ga<sub>1-X</sub>As Modulation-Doped Structures in the Quantum Limit”. In: *IEEE Journal of Quantum Electronics* 22.9 (1986), pp. 1753–1759.
- [38] A. J. A. Beukman et al. “Spin-orbit interaction in a dual gated InAs/GaSb quantum well”. In: *Physical Review B* 96.24 (2017), p. 241401.
- [39] C. Charpentier et al. “Suppression of bulk conductivity in InAs/GaSb broken gap composite quantum wells”. In: *Applied Physics Letters* 103.11 (2013), p. 112102.
- [40] H. L. Stormer, A. C. Gossard and W. Wiegmann. “Observation of Intersubband Scattering in a Two-Dimensional Electron-System”. In: *Solid State Communications* 41.10 (1982), pp. 707–709.
- [41] X. G. Wu. “Influence of an in-plane magnetic field on the electronic structure of an inverted InAs/GaSb quantum well”. In: *Journal of Applied Physics* 122.22 (2017), p. 225704.
- [42] A. O. Caldeira and A. J. Leggett. “Influence of Dissipation on Quantum Tunneling in Macroscopic Systems”. In: *Physical Review Letters* 46.4 (1981), pp. 211–214.
- [43] Y. Naveh and B. Laikhtman. “Magnetotransport of coupled electron-holes”. In: *Europhysics Letters* 55.4 (2001), pp. 545–551.
- [44] J. Li, W. Yang and K. Chang. “Spin states in InAs/AlSb/GaSb semiconductor quantum wells”. In: *Physical Review B* 80.3 (2009), pp. 035303–1–11.
- [45] R. E. Prange. “Quantized Hall Resistance and the Measurement of the Fine-Structure Constant”. In: *Physical Review B* 23.9 (1981), pp. 4802–4805.

- 
- [46] A. Isihara and L. Smrcka. “Density and Magnetic-Field Dependences of the Conductivity of Two-Dimensional Electron-Systems”. In: *Journal of Physics C-Solid State Physics* 19.34 (1986), pp. 6777–6789.
- [47] R. B. Dingle. “Some Magnetic Properties of Metals .2. The Influence of Collisions on the Magnetic Behaviour of Large Systems”. In: *Proceedings of the Royal Society of London Series a-Mathematical and Physical Sciences* 211.1107 (1952), pp. 517–525.
- [48] F. F. Fang, T. P. Smith and S. L. Wright. “Landau-Level Broadening and Scattering Time in Modulation Doped GaAs/AlGaAs Heterostructures”. In: *Surface Science* 196.1-3 (1988), pp. 310–315.
- [49] Charles Kittel. *Introduction to solid state physics*. 7th. New York ; Chichester: Wiley, 1976, pp. 154–176.
- [50] D. Grundler. “Large Rashba splitting in InAs quantum wells due to electron wave function penetration into the barrier layers”. In: *Physical Review Letters* 84.26 (2000), pp. 6074–6077.
- [51] G. Engels et al. “Experimental and theoretical approach to spin splitting in modulation-doped  $\text{In}_x\text{Ga}_{1-x}\text{As}/\text{InP}$  quantum wells for  $B$  approaching 0”. In: *Physical Review B* 55.4 (1997), R1958–R1961.
- [52] Y. H. Park et al. “Separation of Rashba and Dresselhaus spin-orbit interactions using crystal direction dependent transport measurements”. In: *Applied Physics Letters* 103.25 (2013), p. 252407.
- [53] P. J. van Hall, T. Klaver and J. H. Wolter. “Remote Impurity Scattering in Heterojunctions”. In: *Semiconductor Science and Technology* 3.2 (1988), pp. 120–123.
- [54] F. Stern. “Properties of Semiconductor Surface Inversion-Layers in the Electric Quantum Limit”. In: *Current Contents/Physical Chemical and Earth Sciences* 14 (1983), pp. 22–22.
- [55] S. Das Sarma and F. Stern. “Single-Particle Relaxation-Time Versus Scattering Time in an Impure Electron-Gas”. In: *Physical Review B* 32.12 (1985), pp. 8442–8444.

- 
- [56] B. Jeckelmann and B. Jeanneret. “The quantum Hall effect as an electrical resistance standard”. In: *Reports on Progress in Physics* 64.12 (2001), pp. 1603–1655.
- [57] R. B. Laughlin. “Quantized Hall Conductivity in 2 Dimensions”. In: *Physical Review B* 23.10 (1981), pp. 5632–5633.
- [58] R. B. Laughlin. “Nobel Lecture: Fractional quantization”. In: *Reviews of Modern Physics* 71.4 (1999), pp. 863–874.
- [59] R. Nakai, S. Ryu and K. Nomura. “Laughlin’s argument for the quantized thermal Hall effect”. In: *Physical Review B* 95.16 (2017), p. 165405.
- [60] S. W. Hwang et al. “Scaling in Spin-Degenerate Landau-Levels in the Integer Quantum Hall-Effect”. In: *Physical Review B* 48.15 (1993), pp. 11416–11419.
- [61] K. Suzuki, S. Miyashita and Y. Hirayama. “Transport properties in asymmetric InAs/AlSb/GaSb electron-hole hybridized systems”. In: *Physical Review B* 67.19 (2003), p. 195319.
- [62] Chihiro Hamaguchi. *Basic semiconductor physics*. Second edition. Berlin, Heidelberg: Springer, pp 287–293.
- [63] T. P. Marlow et al. “Ground state of a two-dimensional coupled electron-hole gas in InAs/GaSb narrow gap heterostructures”. In: *Physical Review Letters* 82.11 (1999), pp. 2362–2365.
- [64] C. Petchsingh et al. “Effects of electron-hole hybridization on cyclotron resonance in InAs/GaSb heterostructures”. In: *Physical Review B* 70.15 (2004), p. 155306.
- [65] C. Petchsingh et al. “Temperature-dependent cyclotron resonance in a hybridized electron-hole system in InAs/GaSb heterostructures”. In: *Semiconductor Science and Technology* 22.3 (2007), pp. 194–202.
- [66] Y. Vasilyev et al. “Evidence for electron-hole hybridization in cyclotron-resonance spectra of InAs/GaSb heterostructures”. In: *Physical Review B* 60.15 (1999), pp. 10636–10639.
- [67] T. W. Moore. “Cyclotron Resonance Linewidths and Electron Relaxation Times in Gallium”. In: *Physical Review Letters* 16.13 (1966), pp. 581–583.

- 
- [68] P. H. E. Meijer. “A Group Theoretical Proof of Kramers Theorem”. In: *Physica* 26.1 (1960), pp. 61–65.
- [69] B. A. Bernevig, T. L. Hughes and S. C. Zhang. “Quantum spin Hall effect and topological phase transition in HgTe quantum wells”. In: *Science* 314.5806 (2006), pp. 1757–1761.
- [70] C. L. Kane and E. J. Mele. “Quantum spin Hall effect in graphene”. In: *Physical Review Letters* 95.22 (2005), p. 226801.
- [71] M. König et al. “The quantum spin Hall effect: Theory and experiment”. In: *Journal of the Physical Society of Japan* 77.3 (2008), p. 031007.
- [72] B. A. Bernevig and S. C. Zhang. “Quantum spin Hall effect”. In: *Physical Review Letters* 96.10 (2006), p. 106802.
- [73] A. Fert and H. Jaffres. “Conditions for efficient spin injection from a ferromagnetic metal into a semiconductor”. In: *Physical Review B* 64.18 (2001), p. 184420.
- [74] E. M. Spanton et al. “Images of Edge Current in InAs/GaSb Quantum Wells”. In: *Physical Review Letters* 113.2 (2014), p. 026804.
- [75] J. Maciejko, X. L. Qi and S. C. Zhang. “Magnetoelectricity of the quantum spin Hall state”. In: *Physical Review B* 82.15 (2010).
- [76] M. König et al. “Quantum spin hall insulator state in HgTe quantum wells”. In: *Science* 318.5851 (2007), pp. 766–770.
- [77] N. F. Mott. “The Transition to the Metallic State”. In: *Philosophical Magazine* 6.62 (1961), pp. 287–309.
- [78] D. Jerome, T. M. Rice and W. Kohn. “Excitonic Insulator”. In: *Physical Review* 158.2 (1967), pp. 462–475.
- [79] C. Brune et al. “Spin polarization of the quantum spin Hall edge states”. In: *Nature Physics* 8.6 (2012), pp. 485–490.
- [80] Marian A. H. and Helmut S. *Molecular beam epitaxy : fundamentals and current status*. Springer series in materials science. Berlin ; London: Springer, 1989, pp. 1–20.
- [81] D. J. Eaglesham and M. Cerullo. “Low-Temperature Growth of Ge on Si(100)”. In: *Applied Physics Letters* 58.20 (1991), pp. 2276–2278.

- 
- [82] J. Thornton et al. *Scanning Probe Microscopy Training Notebook*. 1997, p. 64.
- [83] A. San Paulo and R. Garcia. “Unifying theory of tapping-mode atomic-force microscopy”. In: *Physical Review B* 66.4 (2002), p. 041406.
- [84] P. Jalonen and A. Tuominen. “The effect of core material surface roughness on line accuracy using electrodeposited photoresist”. In: *Proceedings of International Symposium on Electronic Materials and Packaging* (2000), pp. 156–159.
- [85] B. Z. Nosho et al. “Surface morphology of homoepitaxial GaSb films grown on flat and vicinal substrates”. In: *Journal of Crystal Growth* 236.1-3 (2002), pp. 155–164.
- [86] M. Hatzakis, B. J. Canavello and J. M. Shaw. “Single-Step Optical Lift-Off Process”. In: *IBM Journal of Research and Development* 24.4 (1980), pp. 452–460.
- [87] C. C. Negrila et al. “XPS Analysis of AuGeNi/Cleaved GaAs(110) Interface”. In: *Journal of Nanomaterials* (2016), p. 7574526.
- [88] E. Rudy. “Constitution of Ternary Titanium-Tungsten-Carbon Alloys”. In: *Journal of the Less-Common Metals* 33.2 (1973), pp. 245–273.
- [89] A. N. Pal et al. “Influence of etching processes on electronic transport in mesoscopic InAs/GaSb quantum well devices”. In: *AIP Advances* 5.7 (2015), p. 077106.
- [90] O. Dier et al. “Selective and non-selective wet-chemical etchants for GaSb-based materials”. In: *Semiconductor Science and Technology* 19.11 (2004), pp. 1250–1253.
- [91] M. N. Kutty et al. “Study of Surface Treatments on InAs/GaSb Superlattice LWIR Detectors”. In: *Journal of Electronic Materials* 39.10 (2010), pp. 2203–2209.
- [92] I. Knez et al. “Observation of Edge Transport in the Disordered Regime of Topologically Insulating InAs/GaSb Quantum Wells”. In: *Physical Review Letters* 112.2 (2014), p. 026804.
- [93] Marija Drndic. “Transport Properties of InAs/Ga(Al)Sb Single Electron and Double Electron-Hole QWs”. MPhil. University of Cambridge, 1995.

- 
- [94] C. Mittag et al. “Passivation of edge states in etched InAs sidewalls”. In: *Applied Physics Letters* 111.8 (2017), p. 082101.
- [95] R. W. Johnson, A. Hultqvist and S. F. Bent. “A brief review of atomic layer deposition: from fundamentals to applications”. In: *Materials Today* 17.5 (2014), pp. 236–246.
- [96] X. Tang et al. “Room temperature atomic layer deposition of  $\text{Al}_2\text{O}_3$  and replication of butterfly wings for photovoltaic application”. In: *Journal of Vacuum Science and Technology A* 30.1 (2012).
- [97] C. L. Lin et al. “Variety transformation of compound at GaSb surface under sulfur passivation”. In: *Japanese Journal of Applied Physics Part 2-Letters* 37.12B (1998), pp. L1543–L1545.
- [98] Joseph Thomas Batley. “Spin transport in lateral spin valves”. Thesis (Ph D ). University of Leeds (School of Physics and Astronomy), 2015.
- [99] J. W. Ekin. *Experimental techniques for low-temperature measurements*. New York: Oxford University Press, pp. 6–704.
- [100] Anthony Kent. *Experimental low temperature physics*. Macmillan Physical Sciences Series. Basingstoke: Macmillan, 1993, pp. 1–216.
- [101] M. S. Lubell. “Empirical Scaling Formulas for Critical Current and Critical-Field for Commercial NbTi”. In: *IEEE Transactions on Magnetism* 19.3 (1983), pp. 754–757.
- [102] H. R. Segal et al. “The Use of NbTiTa as a High-Field Superconducting Alloy”. In: *IEEE Transactions on Magnetism* 17.1 (1981), pp. 53–56.
- [103] C. S. Knox et al. “Partial hybridisation of electron-hole states in an InAs/GaSb double quantum well heterostructure”. In: *Semiconductor Science and Technology* 32.10 (2017), p. 104002.
- [104] P. J. van Hall. “Remote Impurity Scattering in GaAs-AlGaAs Heterojunctions”. In: *Superlattices and Microstructures* 6.2 (1989), pp. 213–216.
- [105] Y. F. Komnik et al. “Quantum effects in hole-type Si/SiGe heterojunctions”. In: *Low Temperature Physics* 26.8 (2000), pp. 609–614.

- 
- [106] C. Petchsingh et al. “Mass enhancement and electron-hole coupling in InAs/GaSb bilayers studied by cyclotron resonance”. In: *Physica E-Low-Dimensional Systems and Nanostructures* 12.1-4 (2002), pp. 289–292.
- [107] J. Luo et al. “Effects of Inversion Asymmetry on Electron-Energy Band Structures in Gasb Inas Gasb Quantum-Wells”. In: *Physical Review B* 41.11 (1990), pp. 7685–7693.
- [108] K. Nilsson et al. “Cyclotron masses and g-factors of hybridized electron-hole states in InAs/GaSb quantum wells”. In: *Physical Review B* 74.7 (2006), p. 075308.
- [109] X. H. Zhang et al. “Nonlinear Hall Effect as a Signature of Electronic Phase Separation in the Semimetallic Ferromagnet EuB6”. In: *Physical Review Letters* 103.10 (2009), p. 106602.
- [110] I. Knez, R. R. Du and G. Sullivan. “Evidence for Helical Edge Modes in Inverted InAs/GaSb Quantum Wells”. In: *Physical Review Letters* 107.13 (2011), p. 136603.
- [111] M. J. Yang et al. “Evidence of a hybridization gap in “semimetallic” InAs/GaSb systems”. In: *Physical Review Letters* 78.24 (1997), pp. 4613–4616.
- [112] H. Bluyssen et al. “Cyclotron-Resonance in an InAs-GaSb Super-Lattice”. In: *Solid State Communications* 31.1 (1979), pp. 35–38.
- [113] H. J. A. Bluyssen et al. “Cyclotron-Resonance and Shubnikov-de Haas Experiments in a N-InAs-GaSb Super-Lattice”. In: *Physical Review B* 25.8 (1982), pp. 5364–5372.
- [114] D. I. Pikulin et al. “Disorder and magnetic-field-induced breakdown of helical edge conduction in an inverted electron-hole bilayer”. In: *Physical Review B* 89.19 (2014), p. 161403.
- [115] P. C. Klipstein. “Structure of the quantum spin Hall states in HgTe/CdTe and InAs/GaSb/AlSb quantum wells”. In: *Physical Review B* 91.3 (2015), p. 035310.
- [116] S. Das Sarma and E. H. Hwang. “Universal density scaling of disorder-limited low-temperature conductivity in high-mobility two-dimensional systems”. In: *Physical Review B* 88.3 (2013), p. 035439.

- 
- [117] G. Q. Hai et al. “Intersubband-coupling and screening effects on the electron transport in a quasi-two-dimensional  $\delta$ -doped semiconductor system”. In: *Journal of Applied Physics* 80.10 (1996), pp. 5809–5814.
- [118] A. Kurobe et al. “Wave-Functions and Fermi Surfaces of Strongly Coupled 2-Dimensional Electron Gases Investigated by In-plane Magnetoresistance”. In: *Physical Review B* 50.7 (1994), pp. 4889–4892.
- [119] O. N. Makarovskii et al. “Magnetoresistance and electronic structure of asymmetric GaAs/Al<sub>0.3</sub>Ga<sub>0.7</sub>As double quantum wells in an in-plane or tilted magnetic field”. In: *Physical Review B* 62.16 (2000), pp. 10908–10913.
- [120] T. Tschirky et al. “Scattering mechanisms of highest-mobility InAs/Al<sub>x</sub>Ga<sub>(1-x)</sub>Sb quantum wells”. In: *Physical Review B* 95.11 (2017), p. 115304.
- [121] J. A. Vanvechten. “Quantum Dielectric Theory of Electronegativity in Covalent Systems .I. Electronic Dielectric Constant”. In: *Physical Review* 182.3 (1969), pp. 891–903.
- [122] B. K. Ridley. “The Electron Phonon Interaction in Quasi-2-Dimensional Semiconductor Quantum-Well Structures”. In: *Journal of Physics C-Solid State Physics* 15.28 (1982), pp. 5899–5917.
- [123] J. M. S. Orr et al. “Electronic transport in modulation-doped InSb quantum well heterostructures”. In: *Physical Review B* 77.16 (2008), p. 165334.
- [124] H. J. G. Meijer and D. Polder. “Note on Polar Scattering of Conduction Electrons in Regular Crystals”. In: *Physica* 19.2 (1953), pp. 255–264.
- [125] M. A. Alzamil. “Electron Mobility Calculations of N-InAs”. In: *Digest Journal of Nanomaterials and Biostructures* 6.2 (2011), pp. 725–729.
- [126] I. Lo et al. “Negative Persistent Photoconductivity in the Al<sub>0.6</sub>Ga<sub>0.4</sub>Sb/InAs Quantum-Wells”. In: *Applied Physics Letters* 60.6 (1992), pp. 751–753.
- [127] S. Luryi. “Quantum Capacitance Devices”. In: *Applied Physics Letters* 52.6 (1988), pp. 501–503.
- [128] E. D. Siggia and P. C. Kwok. “Properties of Electrons in Semiconductor Inversion Layers with Many Occupied Electric Subbands .1. Screening and Impurity Scattering”. In: *Physical Review B* 2.4 (1970), pp. 1024–1036.

- 
- [129] J. M. Heisz and E. Zaremba. “Transverse magnetoresistance of GaAs/Al<sub>x</sub>Ga<sub>1-x</sub>As heterojunctions in the presence of parallel magnetic fields”. In: *Physical Review B* 53.20 (1996), pp. 13594–13604.
- [130] T. Englert et al. “A Study of Intersubband Scattering in GaAs-Al<sub>x</sub>Ga<sub>1-x</sub>As Heterostructures by Means of a Parallel Magnetic-Field”. In: *Solid State Communications* 45.11 (1983), pp. 989–991.
- [131] M. Lakrimi et al. “Minigaps and novel giant negative magnetoresistance in InAs/GaSb semimetallic superlattices”. In: *Physical Review Letters* 79.16 (1997), pp. 3034–3037.
- [132] A. V. Goran et al. “Anisotropic positive magnetoresistance of a nonplanar 2D electron gas in a parallel magnetic field”. In: *JETP Letters* 79.10 (2004), pp. 495–498.
- [133] A. V. Goran, A. A. Bykov and A. I. Toropov. “Classical anisotropic magnetoresistance of a non-planar 2D electron gas in a parallel magnetic field”. In: *Semiconductor Science and Technology* 23.10 (2008), p. 105017.
- [134] Q. Shi et al. “Strong transport anisotropy in Ge/SiGe quantum wells in tilted magnetic fields”. In: *Physical Review B* 91.20 (2015), p. 201301.
- [135] W. Pan et al. “Chaotic quantum transport near the charge neutrality point in inverted type-II InAs/GaSb field-effect transistors”. In: *Applied Physics Letters* 102.3 (2013), p. 033504.
- [136] C. S. Knox et al. “Deconvolution of Rashba and Dresselhaus spin-orbit coupling by crystal axis dependent measurements of coupled InAs/GaSb quantum wells”. In: *Physical Review B* 98.15 (2018), p. 155323.
- [137] H. H. Luo et al. “Spin dynamics of electrons in the first excited subband of a high-mobility low-density two-dimensional electron system”. In: *Physical Review B* 80.19 (2009), p. 193301.
- [138] J. Nitta et al. “Gate control of spin-orbit interaction in an inverted In<sub>(0.53)</sub>Ga<sub>(0.47)</sub>As/In<sub>(0.52)</sub>Al<sub>(0.48)</sub>As heterostructure”. In: *Physical Review Letters* 78.7 (1997), pp. 1335–1338.
- [139] G. Gumbs. “Rashba effect on the plasma oscillations in a coupled bilayer of electrons and holes”. In: *Applied Physics Letters* 85.14 (2004), pp. 2821–2823.

- 
- [140] A. H. A. Hassan et al. “An origin behind Rashba spin splitting within inverted doped sGe heterostructures”. In: *Applied Physics Letters* 110.4 (2017), p. 042405.
- [141] G. L. Bir, A. G. Aronov and G. E. Pikus. “Spin Relaxation of Electrons Scattered by Holes”. In: *Zhurnal Eksperimentalnoi I Teoreticheskoi Fiziki* 69.4 (1975), pp. 1382–1397.
- [142] J. S. Sandhu et al. “Gateable suppression of spin relaxation in semiconductors”. In: *Physical Review Letters* 86.10 (2001), pp. 2150–2153.
- [143] N. S. Averkiev and L. E. Golub. “Giant spin relaxation anisotropy in zinc-blende heterostructures”. In: *Physical Review B* 60.23 (1999), pp. 15582–15584.
- [144] J. Schliemann, J. C. Egues and D. Loss. “Nonballistic spin-field-effect transistor”. In: *Physical Review Letters* 90.14 (2003), p. 146801.
- [145] J. L. Yu et al. “Tuning of Rashba/Dresselhaus Spin Splittings by Inserting Ultra-Thin InAs Layers at Interfaces in Insulating GaAs/AlGaAs Quantum Wells”. In: *Nanoscale Research Letters* 11 (2016), p. 477.
- [146] P. Roussignol et al. “Time-Resolved Spin-Polarization Spectroscopy in GaAs/AlGaAs Quantum-Wells”. In: *Surface Science* 267.1-3 (1992), pp. 360–364.
- [147] R. J. Elliott. “Theory of the Effect of Spin-Orbit Coupling on Magnetic Resonance in Some Semiconductors”. In: *Physical Review* 96.2 (1954), pp. 266–279.
- [148] A. Kiss, L. Szolnoki and F. Simon. “The Elliott-Yafet theory of spin relaxation generalized for large spin-orbit coupling”. In: *Scientific Reports* 6 (2016), p. 22706.
- [149] F. Nichele et al. “Edge transport in the trivial phase of InAs/GaSb”. In: *New Journal of Physics* 18 (2016), p. 083005.
- [150] L. D. Shvartsman and B. Laikhtman. “InAs-GaSb laser: Prospects for efficient terahertz emission”. In: *Applied Physics Letters* 93.13 (2008), p. 131104.